POLARIZATION PHENOMENA IN ORGANIC NANOSTRUCTURES

by

Donna Kunkel

A DISSERTATION

Presented to the Faculty of

The Graduate College at the University of Nebraska

In Partial Fulfilment of Requirements

For the Degree of Doctor of Philosophy

Major: Physics and Astronomy

Under the Supervision of Professor Axel Enders

Lincoln, Nebraska

August, 2014

POLARIZATION PHENOMENA IN ORGANIC NANOSTRUCTURES

Donna Kunkel, Ph.D.

University of Nebraska, 2014

Adviser: Axel Enders

This thesis explores the self-assembly and surface interactions of two classes of organic molecules through scanning tunneling microscopy. The primary scientific goal of this thesis is to better understand the electric polarization in surface-supported organic molecules, whether inherent to a molecule or acquired through intermolecular interactions.

First, a class of dipolar molecules, the quinonoid zwitterions, are examined on three noble metal surfaces. Two-dimensional islands of hydrogen-bonded molecules, with aligned dipole moments, are formed on Au(111). However, other structures with zero net dipole moment are observed on Ag(111) and Cu(111). Modifying the molecules with longer substituent tails results in the formation of one-dimensional chains irrespective of the surface. Our calculations show that the dipole moment is not the driving factor determining the self-assembly of these molecules. Instead a more complicated picture emerges in which extensive charge transfer with the surface drastically reduces the dipole moment of the molecule by nearly 9 D, so that dipolar energies become small compared to typical chemical bond energies such as hydrogen bonds.

Second, the self-assembly of three molecules, croconic acid, rhodizonic acid, and 3-hydroxyphenalenone (3-HPLN) are studied on three noble metal surfaces. These molecules were chosen due to their ferroelectric bulk properties, which arise from switchable hydrogen bonds. On Ag, croconic acid forms two-dimensional hydrogen

bonded sheets which are, in theory, capable of proton transfer. While these compounds form hydrogen bonded structures on Ag(111) and Au(111), on the more reactive Cu(111) surface metal-organic frameworks involving surface metal atoms are observed for rhodizonic acid, highlighting the importance of surface chemistry. Additionally, on an insulating buffer layer, CuN, croconic acid forms a densely packed hydrogen bonded structure, which more closely resembles its bulk phase, demonstrating the effect of charge transfer on self-assembly.

Additionally, hydrogen bonded co-crystals of 3-HPLN and croconic acid are synthesized on Au(111). Co-crystals of quinonoid zwitterions and croconic acid are also reported. Guided by the surface science studies, related 3D organic co-crystals were grown. Finally, the topic 2D magic organic clusters is presented as a new branch of research. Five new organic magic clusters are described. The research presented in this thesis has relevance to a broad range of applications including data storage devices and molecular electronics.

ACKNOWLEDGMENTS

First and foremost, I want to offer sincere and heartfelt thanks to my thesis adviser, Dr. Axel Enders. His passion for science and learning is nothing short of inspiring. Throughout the years, he has always provided me with kind words of encouragement and wise words of guidance. As a scientist, he has served as an exceptional role model. On a personal note, his warm and gregarious personality has made working with him an absolute pleasure.

I would also like to thank my committee members, Dr. Peter Dowben, Dr. Stephen Ducharme, and Dr. Eva Franke-Schubert for their service both as committee members as well as mentors. Furthermore, I would like to thank my numerous collaborators. Chief among them, Dr. Eva Zurek, Scott Simpson, and Dr. James Hooper have continuously proven to be excellent scientists whose tireless research has provided theoretical insights which add significant value to my thesis. Additionally, I want to thank Dr. Alexander Sinitskii and his students Timothy Vo and Wayz Khan for their collaborations. Aside from the committee service, I also would like to thank Dr. Stephen Ducharme and his student Shashi Poddar, and Dr. Peter Dowben for their scientific collaborations.

I wish to acknowledge my former lab mates Geoffrey Rojas and Xumin Chen for training me on the instrumentation. I would also like to thank my fellow researcher Sumit Beniwal for continually helping in every aspect of research. By aiding me in everything from routine maintenance to providing valuable scientific discussions Sumit has made this thesis possible. Additionally, his humor and friendship has made conducting research for this thesis enjoyable. Finally, I wish to sincerely thank my friends and family for providing unconditional support during my graduate years. With that, to everyone mentioned above: Thank you!

PUBLICATIONS RELATED TO THIS RESEARCH

11. S. Beniwal, S. Chen, X.-C. Zeng, S. Simpson, J. Hooper, E. Zurek, **D. A. Kunkel**, A. Enders *Kagome Lattice of π-π Stacked 3-Hydroxyphenalenone on Cu(111)* accepted Chem. Commun. (2014)

10. J. Hooper, **D. A. Kunkel**, S. Simpson, S. Beniwal, A. Enders, E. Zurek *Chiral Surface Networks of 3-HPLN - A Molecular Analog of Rounded Triangle Assembly?* Surface Science, in print (2014)

9. T. H. Vo, M. D. Morton, M. Shekkirev, **D. A. Kunkel**, E. Berglund, P. Wilson, A. Enders, A. Sinitskii *Bottom-up Synthesis of Narrow Nitrogen-doped Graphene Nano-ribbons* Chem. Commun. **50** 4172-4174 (2014).

8. T. H. Vo, M. Shrekhirev, **D. A. Kunkel**, M. D. Morton, E. Berglund, L. Kong, P. M. Wilson, P. A. Dowben, A. Enders, A. Sinitskii *Large-Scale Solution of Narrow Graphene Nanoribbons*, Nat. Commun. **5** 3189 (2014).

7. **D. A. Kunkel**, J. Hooper, S. Simpson, S. Beniwal, K. L. Morrow, D. C. Smith, K. Cousins, S. Ducharme, E. Zurek, A. Enders *Rhodizonic Acid on Noble Metals: Surface Reactivity and Coordination Chemistry*, J. Phys. Chem. Lett. **4**, 3413 (2013).

6. S. Simpson, **D. A. Kunkel**, J. Hooper, J. Nitz, P. A. Dowben, L. Routaboul, P. Braunstein, B. Doudin, A. Enders, E. Zurek, *Coverage-Dependent Interactions at the Organics-Metal Interface: Quinonoid Zwitterions on Au(111)*, J. Phys. Chem. C **117**, 16406 (2013).

5. **D. A. Kunkel**, J. Hooper, S. Simpson, G. A. Rojas, S. Ducharme, T. Usher, E. Zurek, A. Enders *Proton Transfer in Surface-Stabilized Chiral Motifs of Croconic Acid*, Phys. Rev. B **87**, 041402 (2013).

4. P. A. Dowben, **D. A. Kunkel**, A. Enders, Luis G. Rosa, L. Routaboul, B. Doudin, P. Braunstein *The Dipole Mediated Surface Chemistry of p-Benzoquinonemonoimine Zwitterions*, Top. Cat.**56**, 1096 (2013).

3. **D. A. Kunkel**, S. Simpson, J. Nitz, G. A. Rojas, E.Zurek, L. Routaboul, B. Doudin, P. Braunstein, P. A. Dowben, A. Enders *Dipole Driven Schemes of Quinonoid Zwitterions on Surfaces*, Chem. Commun. **48**, 7143 (2012).

2. G. Rojas, S. Simpson, X. Chen, **D. A. Kunkel**, J.Nitz, J. Xiao, P. A. Dowben, E. Zurek, and A. Enders *Surface State Engineering of Molecule-Molecule Interactions*, Phys. Chem. Chem. Phys. **14**, 4971-4976 (2012).

1. G. Rojas, X. Chen, D. Kunkel, M. Bode, A. Enders *Temperature Dependence of Metal-Organic Heteroepitaxy*, Langmuir **27**, 14267-14271 (2011).

Contents

Chapter 1

Introduction

Organic molecules share many properties with semi-conductors and some key differences, and yet could potentially become an attractive substitute in devices because of superior structural and mechanical properties, increased flexibility, lower costs of production, and increased performance in light absorption and emittance [1]. Prototypes of organic based devices have been demonstrated for applications ranging from medical physics equipment [2–4] to data storage devices [5]. Organic based devices have already demonstrated commercial success in the form of components in solar cells, organic light emitting diodes (OLEDs), and carbon nanotube enhanced materials, among many others. Judiciously chosen organic molecules have even been used to increase the lifetime of LEDs by more than one order of magnitude [6].

Similar to semi-conductors, the electronic band structure of organics, such as frontier orbital energy levels and their separation, must be precisely controlled for any electronic application. Organic molecules have tunable electronic [7] and optical [8] properties, whereby small modifications in chemical formulation can result in significant changes to these properties. For example modifying substituents results in different internal rotation angles for a class of polymers, which strongly influences the

wavelengths of adsorption and luminescence [8].

Utilizing organics in devices often requires depositing them onto a supporting substrate or attaching metal electrodes. Metal-organic interactions at the junction can drastically change fundamental properties of the organic layers [9]. Some observed effects are the modification of the workfunction [1, 10], alterations of carrier density [11] and leakage currents in field-effect transitiors [2], the emergence of new electronic states due to the hybridization of organic and metal orbitals [12], and even the emergence of magnetism [13]. For applications such as OLEDs matching the electrode workfunction with the lowest unoccupied molecular orbital (LUMO) or highest occupied molecular orbital (HOMO) of the organic adlayer is of fundamental importance for electron or hole injection, and thus device performance [14, 15]. Optimizing organic photovoltaic devices means balancing interrelated properties including exiton diffusion lengths, optical absorbtion lengths, and carrier mobilities in which the morphology of the organic donor/acceptor layers is critical [16]. The electronic and optical properties also vary dramatically with the local structural order, interface effects, deposition method, and impurity concentration [17]. While much effort has been spent on quantifying the properties of organics, relatively much less effort has been directed towards elucidating interface effects, even though these are of fundamental importance to bulk-heterojunction solar cells, transistors, and light-emitting devices [17].

Functional properties such as switchable electric or magnetic polarizations are sometimes inherent to a single molecule or amorphous layer and do not depend on the crystalline structure of the organic layer. For example spin crossover molecules exhibit a low spin to high spin transition for individual molecules [18]. In the case of organic ferroelectrics, such as polyvinylidene difluoride (PVDF), a perfect crystalline structure is not always necessary to display ferroelectricity, in stark contrast to in-

organic ferroelectrics such as barium titanate (BTO) in which the ferroelectricity is derived from changes to the crystalline structure. Tolerance for structural defects and even disorder has the benefit of lowering production costs significantly. This is exemplified by the use of low cost deposition methods for certain applications such as the ink jet printing of organics instead of mask-based lithography or other expensive multistep processing methods required for traditional inorganic materials [19]. Furthermore, traditional inorganics often contain environmentally problematic elements such as lead [20], which further increases the usefulness of chemically benign organic ferroelectrics.

Molecules with an innate electric dipole moment have promise to be utilized in the manipulation of energy level alignment of interfaces, and thus a slew of device properties such as charge injection barriers and the workfunction [21, 22]. Dipolar molecules also have the potential to be used as single molecule data storage devices [23]. Moreover, these organics present an opportunity to study whether simple dipole models can be applied to real systems [24].

For organics to become viable model systems in device materials, pressing questions must first be answered through basic research. These include: How does the dipole moment change upon adsorption to the surface? Can the dipole moment or polarization be manipulated through bond formation? How large of a role do electric dipole moments play in determining self-assembled structures? All of these need to be addressed through basic science as a prerequisite to designing the organic based devices of the future.

This thesis aims to answer these questions through the study of polarization phenomena in single molecules and assemblies of dipolar molecules. It discusses both molecules with an inherent static dipole as well as those acquired from intermolecular bonds. Key findings presented in this thesis are:

- Ascertaining that substrate interactions drastically modify the dipole moment of organic adsorbates.

- The discovery that tailoring chemical substituents of dipolar molecules and substrate interactions can switch growth from structures with zero dipole moment to polarized electrets.

- Establishing that, counter to common assumption in the literature, no evidence is found that dipole moments are driving the self-assembly of dipolar molecules. The energies associated with dipole-dipole interactions are negligble compared with other relevant energies.

- The discovery of surface supported, 2D hydrogen bonded structures that are predicted to exhibit a spontaneous ferroelectric polarization due to collective hydrogen bond switching.

- Determining that resonance assisted hydrogen bonds can exist in metal-supported organic systems.

- The first report of crystalline phases of rhodizonic acid.

- The discovery of 2D hydrogen bonded co-crystals that directly led to the synthesis of novel 3D co-crystals.

- Pioneering the concept of magic organic clusters on surfaces.

Chapter 2

Fundamentals

This chapter provides an experimental and theoretical overview of the specific intermolecular and molecule-surface interactions that are further discussed in this thesis. Additionally, the literature addressing the self-assembly of dipolar molecules is reviewed. Finally, the experimental instrumentation and methods for the work discussed in Chapters 3-6 is given.

2.1   Intermolecular Interactions

The bonding of any organic material, whether two or three dimensional, is determined by the interplay of attractive and repulsive forces. These attractive forces include, for example, hydrogen bonding, covalent bonding, $\pi - \pi$ and CH-π bonding, Coulombic attractions, and van der Waals forces. Note that Coulombic forces and permanent dipoles can interact repulsively as well. The role of electric dipoles is often discussed in the literature, with sometimes controversial conclusions, as will be shown. It is therefore necessary to revisit the concept of dipolar interactions in 2D arrangments of dipoles.

2.1.1   Dipole-Dipole Interactions

An electric dipole moment arises when opposite charges are separated a distance, and is defined by:

$$\vec{p} = q\vec{l} \tag{2.1}$$

where $\vec{p}$ is the dipole moment, q is the charge, and $\vec{l}$ is the distance separating the charges. The direction of $\vec{l}$ points from negative to positive charge. Dipole moments are typically given in units of Debye (D), in which $1D \approx 0.208$ eÅ.

Values of organic dipole moments in natural substances vary quite significantly, ranging from 0 D to over 10 D. Table 2.1 gives values of dipole moments for common organic molecules as well as the organic species discussed later in this thesis.

For a pair of two dipoles, $\vec{p_1}$ and $\vec{p_2}$, the dipole-dipole interaction energy is dependent on the separation distance, $\vec{r}$, and the relative orientations of the dipoles. The dipole-dipole energy is given by:

$$U = \frac{1}{8\pi\epsilon_0}\frac{1}{r^3}[\vec{p_1} \cdot \vec{p_2} - 3(\vec{p_1} \cdot \hat{r})(\vec{p_2} \cdot \hat{r})] \tag{2.2}$$

A simple schematic of the quantities involved in Equation 2.2 is shown in Fig. 2.1. Equation 2.2 is valid when the separation between the dipoles, $\vec{r}$, is more than three times the length of the diople, l [25]. Fig. 2.2 illustrates the reason for this. When the

Table 2.1: Magnitude of dipole moments for common organic species and those studied in this thesis.

Organic Species	Dipole Moment (D)
CO_2	0
H_2O	1.85
3-Hydroxyphenalenone	5.98
NaCl	9
Croconic Acid	9-10
Quinonoid Zwitterion	10

dipole separation is similar to the length of a dipole as in (b), the Coulombic energy of the central two charges is underestimated because their spacing is overestimated. In this case, it is more accurate to evaluate the interaction energy of all point charges.
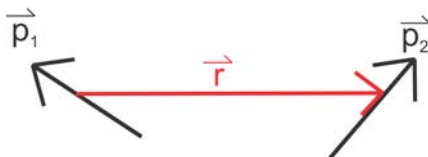
Figure 2.1: Illustration of two point dipoles separated a distance r. The energy of this con guration can is given by Equation 2.2.
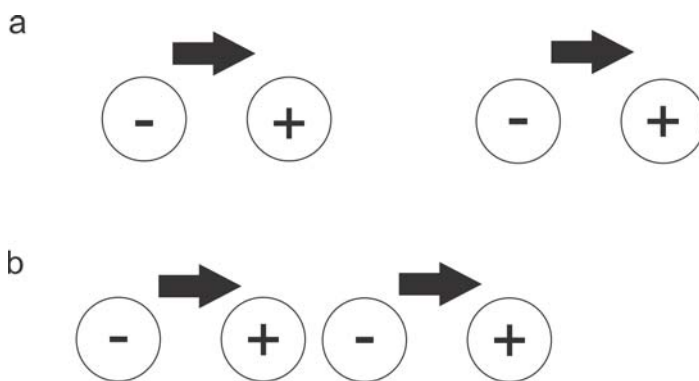
Figure 2.2: (a) When dipoles are far from each other relative to their internal length equation 2.2 holds. However, when dipoles become close as in (b) equation 2.2 underestimates contributions from nearby charges and equation 2.3 must be utilized.

Using Equation 2.2, the relative energies of various dipolar con gurations as a function of the separation between neighboring dipoles can be evaluated. The energies of the dimer con gurations shown in Fig. 2.3 were calculated for a dipole moment of 1 D per dipole. Note that two con gurations are attractive and two are repulsive, and this does not depend on the separation distance. However, the relative favorability of the con gurations switches at r = 0.8 nm.
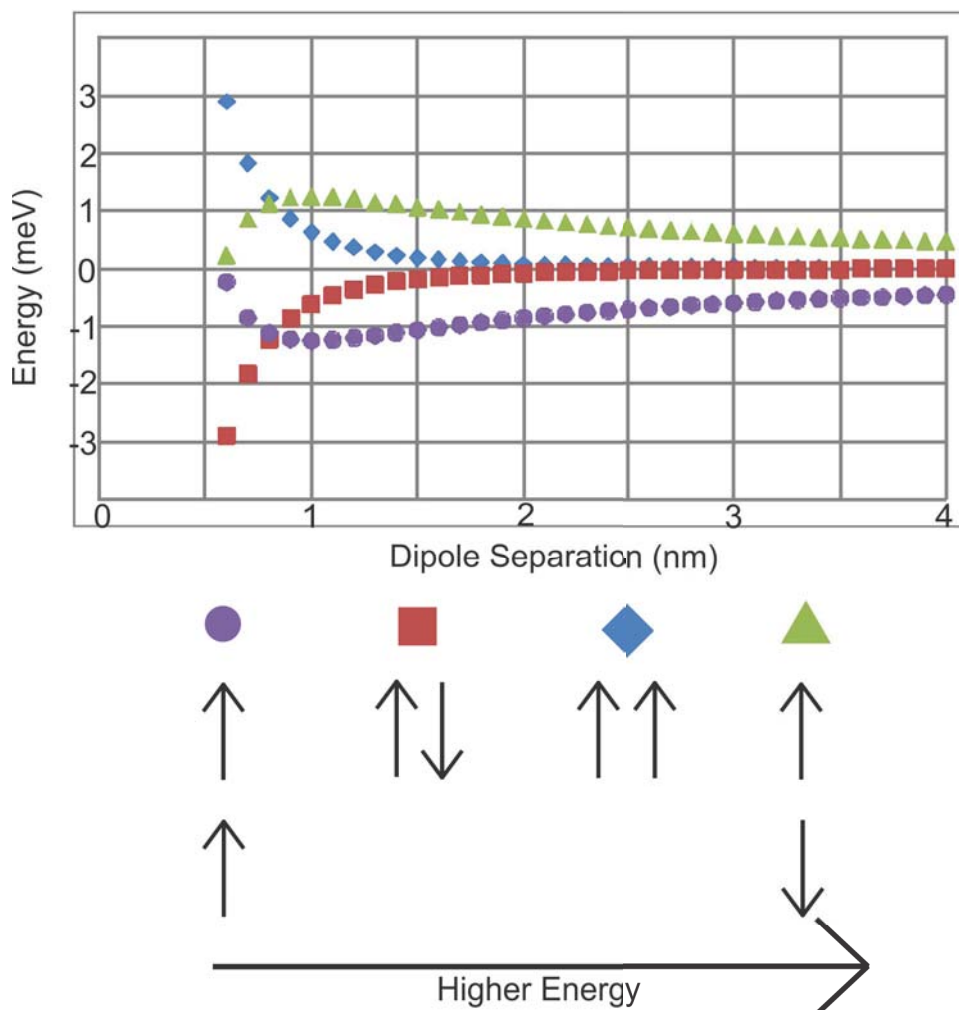
Figure 2.3: The energy in meV is plotted versus separation distance in nm for the dipole dimer con gurations illustrated. The two con gurations to the left are attractive, whereas the other two are repulsive.

Self-assembled molecular systems often have a separation of neighboring dipoles that is much less than three times the charge separation, l. For example, in many of the systems discussed in Chapter 3, the size of the molecule, which roughly corresponds to charge separation, is approximately 5 A and the intermolecular spacing is approximately 7 A. Therefore, the dipole approximation (Equation 2.2) is not a good approximation and point charges have to be evaluated instead. This is achieved by treating the dipoles as a discrete set of Coulombic charges, in which the energy of

each pair of charges is summed. To avoid double counting, there is an extra factor of
1/2 in the equation, which is given by:

$$U = \frac{1}{8\pi\epsilon_0} \sum_{i=1}^{n} \sum_{j=1}^{n} \frac{q_i q_j}{r_{ij}} \tag{2.3}$$

where r_{ij} is the distance connecting the ith and j^{th} charge.

In order to probe the electrostatic energy in 2D assemblies, four model tetramers
illustrated in Fig. 2.4, were evaluated. The energy of each of these configurations was
calculated with the point dipole approximation (Equation 2.2) and with the Coulomb
equation (Equation 2.3). For each of these, the dipole moment was selected to be 1
D, the dipole length 0.5 nm, and the charge of 0.0416 e. The energies were calculated
for three different separation distances: 0.5 nm, 1 nm, and 5 nm. The calculations for
the "Alternating Chain" and "Parallel Chain" configurations remain valid for dipole
moments which point out of the plane. However, we have not considered out of the
plane analogs for the "Square" and "Diamond" configurations, because those require
3D growth to construct.

Figure 2.5 plots the results of the calculations. First, compare the results for
Equation 2.2 and 2.3 for any given configuration. Notice that at a short dipole sepa-
ration (r = 0.6 nm) the point dipole approximation yields very different results than
the Coulomb equation. This effect is particularly noticable for the square configura-
tion. As the dipolar separation is increased to 5 nm, the energetic differences between
Equation 2.2 and 2.3 become negligble, as is expected.

Second, for a given equation one can compare the energies of the configurations to
each other. Note that the parallel chain is the only repulsive configuration for both
equations. For the point dipole approximation, the three attractive configurations are
of very similar energies, within 1 meV at all length scales. For the Coulomb equation,
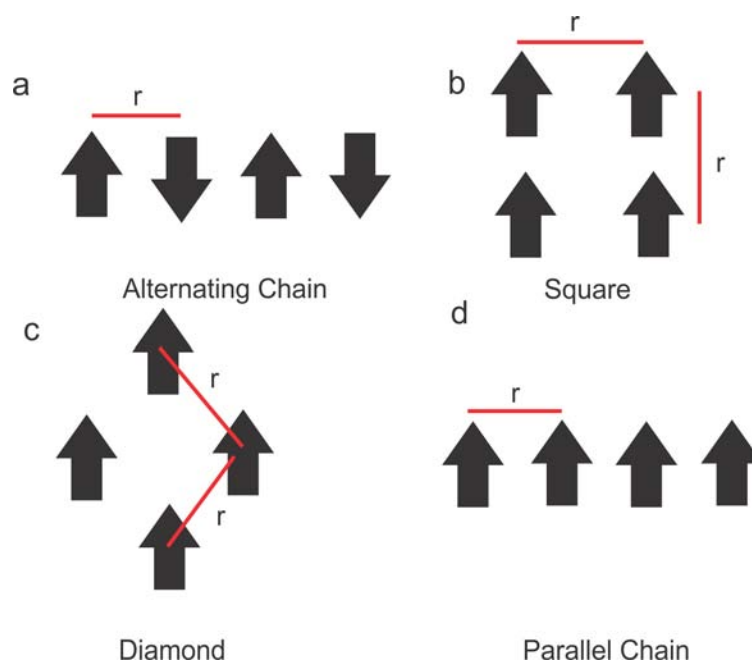
Figure 2.4: Four dipolar configurations for which the energy was calculated using Equation 2.2 and 2.3. Results are plotted in Fig. 2.5

the square configuration becomes increasingly favorable as the dipole separation is shortened. This is because the positive and negative charges from neighboring dipoles are much closer than in the other configurations. For example, at r = 0.6 nm, for the square configuration, neighboring opposite charges are within 1 Å of each other. Whereas for the alternating chain, neighboring charges are six times further apart. Hence the square configuration has a much lower energy.

It is worth noting that the total magnitude of these energies is very low. Even in the extreme case of the square configuration and a spacing of r = 0.6 nm, the energy is less than 10 meV. The energy difference between configurations is, at most, about 10 meV, and typically less than 1 meV. These are very small energies as compared to the energies of typical chemical bonds and on the order of weak van der Waals forces. Table 2.2 displays typical bond strengths for commonly observed interactions. From this it is clear that dipole-dipole forces are roughly comparable to other weak forces

such as van der Waals and CH- interactions. Dipolar forces are only a signi cant factor in the absence of stronger bonds and if the dipole moment is large.
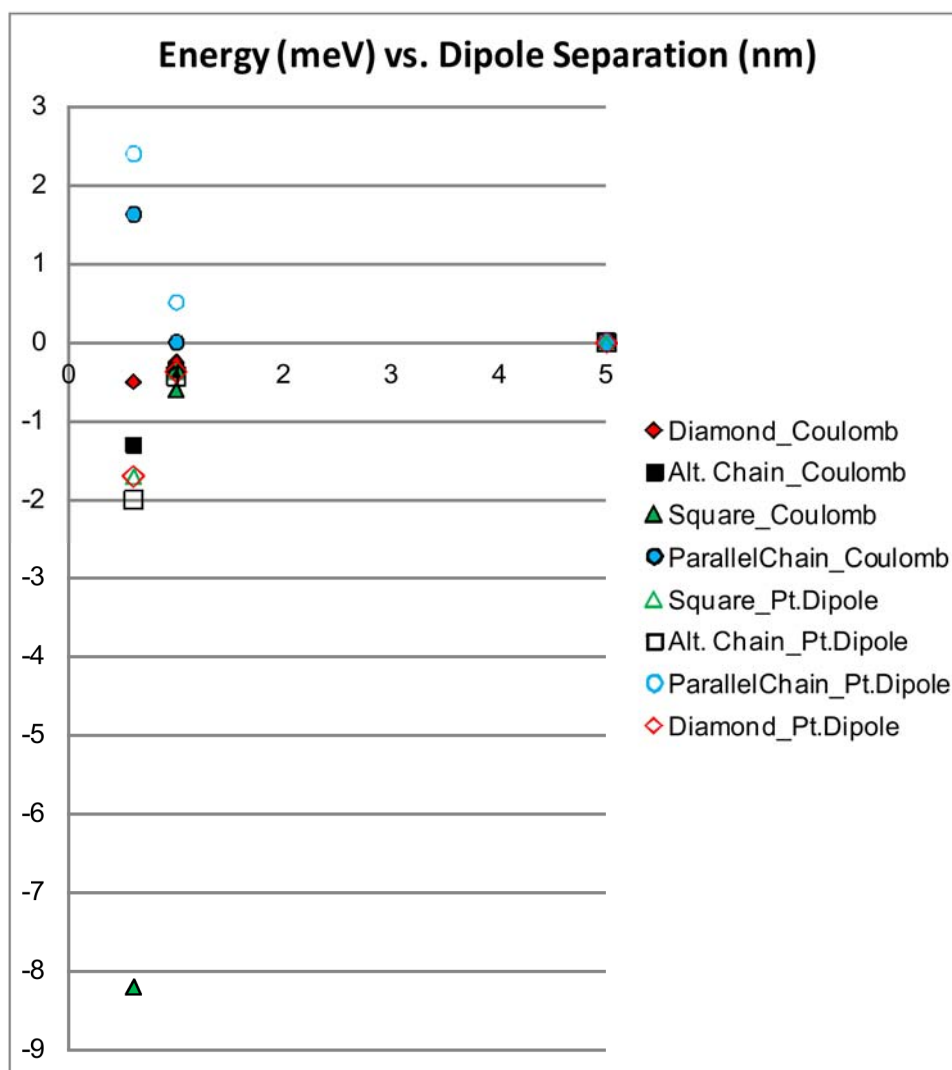
Figure 2.5: Energy/molecule of the con gurations shown in Fig. 2.4. Pt. Dipole indicates the energy was calculated with Equation 2.2 and Coulomb indicates the use of Equation 2.3.

Given the observed energies, one may ask what role dipole energy minimization plays in driving the self-assembly of dipolar molecules. Thus, simulations are needed to determine what con guration has the lowest energy, and to compare that energy with other comparable energies, such as hydrogen bonding. However, such calcula-

Table 2.2: Typical Bond Strengths for Common Molecular Interactions.

Bond Type	Energy (eV)	Reference
Van der Waal	<0.05	[26]
Dipole-dipole	0.02−0.08	[26]
CH-π	0.06∼0.1	[27]
π-π	∼0.1	[27]
Hydrogen (moderate)	0.17−0.65	[28]
Metal-ligand	0.5∼2	[27]

tions are excedingly rare. Talapin *et al.* calculated the dipolar energies of inorganic nanoparticles with an extremely large dipole moment of 100 D (which is an order of magnitude larger than any organic molecule – see Table 2.1) and a radius of 5.8 nm, for three layer systems [29]. Van der Waals forces were nearly constant for all the arrangements considered and did not impact the relative energetics. Diagrams of the three most energetically favored configurations are shown in Fig. 2.6. It is worth noting that even with a 100 D dipole moment, the lowest energy, -39 meV/particle, is much less than a typical hydrogen bond, 170-650 meV. On the basis of the considerations in this section, I will discuss dipolar effects in 2D molecular networks in Chapter 3.

-35.55 meV   -35.66 meV   -39.33 meV
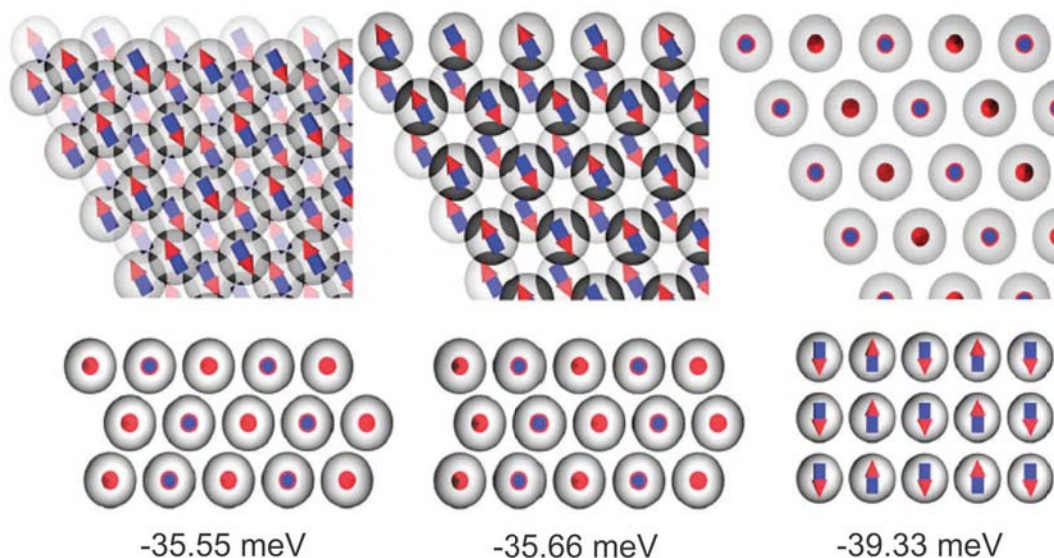
Figure 2.6: Top (above) and side (below) views of the three most energetically favored con gurations. Reproduced from reference [29].

2.1.2 Resonance Assisted Hydrogen Bonding

One speci c type of hydrogen bond important to this thesis is resonance assisted hydrogen bonds (RAHB). RAHB occur when two or more resonant structures exist and are coupled with di erent locations of a proton in a hydrogen bond. The di erent resonances strengthen the hydrogen bond, in e ect shortening the H-bond length. - electron delocalization is increased due to the resonance. The e ect is a two-fold synergistic strengthening of both H-bonds and -electron delocalization. A simple example of RAHB is seen in a carboxylic acid dimer, shown in Fig. 2.7. In this gure, two locations of each hydrogen bond are possible and each corresponds with a particular -electron geometry. The real structure is not just a rapid switching between these two, but is a hybrid of these, in which the electrons are delocalized and the energy is lower than either of the individual components.

RAHB exist for a wide range of other molecules, such as diketone enols [31], carboxylic acids [32], and inorganic acids like cacodylic acid [33]. Of particular

Figure 2.7: Hydrogen bonded dimers of carboxylic acid. The two resonances serve to strength the H bond and delocalize the -electrons, thus making this a simple example of a resonance assisted hydrogen bond (RAHB). Reproduced from reference [30]

relevance to this thesis, ferroelectric organic crystals such as croconic acid and 3-hydroxyphenalenone (3-HPLN) exhibit RAHB, and those bonds are in fact the reason for their ferroelectricity [20, 34], as is explained later. In general terms, the formula $A=R_n \quad DH$ describes systems for which RAHB are possible, where A is the acceptor atom, D the donor atom, and R_n (n=1,3,5...) is a resonant chain of alternating single and double bonded atoms.

Importantly, some RAHB have the e ect of increasing the electric polarization of the organics participating in the bonds. This mechanism is demonstrated through the example of the -diketone fragment shown in Fig. 2.8, in which one of the resonant structures may have a net dipole moment due to partial charges on the acceptor and donor atoms. The unpolarized structure is shown in Fig. 2.8(1a) and the polarized form in (1b). The location of the proton in the hydrogen bond (whether inter or intra-molecular) serves to partially balance out this charge and make the ionized structure more energetically favorable. This, in turn, increases the overall polarity of the molecule by having a higher contribution of the polar resonance to the overall structure.

Two molecules, 3-hydroxyphenalenone (3-HPLN) and croconic acid (CA), which are examined in signi cant detail in Chapters 4 and 5, exhibit electric polarization and, in fact, ferroelectricity, due to their formation of RAHB. 3-HPLN possesses a ketone-enol structure which ts the general criteria for RAHB formation as discussed
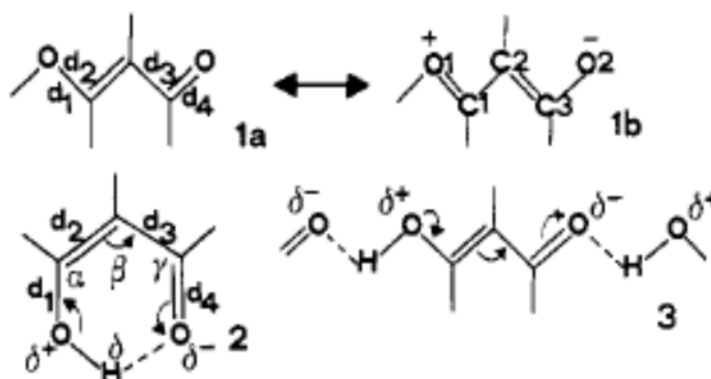
Figure 2.8: (1a) -diketone fragment in a non-polar and (1b) polarized form. When intramolecular (2) or intermolecular (3) hydrogen bonds form, they enhance the stability of the two resonances thus enhancing -electron delocalization and polarization. Reproduced from reference [31].

above [20]. Ketone and enol end groups are illustrated in Fig. 2.9. The two resonant structures of 3-HPLN are shown in Fig. 2.10 (a). A polarization forms from the unequal charges on the ketone and enol fragments. In its crystalline form, CA forms hydrogen bonded sheets [34]. Similar to 3-HPLN, the molecule consists of ketone and enol end groups. Due to the increased number of H atoms per molecule compared with 3-HPLN (2 compared with 1) the two possible resonant structures correspond with a more complicated switching of the bonds. As shown in Fig. 2.10 (b), the resonant structures correspond with -electrons moving in such a way that the ketone and enol groups are reversed. Again, the polarization arises from unequal charges on the ketone and enol groups.

16
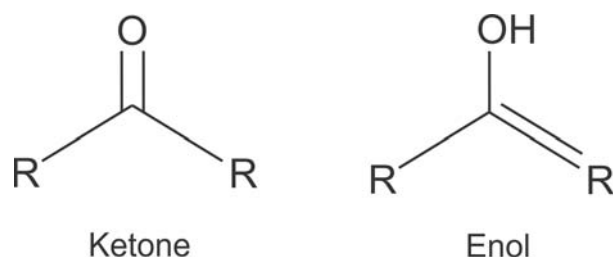
Figure 2.9: Ketone and enol groups which participate in RAHB.
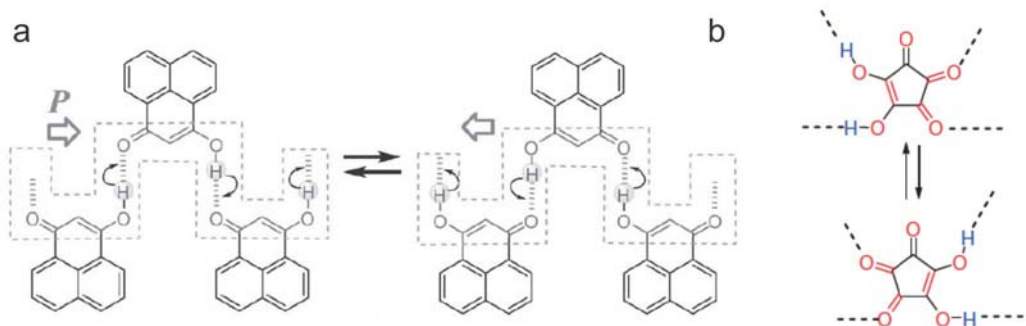
Figure 2.10: (a) Resonance structures of 3-hydroxyphenalenone, which exhibit resonce assisted hydrogen bonding. The resulting electric polarization runs parallel to the chain direction [20].(b) Resonance structures of croconic acid in the ferroelectric crystal phase [34].

The study of RAHB on metal surfaces is still in its infancy. An early study attributed the bonding of guanine quartets on Au(111) to RAHB [35]. However, this has since been disputed [36]. This thesis will examine the bonding of organic species that participate in RAHB in the bulk, on metal surfaces to further understanding of this topic.

2.2 Review of Experiments of Dipolar Molecules on Surfaces

In the last decade many experimental studies have been performed to address the fundamentals of metal-organic systems. Photoemision spectroscopy has allowed for the precise measurement of the interface electronic structure of organic-metal systems [22, 37–39]. Kelvin probe force microscopy has allowed for the detection of changes in surface potential with lateral detection below 1 μm [40,41]. Scanning tunneling microscopy is useful for studying the self-assembly and electronic properties of adsorbed molecules with sub-molecular spatial resolution [42–44]. Dipole-dipole interactions of organics on a surface can now be tested in real space [23,45–48]. Here, a review of experimental results of both the interface electronic structure of dipolar molecules and their self-assembly is presented.

2.2.1 Electronic Effects of Dipolar Molecules on Surfaces

In the simplest picture, the deposition of a polar organic adlayer results in changes to the workfunction that correspond to the direction of the dipole layer. Specifically, if dipoles point into the substrate the workfunction is increased, and if they point out of the substrate the workfunction is decreased. However, as will be shown for a variety of cases below, this change in the workfunction can sometimes be overcome by effects stemming from charge transfer and charge rearrangement, leading to the opposite results.

A large number of the earlier studies on self-assembled monolayer (SAM) interface electronic structures were performed on alkanethiols. Alkanethiols are S terminated compounds, which have long C chains with tunable end groups. Modifying the end

groups results in a controllable dipole moment, as illustrated in Fig. 2.11. Because they form uniform self-assembled monolayers on a variety of metal surfaces, they became a prototypical example of dipolar organic adlayers. Varying the substituent group was found to either increase [49 52] or decrease [49 52] the surface potential, and hence the workfunction of the supporting noble metal surface. Charge transfer was found to be larger on Ag than Au, which resulted in a greater change in workfunction for the Ag surface. [49]. Additionally, for alkanethiols the change in workfunction of a metal surface was found to vary linearly with length of alkane chain [40, 53].
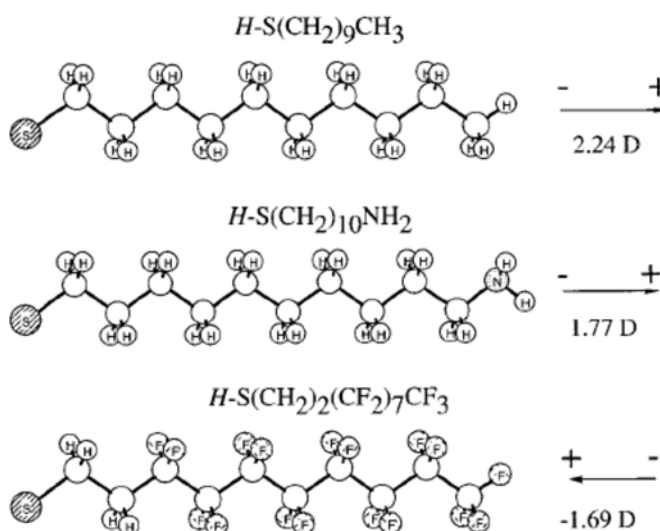
Figure 2.11: Illustrations of three alkanethiols demonstrating their tunable dipole moment [51].

Many other S-containing molecules have been studied, other than alkanethiols. These molecules, like alkanethiols, bind to the metal surface by the S-atom. On Au, areanethiols can be sucessfully modeled as two sheets of dipoles, one created by the molecule itself and one from the S-Au charge transfer at the interface [54]. A variety of compounds that bind to Au [54 56] and $CuInSe_2$ [56] through S atoms vary the workfunction of the underlying substrate at levels which correspond to their dipole

moment. Furthermore, Bruening *et al.* found that the surface potential varies with the coverage and the orientation of the ligands [56]. Adsorbtion of photoswitchable azobenzenes was found to reversibly switch the workfunction of Au, as shown by Qune *et al.* [57]. Further, by examining two chemically different azobenzenes, which each had varying dipole moments corresponding to their respective cis and trans configurations (i.e four different cases), the changes in workfunction could be separated into components from charge transfer and intrinsic dipole moment.

Non-S containing molecules have been examined, especially in more recent years. Three large π conjugated molecules with large dipole moments, GaClPc [21], SubPc [22], and VONc [37] were studied on Cu(111), Ag(111), and Au(111) respectively. GaClPc and Subpc adsorb with the Cl down and the workfunction of the metal is decreased. Suprisingly, the dipole moment of VONc points in the opposite direction, yet the workfunction of the metal is decreased in this case as well. DFT calculations reveal that this is due to significant charge rearrangement which more than compensates any effects of the permanent dipole moment. This demonstrates that the orientation of the dipole moment cannot always be used to predict whether the work function will increase or decrease upon the adsorption of an organic layer. Koch *et al.* determined that a large non-polar pentacene derivative (PFP) aquires a significant dipole moment (0.5 D) caused by a geometric distortion when adsorbed onto Cu(111) [58]. This adsorbtion induced dipole moment modifies the interface electronic structure, highlighting the importance of adsorption geometry.

Organic species tend to interact more weakly with HOPG than with metal surfaces, often resulting in a change of the workfunction that directly corresponds to the direction of the dipole moment of the organic adlayer. Examples of this include phthalocyanine species with a variety of dipole moments adsorb onto HOPG such that the dipole moment points toward the surface. In all cases, this results in an

increase of the workfunction by < 0.5 eV [59]. One complicating factor, however, is that the self-assembly of these molecules does play a crucial role. In the case of ph-thalocyanine, a second layer adsorbs with the opposite orientation of the first, thereby diminishing the effect the first layer has on the workfunction. A thin dipole layer of OTiPc adsorbs onto HOPG with a downward facing dipole, which increases the work-function by approximately 0.21-0.35 eV [60]. When VONc is deposited on HOPG, the change in workfunction (increase of 0.2 eV) directly correlates with the direction of molecular dipole moment (downwards) [61], which is in contrast to the observed result on Au in which a downward facing dipole moment results in a decrease in the workfunction [37].

2.2.2 Self-Assembly of Dipolar Molecules

The self-assembly of dipolar molecules is critical to organic-molecule interface elec-tronic effects because the direction that the dipole moment faces can directly influence the energy level alignment. Similarly, the adsorption geometry can determine charge transfer, as will be shown below. Whether or not the molecular self-assembly is driven by electrostatic considerations is still an open question. Many studies have been undertaken to explore these considerations. Here I review the self-assembly of dipolar molecules examined at the liquid-solid interface, under ambient atmospheric conditions, and under UHV. Dipolar molecules studied with perpendicular and par-allel attachment geometries are discussed, followed by apolar molecules which adopt a dipole moment through surface interactions.

Numerous studies explore the self-assembly of dipolar anthracene molecules with extended alkane side chains, at the liquid-solid interface. These studies focus on modifying the long alkane chains with dipolar components, including ether [62–65]

and ketone [66] groups. In general, the studies focus on the competition of attractive van der Waals forces between the alkane chains with either repulsive or attractive dipolar effects. The length of the side chain, including even/odd effects [65] and the location of the dipolar groups [66], drives the molecules into a variety of assemblies, as is illustrated in Fig.2.12 (a)-(c). Assemblies ranging from anti-parallel dipoles (a) [63–66], parallel aligned diople moments (c) [65, 66], and even a herringbone pattern (b) [65] were observed. Often, multiple phases were observed on the same sample [64, 65]. However, by modifiying the location of the dipolar groups, the amount of polymorphism could be controlled [64]. Co-crystals were grown with a variety of anthracene compounds [62, 63, 66]. Examples of parallel alignment of the dipole moments in anthracene cocrystals are illustrated in Fig. 2.12(d),(e).

Also at the liquid-HOPG interface, several groups have investigated the effect a dipole moment in the central, conjugated part of an organic molecule has on self-assembly. Xu *et al.* reports the co-existence of two different polymorphs, one cyclic, see Fig.2.13(a), and one linear (b), which correspond to slightly different adsorption geometries of the molecule [26]. Calculations reveal that the linear structure maximizes van der Waals attraction, while the cyclic one maximizes dipolar attractions. Surpisingly, a study on polar oligothiophenes found pairs of anti-parallel aligned molecules (Fig.2.13(c)) [67], despite the fact that anti-parallel dipoles are repulsive, as demonstrated earlier this chapter. One study examines zwitterionic molecules, which have a high in-plane dipole moment of about 10 D [68]. Unlike the previously discussed cases, the molecules are capable of forming hydrogen bonds when bound in an anti-parallel alignment, see Fig.2.13(d). This particular configuration also allows for strong van der Waals attraction between interdigitated alkane chains.

In all the examples described above, the long ligands have significant steric inter-actions which must influence the self-assembled geometries observed. More compact
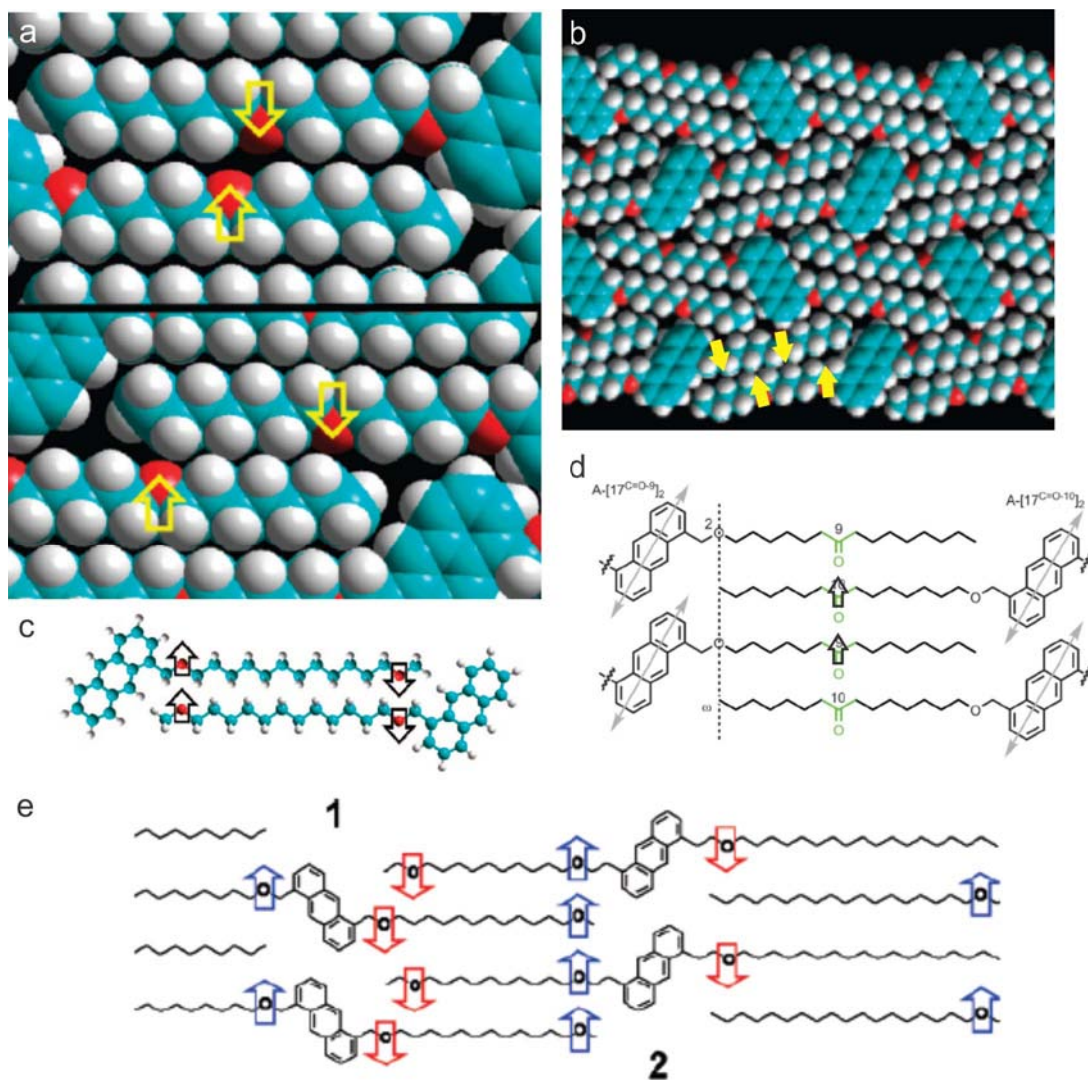
Figure 2.12: Anthracene compounds modi ed to have a dipole moment self-assemble into a wide range of structures, which includes (a) opposite facing dipoles [64], (b) a honeycomb pattern [64], (c) parallel alignment of dipoles [65]. Co-crystals of di erent anthracene compounds have formed parallel alignment of the chains as illustrated in (d) [66] and (e) [63].

molecules have been studied at the liquid-solid interface, under ambient conditions, and under UHV. First, I discuss molecules which adsorb such that their dipole moment points perpendicularly to the surface, followed by a comparison to molecular adsorbates with a dipole moment parallel to the surface plane.
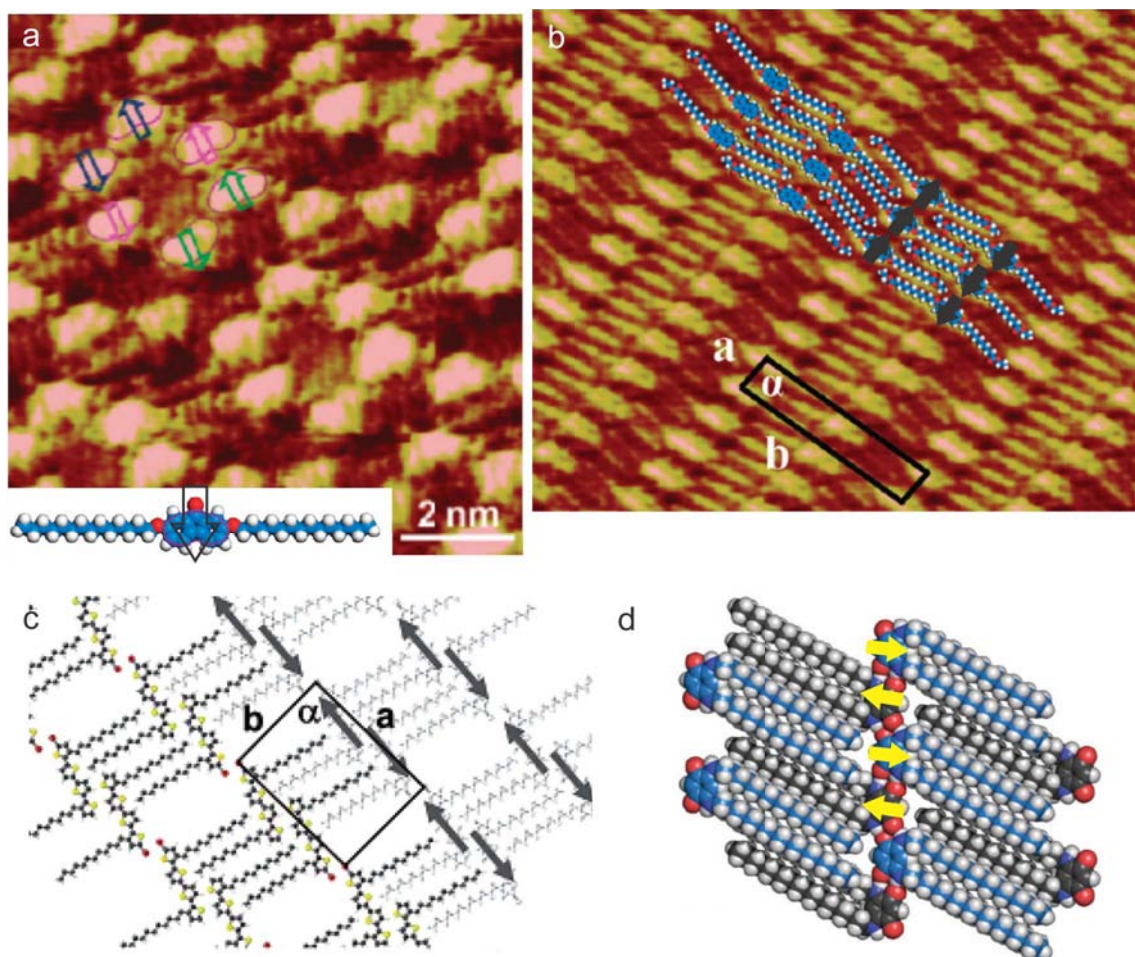
Figure 2.13: Organic species with long ligands and a dipolar core have been studied at the HOPG/liquid interface. Observed self-assembled structures observed are (a) A cyclic con guration [26], (b) Linear chains [26], (c) Tail to tail pairs of dipoles [67] and (d) Alternating chains [68].

Experiments show that adsorbates with a dipole moment perpedicular to the surface form a variety of di erent seemingly unrelated network structures. On Cu(111), Ir(ppy)$_3$ attaches with the dipole moment pointing towards the surface [24]. At all coverages the molecules are repulsive and remain isolated from each other, as is shown in Fig. 2.14(a). From analysis of the average spacing, the surface state of Cu is ruled out as a factor, which is found relevant in other structures [69 71]. Instead, the authors rationalize the intermolecular repulsion by repulsive dipole-dipole interactions.

They are able to model this repulsion if, through surface interactions such as an image dipole, the dipole moment was increased to approximately 9.2 D, which is significantly greater than the gas phase value of 6.5 D. In contrast, bowl shaped hydrocarbons (corannulene and methylcorannulene) both aquire comparably large dipole moments of 6 and 9 D respectively when adsorbed onto Cu(111), yet these molecules form close packed networks with all the dipole moments aligned, as shown in Fig. 2.14(b) [72]. Other studies demonstrate close packed networks of aligned out of plane dipoles on Ag(111) [22], under ambient conditions on Au(111) [73], and under UHV conditions on Au(111) with about 80% alignment of dipoles. Of particular interest, Toader *et al.* discovered that SnPc adsorbed on Ag(111) has a smaller dipole moment when adsorbed with Sn-down compared to Sn-up. Importantly, only two dipolar configurations, one in which all dipoles point down and one in which the molecular dipoles alternate up/down, were observed, see Fig. 2.14(c). Up only congregations were never observed, implying that these were repulsive due to the larger dipole moment.

Remarkably, in two instances STM tip-induced dipole switching was reported for molecules with a dipole moment perpendicular to the surface. Namely, ClAlPc selectively adsorbs into the holes of a SiC nanomesh forming an ordered array [74]. As deposited, the dipole moment of the ClAlPc aligns with the dipole moment of the underlying lattice, which points perpendicular to the surface plane. By scanning with an STM tip or performing a voltage pulse of the tip of a magnitude greater than 3.3 V, the orientation of the molecular dipole moment can be reversed, accompanied by a shift in the adsorption position. While this switching is irreversible, the same molecule deposited onto HOPG can be reversibly switched into an up or down configuration with voltage pulses [23].

The following studies have examined the self-assembly of polar organic molecules that adsorb to surfaces with the orientation of the dipole moment parallel to the
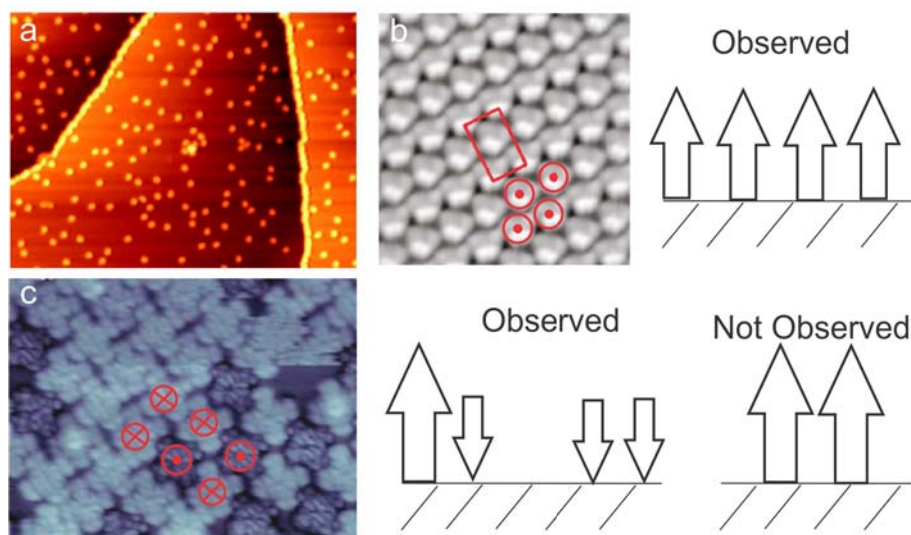
Figure 2.14: Self-assembled structures reported for perpendicularly attached dipole moments. Structures include (a) Repulsive single molecules [24], (b) Close packed structures [72], and (c) A mixture of aligned dipoles and alternating up/down close packed networks [48].

surface plane. The organic species 1,5-dichloropentane displaces Si surface charges upon adsorption, which drives it to self-assemble into 1-D electret lines [45], displayed in Fig. 2.15(a). Kuck *et al.* examined salen complexes that were modied both with and without a dipole moment on Cu(111) [46]. The non-polar species repel each other, while the addition of an inplane dipole moment leads to a porous 2-D network shown in Fig. 2.15(b). At the liquid solid interface, Mu *et al.* investigated a large, conjugated, C_3 symmetric molecule which was functionalized to have a dipole moment on end groups, and also functionalized to not have a dipole moment for comparison [75]. It was found that adding dipolar groups switched the self-assembled structure from a close-packed hexagonal network into a porous honeycomb network due to an anti-parallel alignment of the end groups, illustrated in Fig. 2.15(e). 4-uorstyrene was examined on both Cu(111) and Au(111) [76], however, calculations demonstrate that surface interactions actually modify the dipole moment such that

it is larger (approximately by a factor of 2) and out of plane. The molecules form magic clusters, comprised of three molecules on Cu and four molecules on Au with the di erence in cluster size attributed to unequal charge uptake (and thus dipole moment) in the two cases.
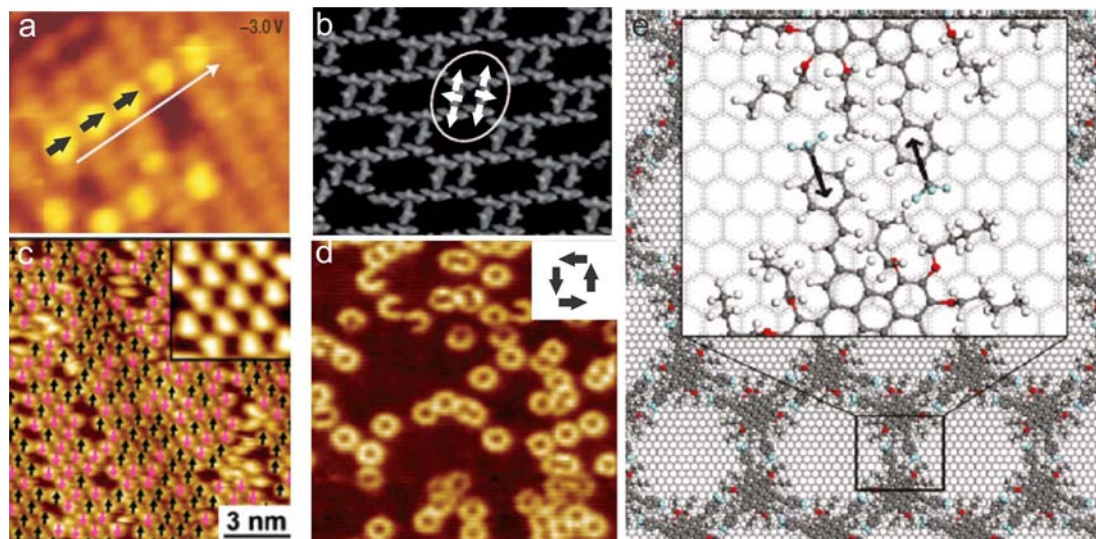
Figure 2.15: Self-assembled structures reported for organics with an in-plane dipole moment. Structures include (a) lines [45] (b)Porous 2-D networks [46]. (c)Aligned 2-D domains [77] (d) Rings [78] and (e) Honeycomb networks [75]. Arrows indicate direction of dipole moment in all cases.

Further highlighting the importance of changes in dipole moment upon adsorption to a metal surface, styrene is nearly non-polar in the gas phase but aquires a signi cant in-plane dipole when adsorbed on Ag(100) [78]. This dipole moment was found to drive the self-assembly into small clusters of four or eight molecules, seen in Fig. 2.15(d). While the dipole moment was not calculated for adsorption onto Au(111), styrene aligns parallel locally as illustrated in Fig. 2.15(c). Surprisingly, when adsorbed onto Ag(111), styrene did not aquire a dipole moment due to the di erent adsorption geometry. Lending further evidence of the importance of surface charge transfer/rearrangement is the study of TTF of Au(111) [79]. Through charge

transfer TTF aquires a dipole moment out of the plane of nearly 5 D and the molecule is charged to such an extent that its Coulombic repulsion outweighs other attractive forces.

As can be seen, much progress has been made towards understanding how dipolar molecules self-assemble on surfaces. However, there remain open questions. For example, molecules that have similar dipole moments that point perpendicular to the surface plane repel each other on one surface [24] and attract each other on another [72]. This indicates that the dipolar interactions are only one part among several complex interactions. Many studies of dipolar molecules ascribe the ordering of the molecules to their dipole moment. However, the variety of structures reported for dipolar molecules, such as those seen in Fig. 2.15, can only mean that most of them are not in the energetically favored diople configuration, which was shown earlier in this chapter. This means that there must be other factors contributing to the self-assembly of these structures that dominate over dipolar interactions. Another current challenge is that the dipole moment of a molecule in the gas-phase often changes substantially after deposition on a surface, as was discussed above. The dipole moment can even depend on the crystal orientation of the surface. This thesis aims to systematically study strongly dipolar molecules on various surfaces to establish the role of the intrinsic dipole moment during organic self-assembly.

2.3   Molecule Surface Interactions

The utilization of organics in devices often requires their deposition onto a supporting substrate. It has been shown that interactions with the substrate can be significant [9,43,47]. Some observed effects are band alignment and broadening, charge transfer, modification of the surface workfunction [1], alterations of carrier density [11], the

emergence of new electronic states due to the hybridization of organic and metal orbitals [12], and even the emergence of magnetism [13]. These effects can be utilized as parameters to tailor material properties [80]. Fundamental interactions between organics and surfaces are first discussed, followed by more technical aspects of current theories.

2.3.1 Short Review of Clean Metal Surfaces

Before discussing how molecules interact with metal surfaces, it is worthwhile to first review a few basic concepts of clean metal surfaces. Every metal surface has an inherent dipole moment pointing inwards toward the surface. This can be readily understood by examining a simple theoretical model: the jellium model. In this model, the positive ionic lattice of a crystal is assumed to be uniformly distributed throughout the bulk material. The electrons do not terminate sharply at the surface, however, and some electron density is present in the vacuum region outside the surface. This electron "spillout" is compensated inside the bulk, resulting in Friedel oscillations of the electron density. The resultant distribution of electron density creates an inward pointing surface dipole moment, illustrated in Fig. 2.16. The jellium model reflects the intuitive physical picture, in which a regular bulk lattice of positive ions is surrounded by electron clouds. When a surface is created, the lattice terminates in negatively charged electron clouds, creating a surface dipole.

The workfunction is defined as the energy to remove an electron from inside the bulk of a metal to a macroscopic distance away. Many factors influence the magnitude of a workfunction. An increase in the interface dipole correlates to a larger workfunction, because an electron must move against the electric field created by this interface dipole. The connection between interface dipoles and workfunctions can be
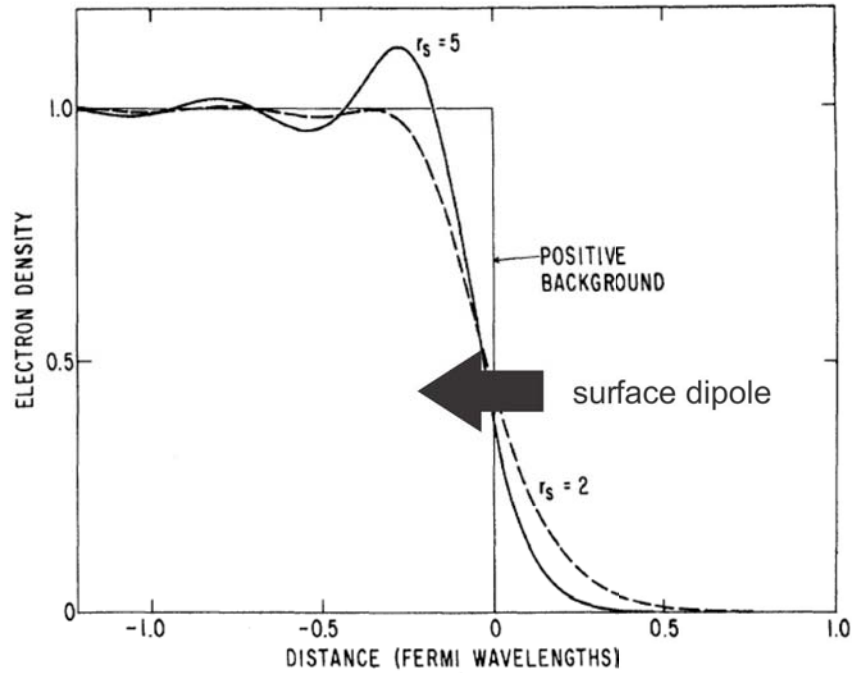
Figure 2.16: In the jellium model, electron denisty oscillates as it approaches the surface leading to a surface dipole. Adapted from reference [81].

seen by examining different crystal faces of a metal, which have different densities of electrons, resulting in different magnitudes of interface dipoles [82]. For example, for W the work function of the (111) face is 0.78 eV lower than for the (110) face, which corresponds to the lower electron density of the (111) face [83].

Monatomic steps in a metal surface have the effect of lowering the workfunction [84]. In terms of the jellium model, electron clouds still extend outwards into the vacuum but the contributions from one step partially cancel out the contributions from another layer. This effect has even been measured with STM in which laterally resolved maps of the workfunction appear darker, corresponding to a lower value of the workfunction, at monatomic steps [85].

Table 2.3: Catagories of molecule metal interaction strengths. Charge transfer is abbreviated CT, Induced Density of Interfacial States is IDIS, and Integer Charge Transfer Model is ICT.

Strength	Type of Bonding	Charge Transfer	Relevant models
Weakest	Weak Physisorption	None	Only Pauli Repulsion
	Physisorption	Possible Integer CT	ICT
	Weak Chemisorption	Possible Partial CT	IDIS
Strongest	Covalent Bonding	Partial CT	Case by case

2.3.2 Molecule-Substrate Interaction Strengths

Organic metal interactions range from very weak physisorption to strong covalent bonding. No single model accurately describes all interfaces, and thus catagories of interactions are useful. Table 2.3 provides a summary of the classes of interaction strengths and what models are typically used to describe these cases, based on reference [17]. Though an interaction may be termed "weak", the observed physical effects can, however, be significant. For example, bowl shaped hydrocarbons called corannulene induce a dipole moment of approximately 8.8 D on Cu(111), despite nearly no charge being transfered to or from the molecule [72].

2.3.3 Energy Level Alignment

Upon adsorption to a metal surface, the energy levels of the organic and metal can align in a number of ways, depending on the strength of the interaction. In the weakest case of physisorption with no charge transfer, the energy levels of the organic molecule may shift slightly but do not align with those of the metal surface.

For slightly stronger physisorption, the integer charge transfer (ICT) model accurately describes the energy level alignment of certain organic/metal systems. In particular, this model typically describes interfaces which are created under ambient atmospheric conditions in which atmospheric adsorbates passivate the sample and

limit interaction strength [17]. In this model, two new molecular energetic states are defined. The positive (negative) integer charge transfer state E_{ICT+} (E_{ICT-}) is that for which one electron (hole) has tunneled into the surface and the molecule has been relaxed geometrically, with screening from the substrate taken into account. This results in three different regimes depending on the workfunction of the surface. The first regime is that for which the workfunction of the bare metal (denoted Φ_M) is $\Phi_M > E_{ICT+}$, illustrated in Fig. 2.17 (a). In this case, an electron tunnels from the molecule to the surface, resulting in the Fermi level of the metal aligning with the positive integer charge transfer state. Note that this results in an offset of the vacuum levels of the molecule and metal, labeled Δ in Fig. 2.17. The second case, when $E_{ICT-} < \Phi_M < E_{ICT+}$, results in energy level alignment, $\Delta \approx 0$, as is illustrated in Fig. 2.17(b). Finally, Fig. 2.17 (c) illustrates the third regime, when $\Phi_M < E_{ICT-}$. This results in the transfer of an electron from the surface to the molecule, and the Fermi level of the metal is pinned to the negative charge transfer state.

For interfaces in which the organic species weakly chemisorb to the metal, i.e. those described by the induced density of interfacial states (IDIS) model, the energy levels align in a different way. Upon adsorption to a metal surface, the molecular orbitals broaden from discrete lines into bands, shown in Fig. 2.18. The red line marked CNL represents the charge neutrality level. It is defined such that the integral of the density of states up to the CNL is equal to the charge of a neutral isolated molecule, as in Equation 2.4.
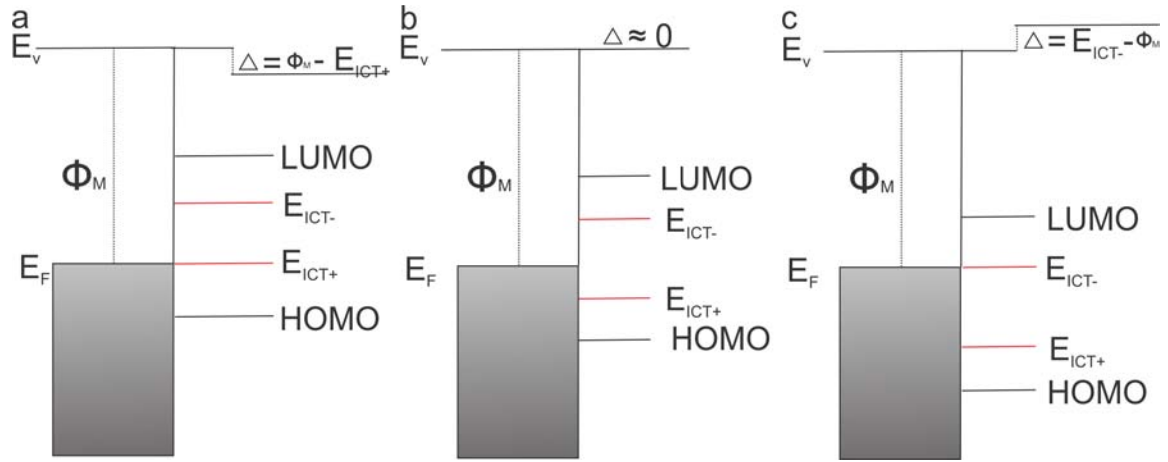
Figure 2.17: Energy level diagrams for the three cases of the ICT model. (a) Fermi-level pinning to E_{ICT+} when the metal workfuction is greater than E_{ICT+} (b) Vacuum level alignment when the workfunction of the metal is between the two charge transfer energy states. (c) Fermi-level pinning to E_{ICT-} when the workfunction is less than the E_{ICT-}

$$\int^{CNL} DOS(E)dE = N \qquad (2.4)$$
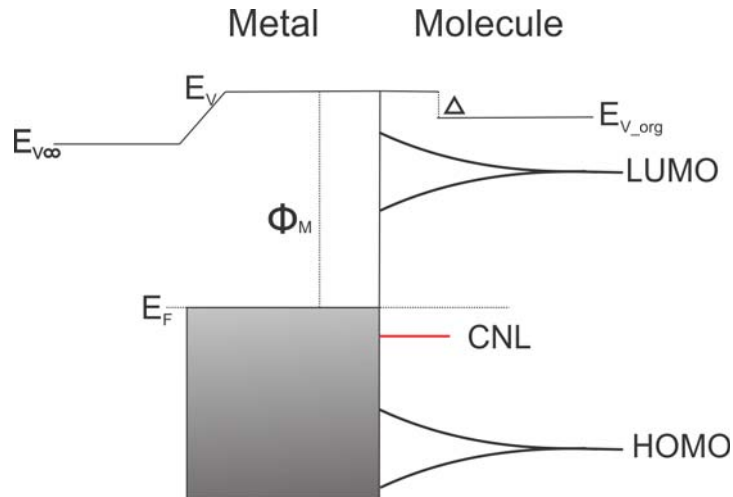
Figure 2.18: Illustration of a typical band diagram for weakly chemisorbed organics.

Note that the DOS is not, in general, symmetric about the HOMO-LUMO gap.

Because of this asymmetry, the CNL is located closer in energy to the molecular orbital with higher density of states. The energy levels of the organic shift such that $E_F \approx CNL$. The reason this is not an exact equality is that the surface has screening effects. These are taken into account in the IDIS model, the details of which are provided in Section 2.2.6.

As alluded to in Table 2.3, for strongly reactive interfaces and those with strong covalent bonds, each scenario must be analyzed on a case by case basis. This is because there currently are no general models which successfully describe all of these [17].

2.3.4   Interface Charge Transfer

For the weakest molecule/metal interface interaction, no charge is transferred across the interface. This is typically obseved for noble gases or saturated hydrocarbons on clean metal surfaces [17].

Organic/surface interfaces that are successfully described by the integer charge transfer model typically involve molecules with π conjugated electron systems. In these compounds, the π electrons in the organic do not hybridize with metal states [17]. Thus, charge can only transfer through tunneling because of the lack of hybridization. Depending on the relative energies of the metal workfunction and molecular orbitals, three cases exist. The molecule can gain an electron, donate an electron, or have vacuum level alignment (with no charge transfer). Experimentally, this is observed by measuring the workfunction of the combined molecule/surface interface and comparing it to the bare surface workfunction. The resulting plot is often termed a "mark of Zorro" plot, in which three clear regimes are observed, corresponding to one electron transferred, no charge transferred, or one hole transferred. For most π conjugated compounds studied, the energetic gap between positive and negative charge

transfer states is too large to experimentally access all three regimes [17]. However, Crispin *et al.* demonstrated that for low band gap polymers (such as alternating poly uorene-green1) all three regimes can be experimentally veri ed, as shown in Fig. 2.19 [38].
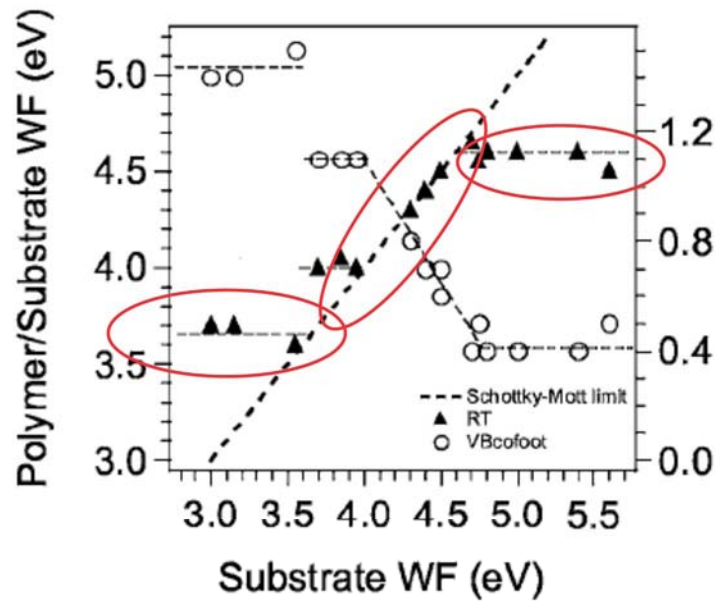
Figure 2.19: Three charge transfer states (highlighted by red ellipses) representing 1 hole tranferred (far left), no charge transfer(center) and 1 electron transferred(right), which occurs with physisorption between organic adsorbates and surfaces. Adapted from reference [38].

For weakly chemisorbed systems, such as those described by the induced density of interfacial states (IDIS) model mentioned above, molecular orbitals hybridize with metal wavefunctions. This results in non-integer charge transfer. The quantity of charge transferred is determined by the charge neutrality level (CNL) as de ned previously. If the CNL is located above the Fermi level of the metal, charge will transfer to the metal, and if the CNL is below the Fermi level, charge will transfer from the metal to the organic. This occurs until the CNL approaches the Fermi level of the metal (CNL E_F). This is part of the basic framework of the uni ed IDIS

Table 2.4: Charge transfer at the metal organic interface. Charge transferred to the surface is listed as positive.

Organic Species	Metal Surface	Charge to Surface(e)	Method	Reference
VONc	Au(111)	0.7	Calculation	[37]
F_4-TCNQ	Cu(111)	-1.8	Experiment	[12]
PTCDA	Ag(111)	-0.6	Calculation	[86]
4-Fluorostyrene	Cu(111)	0.3	Combined	[76]
4-Fluorostyrene	Au(111)	0.2	Combined	[76]
Corannulene	Cu(111)	0	Combined	[72]
ClAlPc	Cu(111)	-1.3	Calculation	[44]
TTF	Au(111)	0.43	Calculation	[87]

model, which is discussed in greater detail in Section 2.2.6.

Many experiments and calculations have been performed to compute the charge transfer occuring at a metal/organic interface. These values range from zero to over 1 e. For reference, some examples of organic/metal charge transfer values are provided in Table 2.4.

2.3.5   Pauli Repulsion

Regardless of the strength of interaction, from the weakest physisorption to the strongest chemisorption, when a molecule or atom is adsorbed onto a metal surface, the electronic wave functions of both the adsorbate and metal overlap. These overlapping electrons experience Pauli repulsion, i.e. two identical Fermions cannot occupy the same quantum state simulatneously. As a result, the electrons in the surface are "pushed back" into the metal and often rearrange to a ring surrounding the adsorbate, resulting in the name the pushback, pillow, or Pauli repulsion effect. The outcome of this is a change in the charge distribution at the surface, resulting in a reduction of the interface dipole of the metal, which corresponds to a lowering of the workfunction of the metal.

For molecules or atoms with filled electronic shells, such as the noble gases, the

reduction in surface dipole is particularly pronounced because the molecule s electron clouds are not easily deformed [88]. Computationally, this e ect has been successfully utilized to model Xe on Cu(111) [88] as well as cyclohexane and benzene on Cu(111) [89] and Au(111) [90]. The resulting change in interface dipole can be signi cant, exceeding 1 D in some cases [90]. This e ect is not limited to simple noble gases and hydrocarbons. Recently, Pauli repulsion was found to be the primary cause of a 0.73 eV reduction in the Au(111) workfunction for adsorbed vanadyl naphthalocyanine (VONc), even though the inherent molecular dipole pointed towards the surface and would have increased the workfunction [37]. This Pauli repulsion e ect has been visualized using laterally resolved maps of the workfunction taken with an STM [43, 91]. In the workfunction map, shown in Fig. 2.20(b), a dark ring appears around the tetraphenyl porphyrin molecule demonstrating the lowering of the workfunction in the vicinity of the molecule.
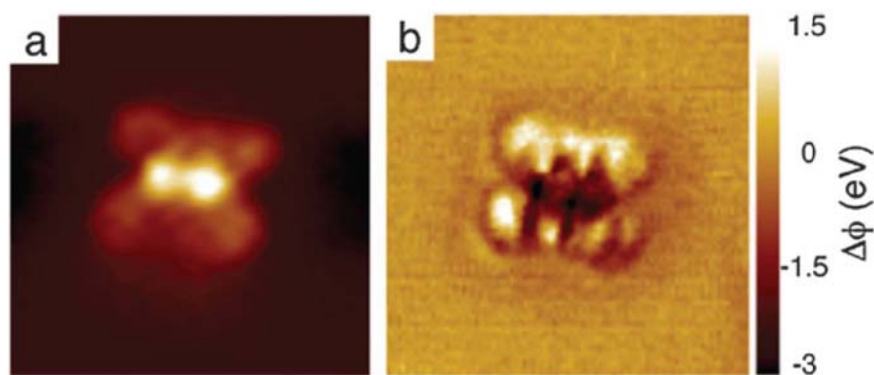

Figure 2.20: (a) STM image of TPP (b) Workfunction map in which the dark ring just outside of molecule illustrates decrease of the workfunction of Cu due to the pillow e ect. Reproduced from reference [43].

2.3.6 Unified IDIS-Pillow-Permanent Dipole Model

As mentioned in previous sections, the induced density of interfacial states (IDIS) model describes weakly chemisorbed organic molecules on metal surfaces. It has demonstrated success in accurately describing many molecule-metal junctions [1]. Furthermore, it has recently been expanded to take into account Pauli repulsion and also the contributions from a permanent dipole moment in the organic. This combined model is termed the unified IDIS model. Because it accurately describes the types of molecule/metal interfaces which are the focus of this thesis, I provide more technical aspects of this theory here.

The first step in the unified IDIS model is to calculate the molecular orbitals for a free molecule using DFT-LCAO calucations [17]. Second, each molecular orbital is broadened into a Lorentzian function due to interaction with metal orbitals [92], which, when summed, yields the density of states (DOS). From the DOS, the charge neutrality level (CNL) can be calculated as described in previous sections. The CNL can be thought of as an organic Fermi level, before interface charge transfer is taken into account. The final parameter fundamental to determining the magnitude of charge transfer at an interface is the screening parameter, S. It varies from 0<S<1, in which S close to 1 corresponds to a weak metal-organic interaction, and S close to 0 corresponds to a strong metal-organic interaction. This parameter allows the unified IDIS model to accurately represent a range of interfaces. The screening parameter is defined by:

$$S = \frac{dCNL}{d\Phi_M} = \frac{1}{1 + (4\pi e^2 DOS(E_F)d/A)} \tag{2.5}$$

where d is the distance between the metal and adsorbed organic, and A is the contact area associated with each molecule.

From these calculated values as well as the experimentally obtained work function

value, the value of the induced dipole at the interface can be calculated as:

$$\Delta_{IDIS} = (1 - S)(\Phi_M - CNL) \qquad (2.6)$$

Pauli repulsion can be successfully incorporated into the unified IDIS model as follows. An interface dipole due to the Pauli effect is given by:

$$\Delta_{pillow} = \frac{4\pi D}{A} \qquad (2.7)$$

where D is a corresponding dipole moment and A is the contact area associated with each molecule. D is calculated by expanding the organic-metal many-body interactions up to second order in the organic-metal overlap. The mathematical details are provided in reference [93]. The pillow interface dipole modifies the workfunction of the surface such that $\Phi_M^* = \Phi_M - \Delta_{pillow}$. By applying the IDIS formalism with the modified workfunction, it is shown that:

$$\Delta_{I-P} = \Delta_{IDIS} + \Delta_{pillow} = (1 - S)(\Phi_M - CNL) + S(\Delta_{pillow}) \qquad (2.8)$$

Notice that for the case of very weak molecule-metal interactions (S=1) the only effect is due to Pauli repulsion. Whereas, for the case of extremely strong interactions (S=0) the Fermi energy level is forced equal to the CNL and the pushback effect is neglible.

Molecules with a permanent electric dipole moment create an electrostatic potential which shifts the energy levels of the molecule with respect to the metal [60]. Similarly, image charges which form in the metal due to dipole layer amplify this effect for perpendicularly attached dipole layers [1]. The effects of a molecular dipole layer can be successfully incorporated into the IDIS model in a similar manner as the

pillow effect. For a molecule with a permanent dipole P, on first approximation the change in metal work function is given by:

$$\Delta_{dipole} = \frac{4\pi P cos(\gamma)}{A(1+\alpha)} \tag{2.9}$$

where α is the molecular polarizability, and γ is the angle of the dipole moment to the surface normal [94]. Then, the sum of the contributions from charge transfer, the pillow effect, and interface dipole can be simply summed as follows:

$$\Delta_{total} = S\Delta_{dipole} + S\Delta_{pillow} + (1-S)(CNL - E_F) \tag{2.10}$$

This unified IDIS model which takes into account both permanent diopoles as well as the pillow effect has sucessfully modeled certain experimental setups, such as the Cu(100)/Bt-SAM/pentacene system [94]. A review of experimental results, with a discussion of the efficacy of the IDIS model is presented below.

2.3.7 Experimental Confirmation of the IDIS Model

X-ray photoelectron spectroscopy (XPS) and ultraviolet photoelectron spectroscopy (UPS) are powerful surface sensitive tools that allow for the study of the workfunction of organics on surfaces. The IDIS model pertains to non-chemically reactive surfaces, which interact moderately with adsorbed organics. In terms of materials, Au is a very good candidate for studying the accuracy of this model. Vázquez *et al.* compiled a list of photoemission spectroscopy results and compared their IDIS calculations to the experimentally confirmed results [92]. There is remarkable corresponsdence between the theory and experiment, with the magnitude of the interface dipoles often being within 0.1 eV with respect to each other. For quick comparison, their results are summarized in Table 2.5.

Table 2.5: Inteface dipoles (Δ) for organics on Au computed with the IDIS model compared to experimental results. All theory values from reference [92].

Organic Species	Δ (eV) Theory	Δ (eV) Experiment	Exp. Reference
PTCDA	0.25	0.2	[39]
PTCBI	0.50	0.4	[95]
CBP	0.43	0.5	[96]
CuPc	0.91	1.2	[97]
α-NPD	0.70	0.86	[98]
α-NPD	0.87	1.3	[99]
Alq$_3$	0.65	0.65	[39]

2.3.8 Challenges to Interface Modelling

While the unified IDIS model is successful in describing some experimental results, it is not without challenges. The model depends very strongly on the adsorbed molecule-metal distance, which can be difficult to measure experimentally or calculate accurately [17]. Further, the model does not, in general, account for a variety of molecular orientations which can vary based on growth conditions [17].

Neither the integer charge transfer nor the induced density of interfacial states (IDIS) describe systems in which the organic molecule binds covalently to or chemically reacts with the metal. Because of the unique nature of chemical reactions, each reactive metal and organic pair must be treated on a case by case basis [92]. However, some more general statements can be made. Strongly bound adsorbates typically have a short bond length to the substrate, which increases the Pauli repulsion effect. Significant charge is transferred either to or from the surface resulting in a change of the interface dipole. In such cases, the interface dipole has been successfully modeled in terms of the relative chemical potentials of the surface and the organic species as detailed in references [17, 100]. There is some evidence that the absolute hardness, defined as the derivative of the chemical potential with respect to the number of electrons, has a strong correlation with the changes in workfunc-

tion upon adsorption of an organic species. This was demonstrated for acetonitrile on Ni, Fe, and Cu [17, 100]. However, a complicating factor is that in chemisorbed systems, metal atoms often diffuse into organic layers which causes local variations in the chemical and electronic properties of these layers. In short, while individual cases have been accurately modeled, there is not yet one single model, such as the unified IDIS model, for these systems.

Among the challenges to interface modeling that still exist is that each model is limited in the range of interaction strengths which it can describe. This means that one must be able to predict beforehand how strong the interaction will be and then select the proper model, which for intermediate cases may not always be obvious *a priori*. Additionally, the models do not account for defects or contaminations, which often make a significant difference in measured properties such as the work-function [99, 101]. A shortcoming of all of these models is their complexity. Each model requires the use of significant computing resources. Having simple approximations would greatly aid experimentalists in designing future experiments and providing quick guides to explaining experimental results. Simpler models could serve as screening tools to determine which full calculations ought to be performed.

2.4   Experimental Methods

This section first discusses the basic principles of scanning tunneling microscopy. Then, the specific STM and related experimental equipment used in this thesis are described. Finally, experimental methods related to sample preparation and imaging are detailed.

2.4.1 Basic Principles of Scanning Tunneling Microscopy

Scanning tunneling microscopy is a powerful tool for the real space probing of the electronic structure of atoms and molecules with ultimate atomic resolution. The idea behind an STM is quite simple. An STM consists of a metallic tip situated on three piezoelectric transducers (x, y, and z) where "z" is typically along the surface normal, i.e. the distance from the surface. The tip is approached very close to a conducting surface, typically less than one nm. When a voltage is applied between the tip and sample, electrons tunnel from the tip to the surface or vice versa. The tip scans latterally across the surface. In the simplest mode of operation, called "constant height mode", the tip is held at a constant z position and the current is read out as the tip scans across the sample surface. More commonly, however, a constant current mode is used in which, through use of a feedback loop, the current is held constant and the z-position is constantly adjusted to maintain that current. A computer is used to record the z-position readout.

The basic theory for interpreting STM images was described by Tersoff and Hamann in 1985 [102]. In their landmark paper, the tunneling current was considered to be proportional to the local density of states of the surface. C. J. Chen gives an excellent summary of the basic theory in his book "Introduction to Scanning Tunneling Microscopy," which I provide here [103].

By making the following assumptions:

1. The tip state is spherically symmetric.

2. The tunneling matrix element does not depend on the energy level.

3. The tip density of states (DOS) is a constant for the energy interval considered.

4. The sample DOS is reasonably smooth as a function of energy.

it is shown that:

$$I \propto \rho_T |\Psi(r_0)|^2 \int_0^{eV} \rho_S(E_F + \epsilon) \, d\epsilon \qquad (2.11)$$

where I is the tunneling current, ρ_T is the tip DOS, $\Psi(r_0)$ is the sample wavefunction at the center of curvature of the tip, ρ_S is the sample density of states, E_F is the Fermi energy. By differentiating each side, it is shown that the differential conductance at the tunneling voltage is proportial to the sample DOS, i.e.:

$$\left. \frac{dI}{dU} \right|_{U=V} \propto \rho_s(E_F + eV, r_0) \qquad (2.12)$$

Despite the simplicity of the Tersoff-Hamann model, it has correctly described key features including the scattered waves of surface electrons [103].

2.4.2 Applications of Scanning Tunneling Microscopy

The scanning tunneling microscope provides a tool to probe a diverse array of materials including metals, semi-conductors, organics, and even ultrathin oxide surfaces. Intuitively, the mechanism of tunneling can be thought of in terms of band diagrams. A positive bias voltage shifts the Fermi energy of the tip to a higher energy (see Fig. 2.21 (a)). Tunneling of electrons then occurs from the occupied states of the tip to the unoccupied states in the metal surface. For a negative applied voltage, Fig. 2.21(b) electrons tunnel from the occupied states of the sample to the unoccupied states of the tip. The shift in bias voltage corresponds to eV in Equation 2.11, and the rate of electron tunneling is I in that equation. The same concept holds for the addition of an ultrathin organic or semi-conductor layer, with the exception that the density of states of the sample is now modified by the density of states of the organic or semi-conducting adsorbates.
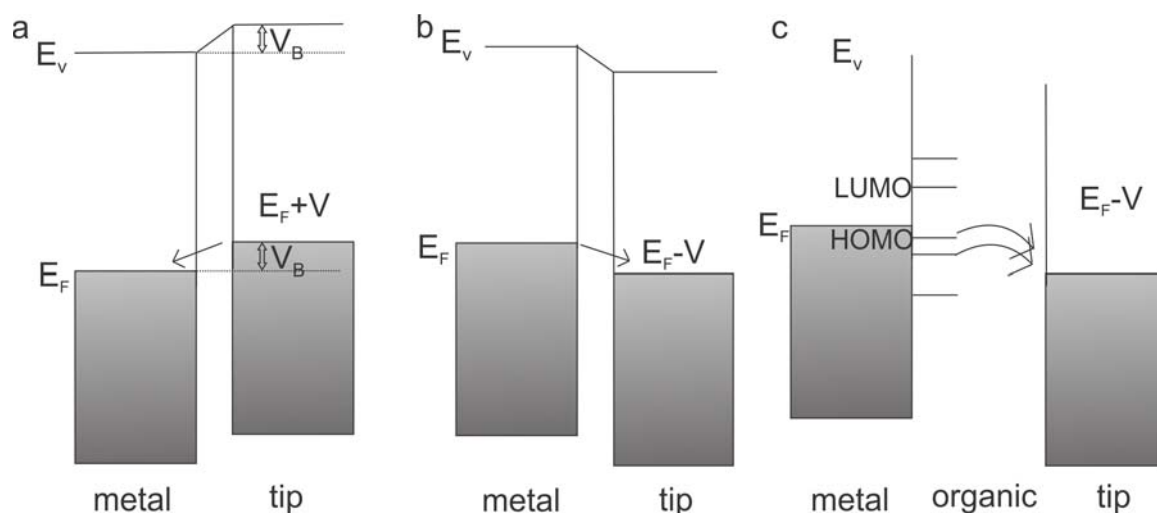
Figure 2.21: Band diagrams to illustrate STM tunneling mechanism. (a) When a positive voltage is applied to the tip, electrons tunnel from the tip into the unoccupied states of the surface. (b) For a negative voltage, electrons tunnel from the metal into the unoccupied states of the tip. (c) In the case of an ultrathin adsorbed organic (or semi-conductor), at negative tip voltages, electrons tunnel from the occupied molecular orbitals of the organic layer into the tip, and at positive voltages electrons tunnel from the tip into the unoccupied orbitals of the organic layer.

STM can also be utilized to examine oxide surfaces. While oxides have a large band gap and possess resistances that can be larger than the tunnel junction resistance, there are a number of cases in which STM can be used. Ultrathin oxide layers of <1 nm thickness are thin enough that metal wavefunctions can protrude through the oxide surface and overlap with the tip. These surfaces can be probed at low bias voltage [104]. For thicker oxide lms, tunneling at a high voltage above the band gap allows for tunneling into the oxide s conduction band [105]. The electric eld from an STM tip can manipulate the electric polarization of thin ferroelectric oxide lms [106]. For a full discussion, see reference [106].

The power of STM is in its ability to spectroscopically probe the DOS of the sample locally. Di erential conductance, or dI/dV spectra allows for the direct measurement of the density of states of a material, because the DOS is directly proportional to the

di erential conductance as was described in the Terso -Hamann model, Equation 2.12. These measurements may be performed in two ways: as point spectra or as dI/dV maps. In both modes the tip bias is modulated by a small AC voltage, on the order of 10 meV peak-to-peak amplitude. For point spectra, the tip is held at a point on the sample and the voltage is ramped through the desired range while the change in tunneling current is measured. This produces a dI/dV spectra, such as that shown in Fig. 2.22 (a), which directly corresponds to the DOS at the point of the tip. To record a dI/dV map, the tip is held at a constant bias voltage to which an AC voltage is added. The tip is then scanned over the surface. This results in a spatial map of a particular electronic feature in the DOS. A sample z image and corresponding dI/dV map of croconic acid is displayed in Fig. 2.22 (b,c) respectively as an example to illustrate these measurement methods. An additional method to measure the DOS has recently been reported by the Dougherty group, in which it is shown that the DOS is proportional to dz/dV spectra [107]. This method accurately preserves the positions and widths of the DOS peaks, often within 0.1 eV [107].
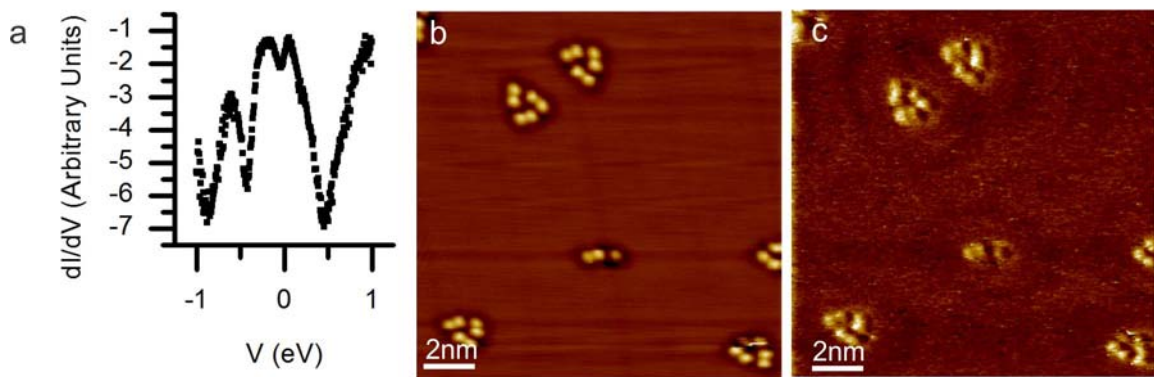

Figure 2.22: (a) Sample dI/dV point spectra taken on a quinonoid zwitterion on Ag(111). (b) STM image and (c) dI/dV map of croconic acid on Ag(111) taken concurrently. The dI/dV map represents the DOS at the scanning voltage.

Other spectroscopic measurements are possible with an STM as well. The $\frac{d^2 I}{d^2 V}$

signal is proportional to losses or gains of energy of the tunneling electrons as the result of inelastic vibrational modes [108]. This effect can be measured with an STM through inelastic tunneling spectroscopy, or IETS, in which vibrational modes of molecules on a surface are measured by taking the $\frac{d^2I}{d^2V}$ spectra in analogy to dI/dV spectra.

Another possibility is to study the workfunction with STM. The tunneling current varies with tip-sample distance, which can be approximated by:

$$I \propto e^{-2kz} \tag{2.13}$$

where z is the tip-sample separation and k is given by:

$$k = \sqrt{\frac{2m(\Phi)}{\hbar^2}} \tag{2.14}$$

where m is the mass of an electron, Φ is the work function of the surface [109,110]. By taking the natural log of the tunneling current and differentiating with respect to z, it can be shown that [27],

$$\frac{\partial ln(I)}{\partial(z)} = -2\frac{\sqrt{2m}}{\hbar}\Phi^{-\frac{1}{2}} \tag{2.15}$$

Therefore, the workfunction of a sample can be determined from measurements of I vs z spectra. This has been demonstrated for organics on metal surfaces [43, 91].

Scanning tunneling microscopy also allows for the measurement of magnetic states of a material by exploiting the tunnel magnetoresistance effect, through use of a ferromagnetic tip. Parallel alignment of the magnetization of a sample and the tip results in a lower tunneling resistance compared to anti-parallel alignment. The tunneling current depends on both the relative alignment of the magnetization of the tip and

sample, as well as the degree of spin polarization of the electronic states of both the tip and sample [103, 111]. Cr(100) is an anti-ferromagnetic material in which neighboring monatomic steps display alternating magnetization alignment. This is illustrated in Fig. 2.23, where (a) shows a constant current mode z-image, and (b) shows the corresponding dI/dV map. In this dI/dV map neighboring steps have alternating contrast due to the magetoresistance e ect. As explained in reference [112], there is a contrast inversion compared to the spectroscopic dI/dV measurements, because in dI/dV maps the tip approaches closer to anti-parallel aligned steps due to the increase in tunneling resistance.
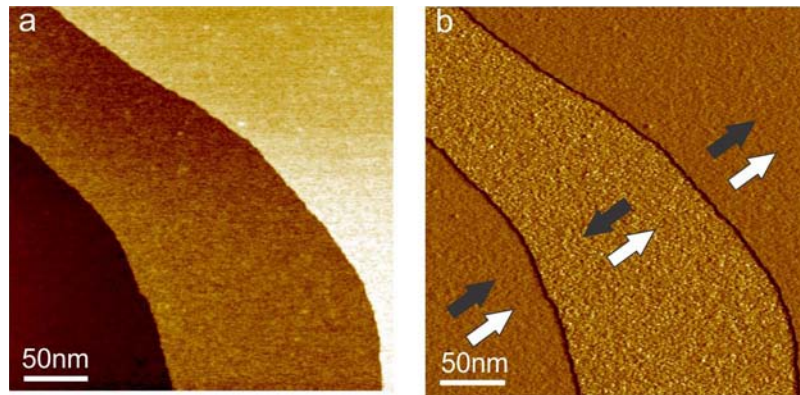
Figure 2.23: (a) STM z-image and (b) Di erential conductance map of a Cr(001) surface imaged with a Cr tip. Black arrows indicate direction of ferromagnetic domains and white arrows indicate magnetic orientation of tip. Note that spin contrast can be detected in the dI/dV image. Tunneling paramters: 0.01 V, 1 nA.

Scanning tunneling microscopy is not limited to measuring metals, semi-conductors and oxides as was described above. In addition to those, superconductive materials can be probed through spectroscopic measurements [113]. Furthermore, charge density waves can be directly imaged with an STM [114, 115]. STM has provided the tool for not just imaging but also manipulating atoms [116]. Using an STM tip, it is also possible to drive and control complex chemical reactions [117].

2.4.3 Experimental Apparatus

An Omicron Low-Temperature STM (LT-STM) was used for all STM measurements in this thesis. The experimental apparatus consists of two connected chambers, one that is used for sample preparation and one that is used for STM measurements. The chamber in which STM measurements were performed had a base pressure of $\leq 5 \times 10^{-10}$ Torr. Electrochemically etched W tips were used for all images. All STM data were taken at liquid nitrogen temperature.

Single metal crystals were prepared by repeated cycles of sputtering with Ar+ ions. Following sputtering, the crystals were annealed to approximately $600\,°C$ by electron bombardment heating. The temperature was measured using an Ircon Ultimax infrared thermometer. All organic molecules discussed in this thesis were deposited through molecular beam epitaxy. Molecules in powder form were placed in quartz crucibles in a home-built Knudsen cell evaporator the details of which are provided in reference [27]. Under vacuum, they were slowly heated until impurities, such as water, were removed. Subsequently molecules were heated to their evaporation temperature and deposited directly onto a sample held at room temperature. A quadrupole mass spectrometer, model RGA 300, was used to monitor residual gas composition and molecular evaporation.

Chapter 3

Investigation of Strongly Dipolar Organic Molecules on Surfaces

Dipolar interactions were studied by examining surface supported organics with large dipole moments. The molecules in question ought to be compact to limit the effect of steric interactions on self-assembly. A recently discovered class of molecule, called quinonoid zwitterions (QZI), was selected for this purpose. This chapter will first provide a review of experimental and theoretical work on QZI. Then STM studies analyzing both the intermolecular and surface interactions are presented for QZI on noble metal surfaces. Finally, results from computational analysis will be discussed.

3.1   Overview of Quinonoid Zwitterions

Quinonoid zwitterions (QZI) are a recently discovered class of organic molecules with a few key defining features: they have a unique 12 π electron system, the zwitterionic state is the ground state, and consequently they possess a very large dipole moment of about 10 D [118]. Each of these characteristics will be disscussed here

in more detail. It is worthwhile to review the concepts of aromaticity and anti-aromaticity before discussing the electron system further. According to the Huckel rule, a planar monocyclic compound with delocalized 4n+2 (n=1,2,3...) electrons is aromatic. However, the de nition of aromaticity is still under debate and there are many competing de nitions, including ones dependent on structure, stability, energy, and magnetism [119]. It is worth noting that many compounds meet only certain criterion but not others. Antiaromaticity was traditionally de ned as systems which have 4n conjugated electrons [120]. For the purposes of this thesis, the de nition based on energy is the most instructive. Fig. 3.1 (a) demonstrates that delocalization results in a decease in energy for aromatic compounds and in (b) an increase in energy for anti-aromatic compounds.
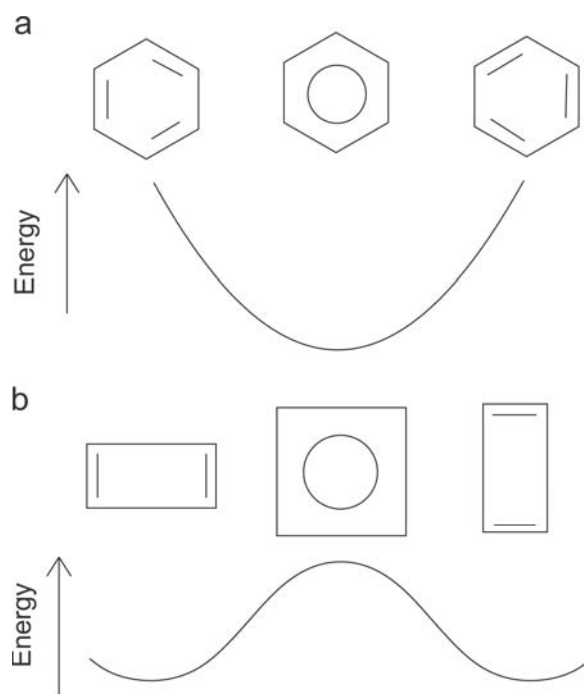

Figure 3.1: (a) Resonant structures of benzene showing that aromaticity lowers the energy compared to the resonant structures. (b) Resonant structures for cyclobutadiene, demonstrating the increase in energy that accompanies delocalization.

Quinonoid zwitterions have a 12 electron system, which based on the number

of π electrons (4n), suggests antiaromaticity. However, the π electrons divide into two, 6-membered subgroups which are fully conjugated and separated by a σ bond. A schematic of QZI, as well as the resonance structures, are shown in Fig. 3.2. Two other examples of organics with 4n π electrons subdividing into two conjugated, but electrically separated groups, with a zwitterionic ground state have been reported [121, 122].
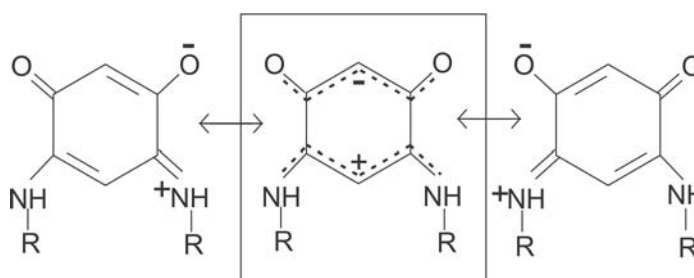
Figure 3.2: The structure of quinonoid zwitterions, highlighted with a box. Note that the two delocalized π electron subunits are not connected electrically. The resonant structures make clear the origin of the positive and negative charges.

A zwitterion is defined as a molecule which has formal unit electrical charge on non-adjacent atoms, with amino acids being the most common example. Note that the QZI shown in Fig. 3.2 has a formal positive and negative charge on the amine and oxygen ends respectively. Thus, the QZI is, in fact, a zwitterion. The localization of positive and negative charges, separated a distance, is what creates the large, 10 D dipole moment of QZI. As was discussed in Chapter 2, this is among the largest dipole moments reported for organic molecules.

Theoretical studies have confirmed the electronic structure initially proposed by Siri and Braunstein, and found the negative charge on the O end of the molecule to be approximately half an electron [123]. Calculations have revealed the potentially antiaromatic nature of QZI through finding a delocalized LUMO which, if filled with a single electron, is sufficient to break the separation of the two 6π subunits [118].

Quinonoid zwitterions (QZI) can be synthesized with a wide range of substituents, thereby allowing for the precise control of chemical, physical, and electrical properties of the end groups and the whole molecule [124]. Numerous QZI and their derivatives have been crystallized. In general, the molecules form hydrogen bonds with two neighbors such that neighboring molecules point in opposite directions, forming 1D chains. The composition of the R-substituent directs more subtle aspects of crystal growth. Methyl QZI, Fig. 3.3(a), form chains which are co-planar whereas tert-butyl QZI, Fig. 3.3(b), form chains which have an accordian shape [125]. However, a bulkier substituent does not always predict non-planar growth. For example, with $R=CH_2CH_2OH$, a co-planar head to tail arrangement is found [126]. Reactions of QZI with metal atoms have even lead to the synthesis of metal-organic crystals containing Ni [127], Pd [118, 128], and Zn [126].

Recently, researchers have begun to examine how QZI interact with surfaces, including Au, lithium niobate, graphene, and HOPG. These will all be discussed in turn. When deposited from solution, butyl QZI attach perpendicularly to Au surfaces through the N groups, as was determined by angle dependent photoemision [129]. When examined with an AFM, pinhole free islands are observed, covering over 98% of the surface [124]. Similarly, QZI with S containing end groups bind perpendicularly to Au directly through the S atom [124]. Interestingly, interactions of butyl QZI with a Au substrate result in the formation a metal induced gap state within the HOMO-LUMO gap [129]. In general, for a range of substituents, Au acts as an electron donor for QZI, and specifically benzyl substituted QZI are found to have molecular orbitals that overlap with the Fermi level of Au, indicating high mobility and semi-conductor or even semi-metal like properties [124]. In a more applied study on Au, thin films of QZI selectively adsorb only one isomer of di-iodobenze through a lock and key mechanism, opening up the possibility of their use as isomeric filters [130].
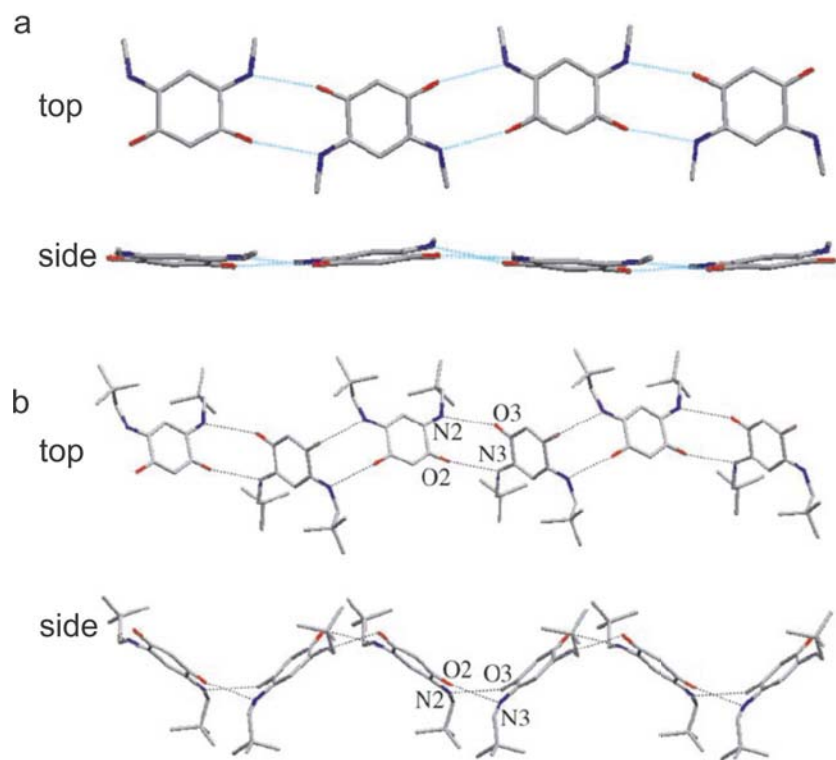
Figure 3.3: The crystal structure of methyl QZI (a) and tert-butyl QZI (b). Crystals are composed of head-to-tail hydrogen bonded chains. Figure adapted from reference [125].

QZI have also been studied on non-metal surfaces. They were found to selectively adsorb on only one domain of ferroelectrically poled lithium niobate [129]. QZI were used as a probe to test the screening capabilities of graphene compared with traditional metals [131]. On HOPG, Fang *et al.* reported the first scanning tunneling microscopy study of QZI, in which the molecules were modified with 18 C long alkane substituents bonded to the amine groups [68]. This influenced their growth into long hydrogen bonded chains parallel to the HOPG surface, which is very similar to the crystalline packing described above.

A systematic study of how a single QZI interacts with a metal surface is still missing from the literature. Likewise, there are no studies pertaining to QZI on
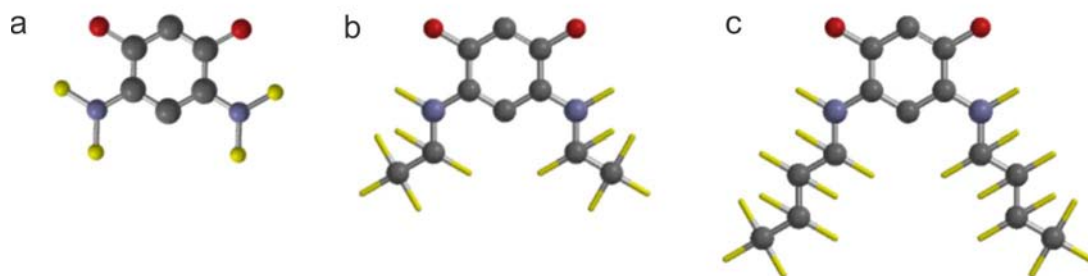
Figure 3.4: The three molecules presented in the study which are (a) parent quinonoid zwitterions, (b) ethyl quinonoid zwitterions, and (c) butyl quinonoid zwitterions.

surfaces performed under UHV conditions, for which the fundamental metal/organic and organic/organic interactions can be more readily determined without convoluting factors such as atmospheric gases and solvent interactions. Thus, presented here are studies of three types of QZI, with R=H, ethyl, and butyl (shown in Fig. 3.4) on three noble metal, single crystal surfaces performed under UHV which will yield unprecedented spatial resolution and a more fundamental understanding of how QZI interact with metal surfaces. These experimental results provide a prototypical model system to study 2D dipole-dipole interactions.

3.2 Experimental Observations of Quinonoid Zwitterions on Metal Surfaces

The three quinonoid zwitterions (R=H, ethyl, and butyl) shown in Fig. 3.4 were studied by STM on the (111) surfaces of Au, Ag, and Cu. An overview over all QZI/substrate combinations studied is shown in Fig. 3.5. QZI form 1D or 2D structures that are of single molecule height on all surfaces studied. From the measured dimensions of each molecule, it is clear that they adsorb with the C ring approximately

parallel to each surface.
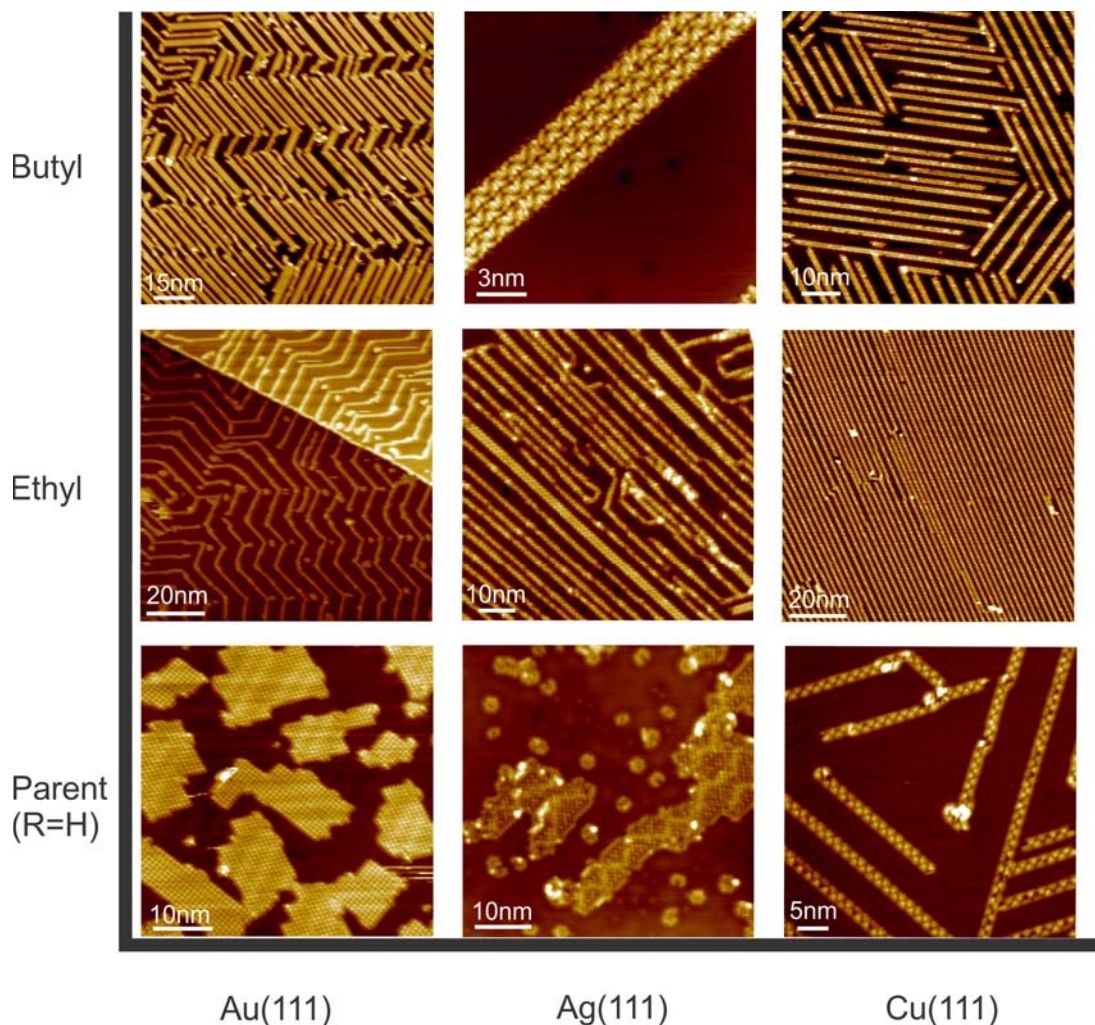
Figure 3.5: An overview of STM studies of quinonoid zwitterions on the(111) faces of Au, Ag, and Cu. Note that two dimensional growth is inhibited for longer substituents.

3.2.1   Parent Quinonoid Zwitterions

First, experimental observations of the parent quinonoid zwitterion (PZI) on Cu(111) will be discussed, followed by Au(111) and Ag(111). PZI form 1D chains *on the Cu(111) surface*, in which each molecule hydrogen bonds to two neighboring molecules,

a model of which is illustrated in Fig. 3.6(e). The alignment of the molecules alternates 180° along a chain. This is very similar to the crystalline structure of many QZI, as discussed in Section 3.1. The spacing between two molecules facing the same direction in a chain is 1.62 nm ± 0.04 nm.

At low coverages (Fig. 3.6(a)) it is observed that no two chains ever grow directly next to one another. Statistical chain arrangement would sometimes result in double and triple chains, but this is never observed. Hence, it is concluded that the chains interact repulsively at low coverage. At high coverage double and triple chains were routinely observed. Representative high coverage STM images are shown in Figure 3.6 (b,c,d). From high resolution images of the chains, as in (c) and (d), the shape of a molecule, and thus its orientation can be determined. Neighboring chains align with an angle of 78° ± 5° with respect to the chain direction, shown as α in Fig. 3.6. The shift occurs with two different orientations, i.e. bonding to the left or right, both of which are commonly observed, seen in (c) and (d). By drawing a model and placing molecules at the observed geometry, as is shown in Fig. 3.6(e), the NH_2 groups are very near each other. These groups are not typically observed to bond in chemistry. One possible explanation is that a chemical modification, such as deprotonation is occuring. This would allow for an additional hydrogen bond between the N atoms. The possibility of deprotonation of PZI is further discussed in Section 3.4.
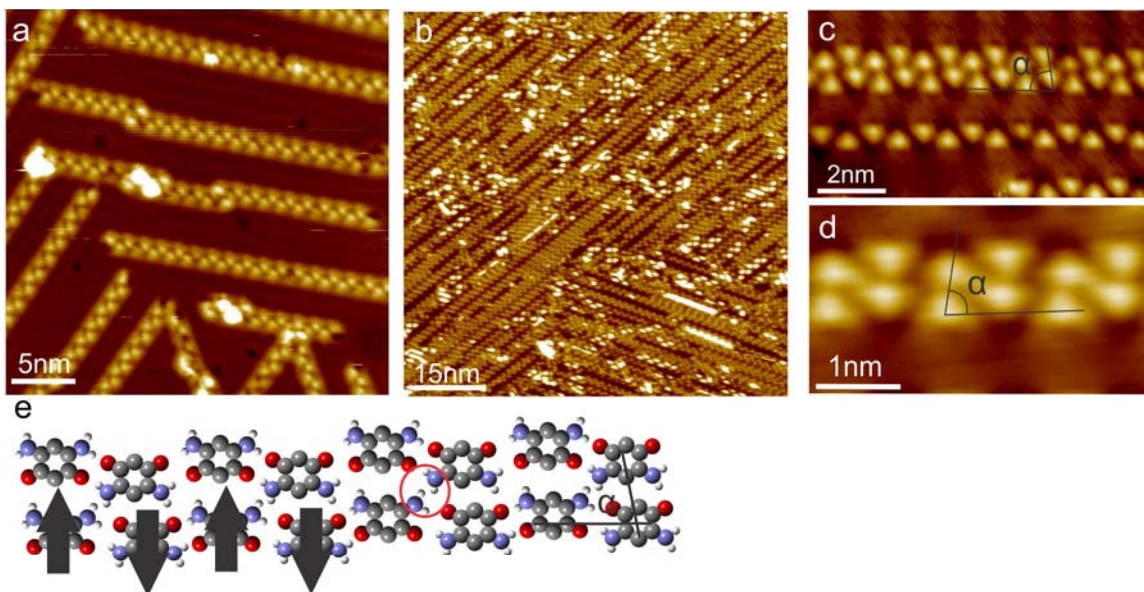
Figure 3.6: (a) STM image of parent quinonoid zwitterions (PZI) on Cu(111) at low coverage. Tunneling parameters: 0.3 V, 850 pA (b) PZI on Cu(111) at high coverage, deposited at room temperature. is measured to be 78   5 from averaging over many images. 0.75 V, 600 pA (c) High resolution STM image, with triangle tip corresponding to O end of molecule. -0.2 V, 600 pA (d) other orientation of PZI on Cu(111). -0.75 V, 600 pA. (e) Illustration of PZI as observed on Cu(111) at high coverage. Black arrows indicate direction of dipole moment and red circle highlights the close distance of neighboring NH_2 groups.

In stark contrast to the observed self-assembly on Cu(111), the parent zwitterions form two-dimensional islands *on Au(111)*, see Fig.3.7. Au(111) exhibits a well-known herringbone reconstruction [132, 133], and island nucleation occurs preferentially at the kink sites of the herringbone reconstruction, which is clearly visible in the STM images in Fig. 3.7. The reconstruction does not impede island growth with increasing coverage. At a coverage below 0.1 ML few islands containing approximately 50   200 molecules are visible, see Fig. 3.7(a). The observation of a low frequency of occurrence of nucleation events relates to a large mean free path for the adsorbed zwitterions, which also implies low di usion barriers. As the adlayer coverage increases, the islands

grow in size, extending easily over many herringbone reconstruction ridges.

The structural model shown in Fig. 3.7(c) results from a close inspection of the alignment of the molecular rows in the networks, the orientation of those rows with respect to the reconstruction ridges as well as the ⟨1̄10⟩ directions of the Au surface, and the details of the geometry at the structural domain boundaries. It is concluded from this model that (i) rows of molecules align with the in–plane ⟨1̄01⟩ directions of the Au, (ii) the symmetry axis of the molecules is aligned parallel to the reconstruction ridges, which explains the observed tilt of the islands in Fig. 3.7(b), and (iii) that the symmetry axes of the molecules makes an angle of 30° with the ⟨01̄1⟩ directions of the Au surface by following the herringbone ridges, which are known to make such an angle with the densely packed directions of the surface [132, 133].

Boundaries between the resulting structural domains are frequently observed, such as the one highlighted by a dashed line in Fig. 3.8(a) for PZI growth on Au. The boundaries can be easily constructed by assuming two structural domains, aligned in opposite directions with respect to each other. Pairs of molecules, at the boundary, form double hydrogen bonds. This would tend to stabilize the domain boundary, and is also consistant with the observed 1D bonding described previously for PZI on Cu(111) as well as that for QZI on HOPG [68]. Two orientations of the molecules are possible for a given domain direction. However, note that the angle between the domain boundary and neighboring molecules across a domain (α in Fig. 3.8) allows us to distinguish between these cases. For the example in Fig. 3.8, by analyzing the angles, it is determined that the molecules are oriented as is shown in (c).

The inter-molecular spacings were measured with sub-angstrom precision and averaged over many molecules, to identify the exact adsorption sites on the Au(111) surface. The molecular spacing along a ⟨1̄01⟩ directions of the Au is within the range of 1.08 nm and 1.11 nm. This spacing would be commensurate with the lattice spac-
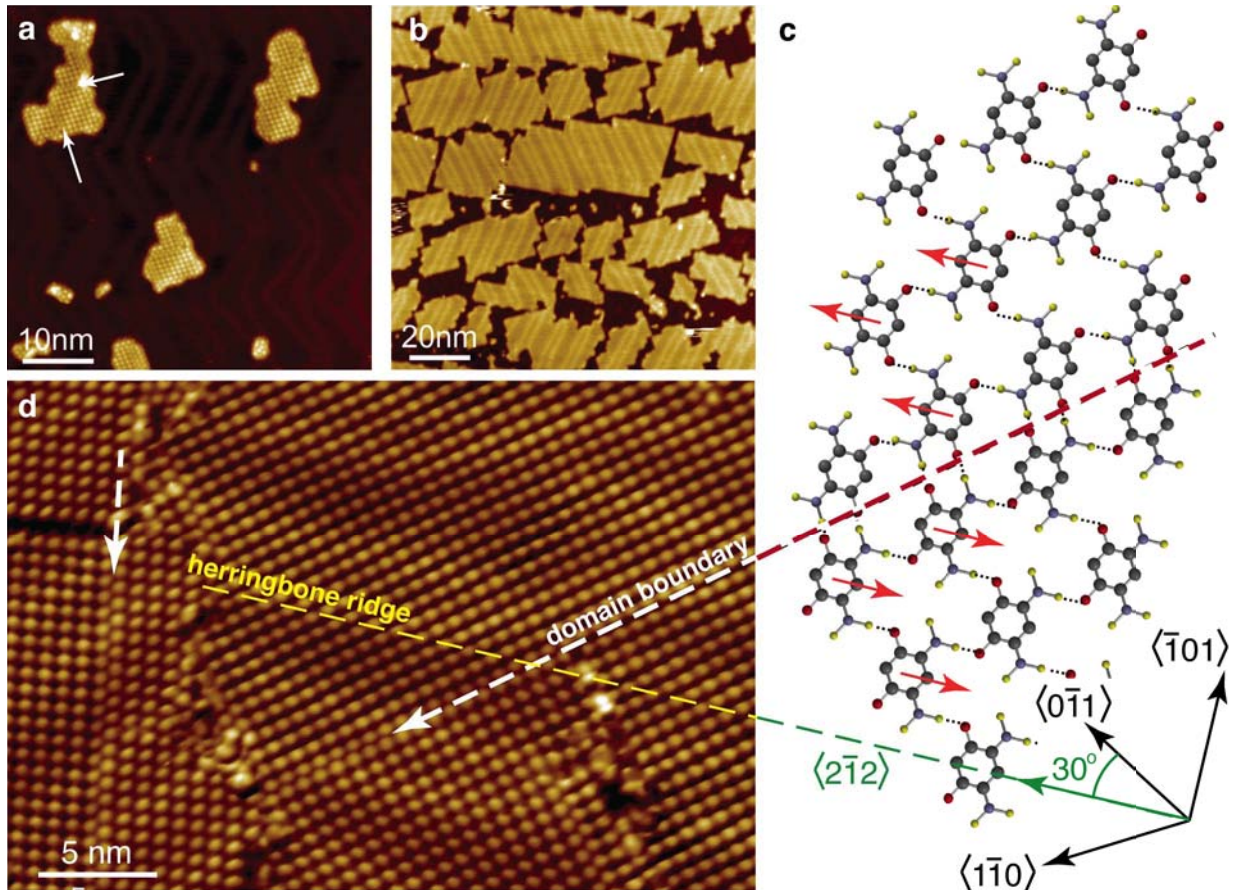
Figure 3.7: (a) Low coverage STM image of PZI on Au(111). White arrows indicate domain boundaries. Tunneling parameters: 0.3 V, 750 pA (b) STM topography image of quinonoid zwitterions on Au(111). Tunneling parameters: 0.3 V, 750 pA. (c) Higher magni cation STM topography, imaged at 0.3 V, 250 pA. The dashed line highlights a structural domain boundary. (d) Proposed structure model of zwitterions on Au(111), showing two domains of aligned molecules, with the domain boundary along the dashed line. Tunneling parameters: 0.3 V, 900 pA. Reproduced from reference [134]

ing of the Au surface along this densely packed direction, where four atomic distances correspond to 1.15 nm, if a compression of the surface in this direction of 5% is considered. Such a compression along 101 is indeed assumed to be the origin of the surface reconstruction [133]. The same measurements of the molecule spacings in the perpendicular 212 direction shows, however, that here the molecular positions are incommensurate with the Au surface lattice. This means that although the 101
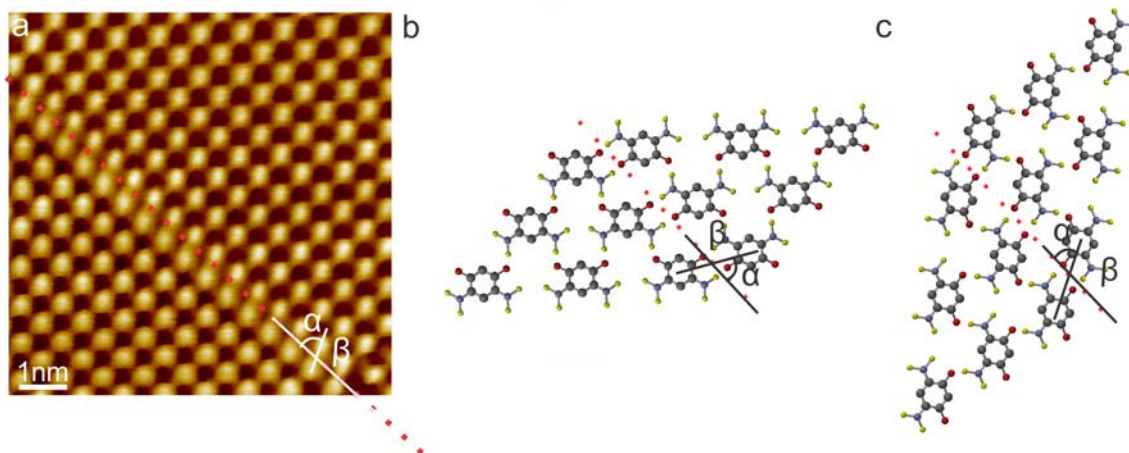
Figure 3.8: (a) STM image of PZI on Au(111) with boundary between two oppositely facing domains highlighted by red dashed line. Note that the angle between neighboring molecules and the domain boundary can be used to determine the orientation of the molecules. From comparing the angle observed in (a) to the two possibilities illustrated in (b) and (c) it is determined that the PZI imaged in (a) are oriented like in (c). Tunneling parameters: 0.3 V, 500 pA

surface directions of the Au surface are a template for the growth of molecular rows, the molecules are not generally locked to specific adsorption sites on the surface. This also implies very small binding energy variations between on-top, bridge and hollow sites for the molecules on the surface.

Next, coverage dependent studies were performed for the PZI on Au. Experimentally, varying the coverage of organics on metal surfaces can result in the formation of different self-assembled structures [135, 136]. Theoretically, higher coverages have also been linked to changes in bonding energy and charge transfer [137, 138]. While the same basic network architecture of PZI was observed for all coverages studied from approximately 0.1 monolayers (ML) to 1 ML, a small change in bond length was observed. Intermolecular bond length was measured at low (0.1 ML) and high (0.8 - 1.0 ML) molecular coverage. For example, Fig. 3.9(a) compares two typical line scans taken over 5 molecules within a low coverage island and a high coverage

lm. Histograms of all measurements taken at both coverages, together with Gaussian

ts, are shown in Fig. 3.9(b). Comparison of both histograms shows unambiguously

that the intermolecular bond length contracts by 0.2 A upon increasing the cover-

age from 0.1 ML to a nearly complete monolayer. The basis of this phenomenon is

disscussed in section 3.3, based on computations. In short, it is due to a weakening

of the surface-PZI bond, with increasing coverage, which allows for stronger PZI-PZI

bonding.
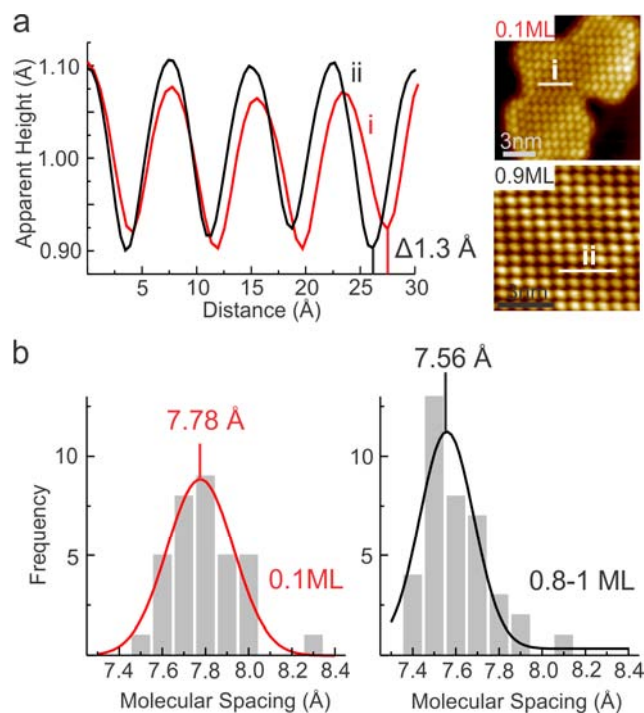
Figure 3.9: (a) STM images and representative line pro les of parent zwitterions taken at low (i) and high (ii) coverages as indicated. (b) Histograms of length measurements taken for low and high coverages, tted with a Gaussian curve. Reproduced from reference [134].

It becomes obvious at higher coverage that the orientation of the islands correlates

with the local direction of the herringbone ridges. Especially, Fig. 3.7(b) and (d)

show the organic network with molecular resolution, together with the herringbone

reconstruction. Atomically resolved STM images of the uncovered Au(111) were also

taken on the same sample to identify the crystallographic 110 directions of the surface and their alignment with respect to the observed molecular rows.

PZI deposited *onto Ag(111)*, shown in Fig. 3.10 (a), exhibit the same bonding as observed on Au(111), and can be explained in terms of a commensurate adlayer structure as follows. The molecular rows are measured to lie 18 5 with respect to the 101 direction, with a spacing of 7.8 A 0.4 A. The molecules all align with the 101 direction cutting the molecule along its high symmetry direction. A model that includes these experimental results is shown in Fig. 3.10 (b). Of importance in these self-assembled structures is the electret nature of each domain, in which the in-plane component of the dipole moment aligns. This is in contrast to our nding for PZI on Cu(111) in which the 1D chains had no dipole moment, but similar to the growth of PZI on Au(111).
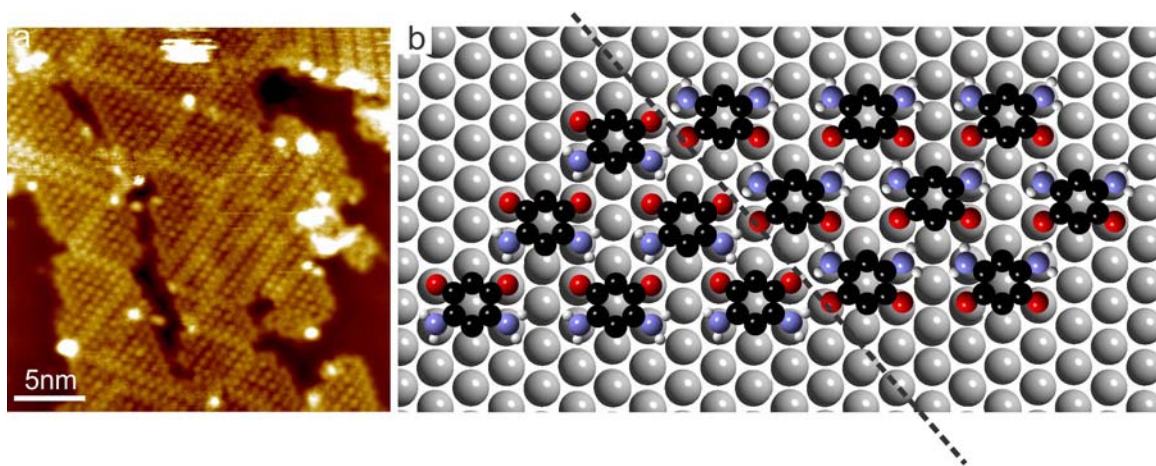
Figure 3.10: (a) STM image of parent quinonoid zwitterions on Ag(111), room temperature growth, tunneling parameters: -0.5 V, 1 nA (b) Model showing commensurate adlayer structure of PZI on Ag(111) with dashed line indicating domain boundary between electrets

A remarkable transformation of island geometry is observed upon annealing PZI on Ag(111) to approximately 84 C and subsequent imaging at liquid nitrogen temperature. The geometry of the islands becomes considerably more complex. Key fea-

tures include double row structures visible as nearly horizontal lines in Fig. 3.11(a). From measuring the bare Ag(111) lattice with atomic resolution, it is found that the columns make an $18° \pm 4°$ angle with the $\langle \bar{1}01 \rangle$ direction of the Ag(111) substrate, with a molecular spacing of 7.6 Å $\pm$ 0.3 Å. Three different rotational domains each with two orientations is observed indicating registry with the underlying Ag(111) substrate.
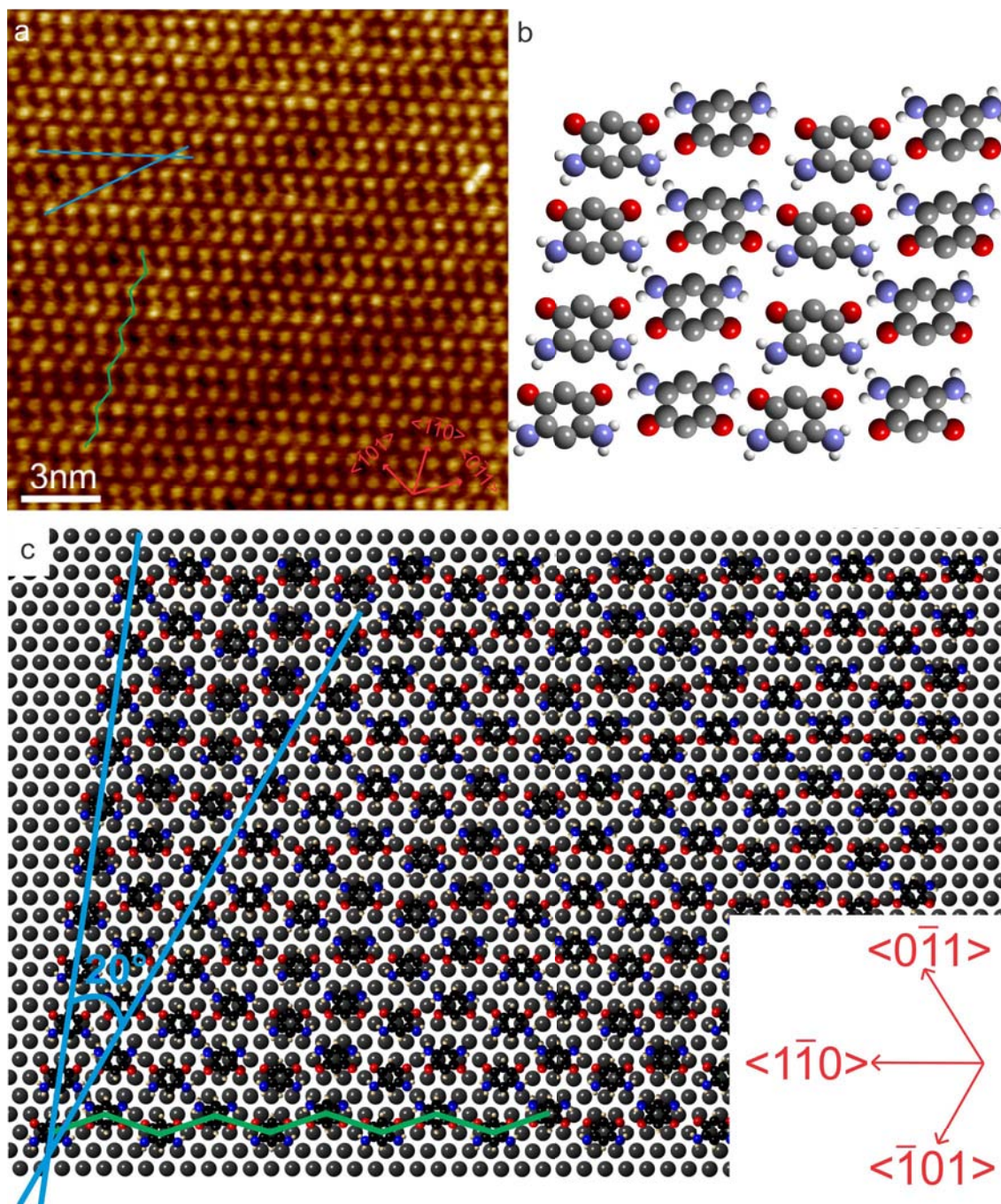
Figure 3.11: (a) STM image of parent quinonoid zwitterions after annealing to approximately 84 C. Tunneling parameters: 0.7 V, 500 pA (b) Model of PZI post annealing. Green line corresponds with H-bonded chain. Blue line highlights stacking of chains 20 to atomic lattice. Bright stripes in STM images correspond to on-top bonding sites in this model and are visible as dark stripes from bottom left to top right of model.

At positive voltages, bright stripes appear at an angle of 13 5 to the 101 direction of the Ag(111) lattice, with an average spacing of 3.6 nm 0.2 nm. The brightness of these stripes is voltage dependent, becoming nearly invisible at negative voltages and positive voltages close to the Fermi level. Typical STM images of these islands as a function of voltage are displayed in Fig. 3.12. These stripes occur at two orientations, to the left or right of the double rows, indicating there are two di erent domains, which are highlighted by green and red lines in Fig. 3.12.
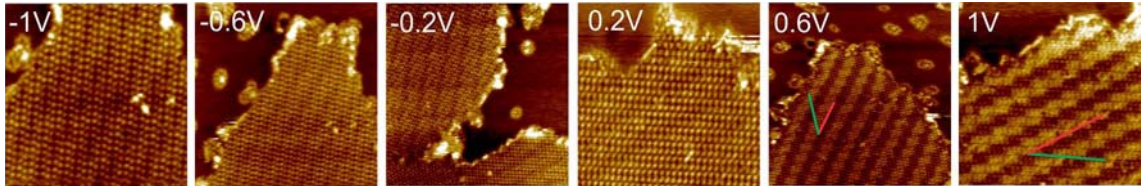
Figure 3.12: STM images of PZI on Ag(111) after annealing to approximately 84 C. Images show how the brightness of stripes depends strongly on voltage. Red lines indicate the direction of the double row structures and green lines highlight the direction of the Moire stripes. Note that two relative orientations of the rows to the stripes are observed.

By constructing a model with the measured dimensions, shown in Fig. 3.11(b) and (c), all key features of these structures are reproduced. The model is based on single H-bonded chains of alternatingly arranged molecules, like those in Fig. 3.6, running parallel to the 110 directions. Neighboring chains form an angle of 20 angle to the 110 direction of the substrate. Along a 110 direction, every sixth molecule sits at the same adsorption site, and perpendicular to that, every 12th molecule has the same adsorption site. As a result of this commensurate epitaxial orientation of the molecular layer with the substrate, a Moire pattern, visible in Fig. 3.11(c) is formed. It is therefore concluded that the origin of the applied contrast in the STM layers is the Moire pattern following from the relative orientation of the commensurate PZI lattice with the Ag(111) surface. This is consistent with previously reported

results [139–142].

To conclude this section, experiments show that PZI form 1D hydrogen bonded chains with no net dipole moment on Cu(111). Whereas on Au(111), PZI self-assemble into 2D domains, in which all the dipole moments align. The results on Ag(111) are somewhere inbetween the Cu(111) and Au(111) results. Namely, PZI form electret domains at room temperature that resemble the structures observed on Au(111), but at higher temperatures PZI form islands with alternating molecules that more closely resemble PZI on Cu(111).

3.2.2   Ethyl and Butyl Quinonoid Zwitterions

From examining Fig. 3.5 one can see that QZI with longer substituent tails (ethyl and butyl) only form 1D chains. This is true for all coverages studied (approximately 0.1 ML to 1 ML) and after moderate annealing to approximately 44°C. From examining the STM images, such as those in Fig. 3.13, it is concluded that the chains are hydrogen bonded with $NH\cdots O$ bonds, as was found for the PZI on Cu(111). In this bonding scheme neighboring dipoles cancel each other, so that each chain has zero net dipole moment.

The molecule-molecule spacing was measured for each the EZI and BZI on all three surfaces (Au(111), Ag(111), and Cu(111)), and values are provided in Table 3.1. A key to the measured lengths is illustrated in Fig. 3.13. The measured intermolecular distances for EZI are the same on all surfaces, within the uncertainty. This is also true for the BZI, confirming that the bonding is, in fact, the same on Au, Ag, and Cu.

The substrate on which EZI and BZI is deposited directs the growth of the chains. On Au(111), both ethyl (EZI) and butyl (BZI) zwitterion chains adsorb between the
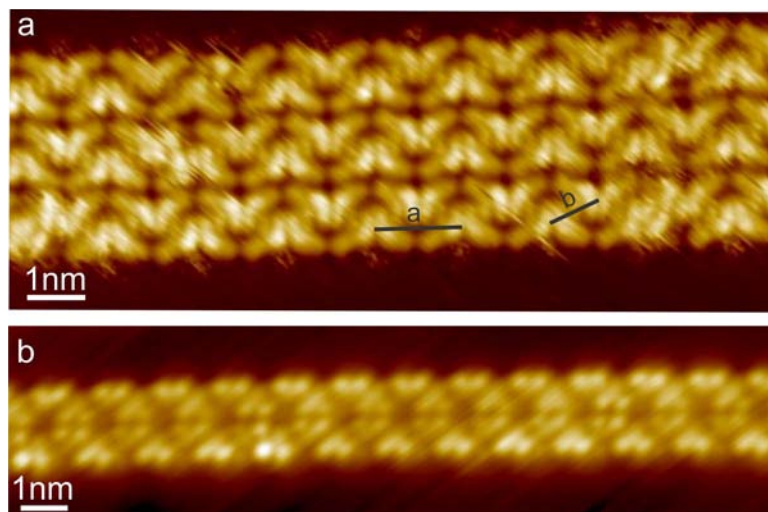
Figure 3.13: STM image of (a) butyl zwitterions and (b) ethyl zwitterions on Ag(111). a and b indicate measured distances as given in Table 3.1

pairs of herringbone ridges at low coverages. Fig. 3.14 illustrates that for the EZI in (a) and (b) and for the BZI in (d). At higher coverages, the molecular chains become longer and do not follow each herringbone kink. This is true for both the EZI shown in Fig. 3.14 (c) and BZI shown in (e).

When deposited on Ag(111), two or even three EZI and BZI chains are often observed directly next to each other, as was shown in Fig. 3.13. This indicates that neighboring chains attract each other through van der Waals forces. Ag(111) lacks a reconstruction, which was what likely prevented neighboring chains from van der Waals bonding on Au(111).

On Cu(111), the 1D rows of EZI and BZI are observed primarily as single chains with bare Cu separating them, shown in Fig. 3.15. The Shockley surface state of Cu(111) is visible in between the zwitterion chains, such as in Fig. 3.15(a). The chains of EZI are long, often appearing over 100 nm in length, Fig. 3.15(b). Whereas the BZI form shorter chains, typically on the order of 50 nm, as in Fig. 3.15(d). At higher coverages double chains are occasionally visible, such as those in Fig. 3.15(c)

Molecule	Surface	Length	Distance(nm)	Uncertainty(nm)
Ethyl ZI	Au(111)	a	1.26	0.09
Ethyl ZI	Au(111)	b	0.72	0.07
Butyl ZI	Au(111)	a	1.36	0.03
Butyl ZI	Au(111)	b	0.72	0.07
Ethyl ZI	Ag(111)	a	1.30	0.05
Ethyl ZI	Ag(111)	b	0.79	0.09
Butyl ZI	Ag(111)	a	1.31	0.10
Butyl ZI	Ag(111)	b	0.74	0.10
Ethyl ZI	Cu(111)	a	1.33	0.02
Ethyl ZI	Cu(111)	b	0.76	0.10
Butyl ZI	Cu(111)	a	1.40	0.05
Butyl ZI	Cu(111)	b	0.82	0.09
PZI	Cu(111)	a	1.62	0.04
PZI	Cu(111)	b	0.77	0.09

Table 3.1: Measured molecule-molecule spacing for ethyl and butyl zwitterions on Au(111), Ag(111), and Cu(111). Parent quinonoid zwitterions on Cu(111) are provided for comparison. See Fig. 3.13 for illustration of distances a and b.

and (e). Note that the zwitterion chains are very regularly spaced. For example, most EZI chains shown in Fig. 3.15 (c) have a chain to chain spacing of either 1.69 nm or 2.11 nm. This seemingly repulsive behavior between chains is best explained by long range Shockley state interactions, which is further discussed in Section 3.3.
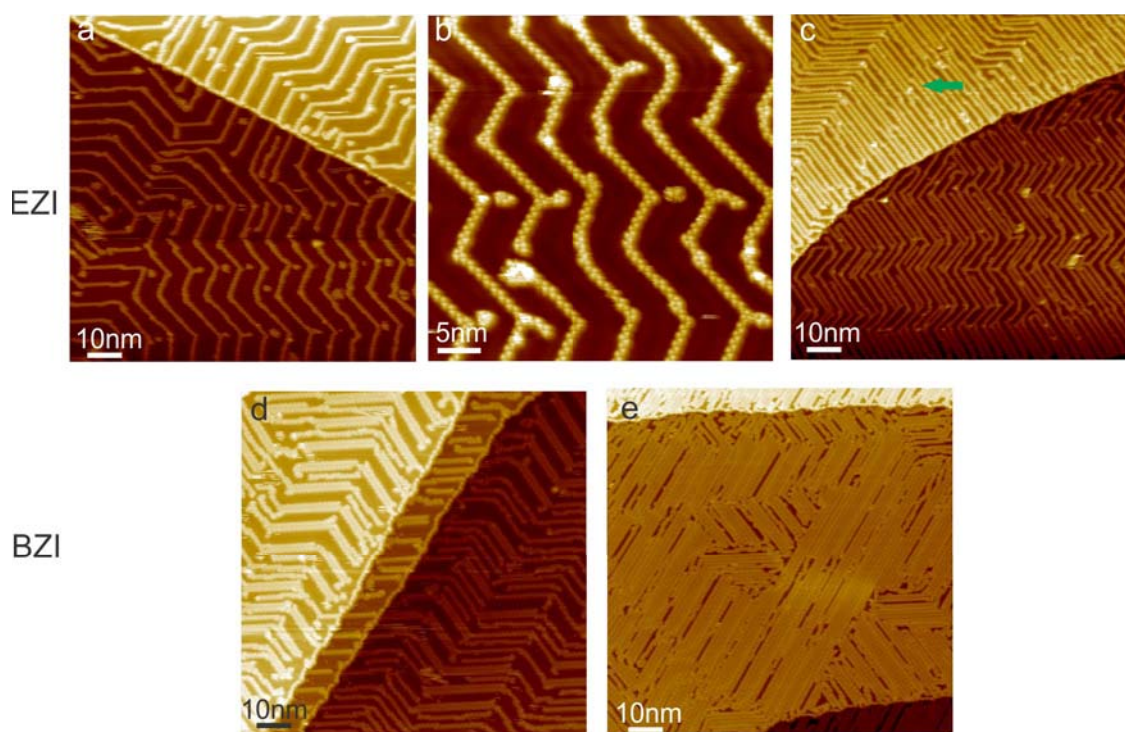
Figure 3.14: STM images of ethyl zwitterions (a-c) and butyl zwitterions (d,e) on Au(111). At low coverages molecules adsorb between pairs of the herringbone ridges, visible between molecular chains in (b). At higher coverages molecular chains straighten and grow over the herringbone reconstruction. The green arrow in (c) highlights this phenomenom. Tunneling parameters: (a) 0.3 V, 300 pA (b) -1 V, 300 pA(c) 0.3 V, 400 pA (d) and (e) -0.7 V, 300 pA.
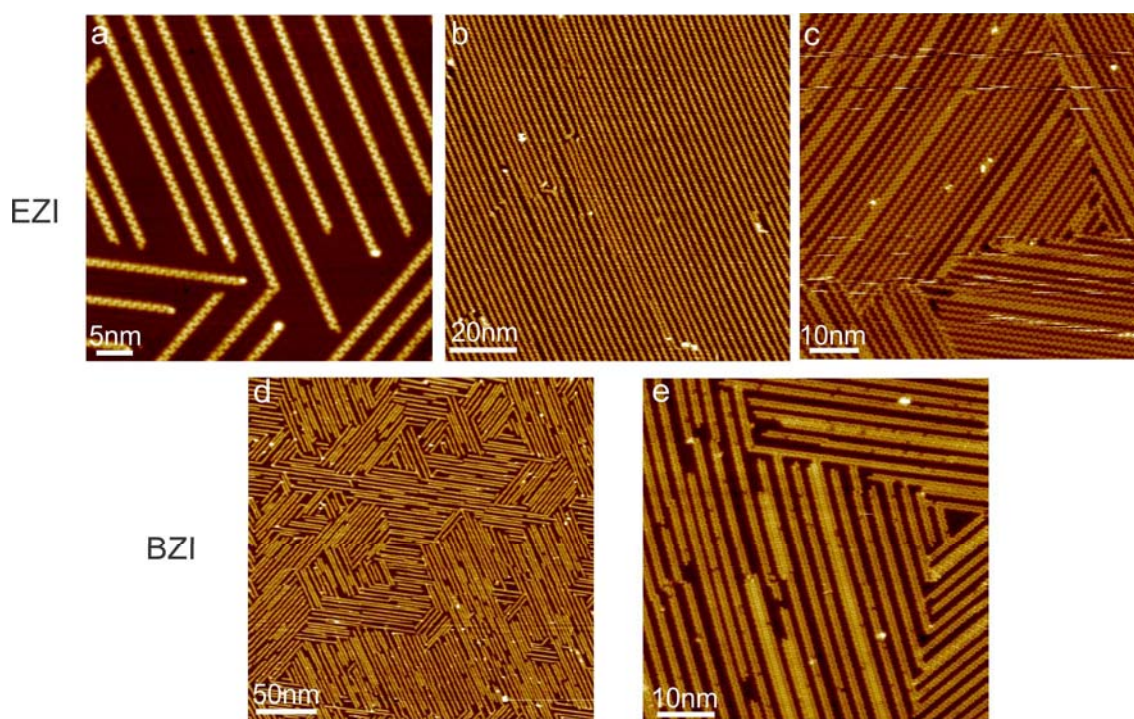
Figure 3.15: STM images of ethyl zwitterions (a-c) and butyl zwitterions (d,e) on Cu(111). Even spacing of EZI and BZI indicates repulsive interaction. At high coverages (c,e) occasionally two chains are close to each other ruling out strong repulsive forces. Tunneling parameters: (a) 0.1 V, 400 pA (b) 0.2 V, 300 pA (c) -0.6 V, 300 pA (d) 0.3 V, 350 pA (e) 0.22 V, 300 pA

3.3 Discussion of Self-Assembly

In the previous sections, experimental observations were documented for the QZI on Au(111), Ag(111), and Cu(111). This section aims to put those observations into perspective with a comparison to the literature, as well as a discussion of theoretical results developed through a collaboration with Dr. Eva Zurek, Dr. James Hooper, and Scott Simpson from the Department of Chemistry at the State Univeristy of New York at Buffalo during the project.

3.3.1 Single Molecule Adsorption Phenomena

All three types of quinonoid zwitterions (R=H, ethyl, and butyl) on all three metal surfaces adsorb with the plane of the C ring nearly parallel to the metal surface. This was determined from analyzing the size of molecules in STM images. If the molecules adsorbed perpendicular to the surface, they would appear much smaller than is observed. This claim is supported by theoretical calculations, which show an approximately flat adsorption geometry on Au(111) and Cu(111) and a 9.8° tilt on Ag(111) with the carboxyl groups slightly closer to the metal surface than the amine groups, as illustrated in Fig. 3.16. See references [47, 134] for computational details. Note that the observed absorption geometry is in contrast to the adorption geometry after deposition from liquid of butyl zwitterions on Au(111) as reported in references [124, 129], in which they bind perpendicular to the surface.

Surface interactions between individual PZI and metal surfaces were analyzed by density function theory calculations, see references [47, 134], and were found to have a strong effect of the dipole moment of PZI as follows. Upon adsorption, the discrete HOMO and LUMO energy levels broaden into bands, as was discussed in Chapter 2, shown schematically in Fig. 3.17. This results in the overlap of each of these bands
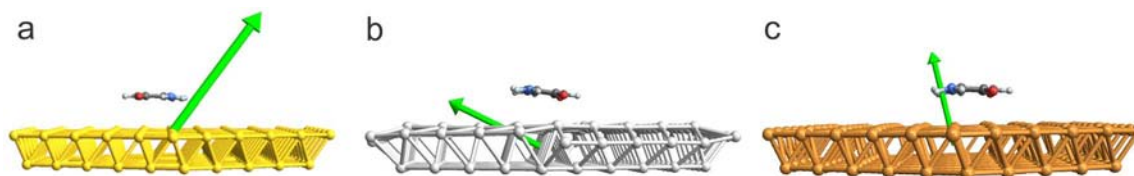
Figure 3.16: Calculated absorption geometries for PZI on (a) Au(111) (b) Ag(111) and (c) Cu(111). Note that they are all nearly parallel to the metal surface. See references [47, 134] for computational details.

with the Fermi level of the metal surface. Hence charge is donated from the HOMO of the molecule into the surface, and back-donated from the surface into the LUMO. This mechanism is fundamentally similar to that of the IDIS model, described in Chapter 2.

As shown in Fig. 3.18, for PZI on Cu, the LUMO is spread over the entire molecule, but the HOMO localized primarily over the carboxyl groups. The frontier orbitals have nearly identical shape on all surfaces studied. As a result, charge is redistributed within the molecule, causing a drastic reduction in the dipole moment, together with a tilt of the dipole of the molecule-surface system out of the plane.

Theoretical results for the dipole moment, net charging, and bond strength to the surface for PZI are summarized in Table 3.2. First note that the bond strength is weakest on Au(111) and strongest on Cu(111), which is typical of these metals [82]. The dipole moment in the plane of the molecule was 10 D before deposition. Charge rearrangement results in approximately a 8.5 D decrease in the dipole moment for all three surfaces studied. As was discussed in Chapter 2, metal surfaces have an intrinsic surface dipole which points inwards. The adsorption a single PZI reverses the direction of this dipole moment, so that it now points out of the plane. This would, in e ect, decrease the workfunction of the metal surface drastically. PZI aquire charge on Au(111) and Ag(111), and donate charge to the Cu(111) surface. However, when
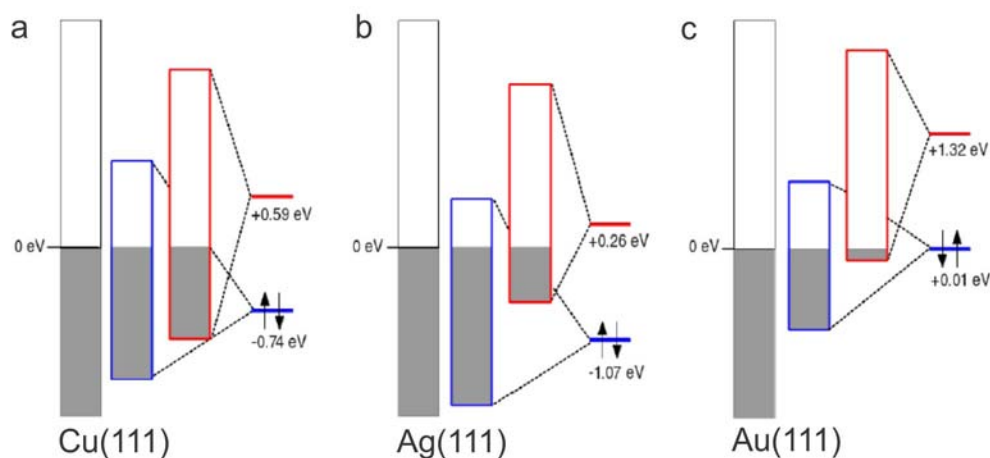
Figure 3.17: Both the HOMO and LUMO of parent quinonoid zwitterions adsorbed onto (a) Cu (b) Ag and (c) Au surfaces broaden upon adsorption. This results in overlap with the Fermi level and subsequent charge rearrangement, causing a drastic reduction of the dipole moment. Figure credit: Scott Simpson and Eva Zurek from the State University of New York at Bu alo.
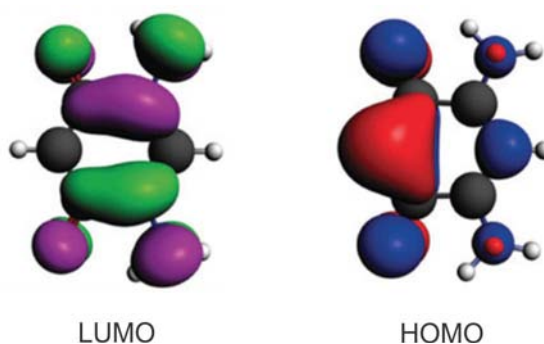
Figure 3.18: Plots of the lowest unoccupied (LUMO) and highest occupied (HOMO) molecular orbital for the parent quinonoid zwitterions. Note that the LUMO is spread over the entire molecule, whereas the HOMO is primarily located on the carboxy group of the PZI. Figure credit: Scott Simpson and Eva Zurek from the State University of New York at Bu alo.

compared to values from the literature of other molecule-metal interfaces, such as those given in Chapter 2, these are relatively small values.

In order to investigate the nature of the charge reorganization upon molecular adsorption to the Au(111) surface in greater detail,the charge density di erence (CDD)

Surface	In-Plane Dip.	Out-Plane Dip.	Mag. Dip.	Charge(e)	BE(eV)
Au(111)	0.89	1.2	1.5	-0.21	0.98
Ag(111)	1.1	1.1	1.6	-0.02	1.54
Cu(111)	0.3	1.3	1.3	0.14	1.91

Table 3.2: Theoretical results for parent zwitterions on noble metal surfaces as reported in references [47, 134]. All dipole moments given in units of Debye. BE is binding strength to the surface.

plots were calculated for the various coverages considered, see reference [134] for details. For low coverages, the CDD plot in Fig. 3.19 illustrates that there is a build–up of charge (red) below the amine containing side of the zwitterion, and a depletion of charge (blue) below the end which contains oxygen, in–line with the results previously obtained for adsorption to Cu(111) and Ag(111) [47]. The CDD plots show that for all three substrates at low coverage the charge transfer induces a surface dipole which opposes the molecular dipole. The Pauli repulsion effect, which was discussed in Chapter 2, dictates that the electron density just above the surface decreases, upon adsorption, as a result of Pauli repulsion. Regions showing both a depletion and an increase in the charge density between the molecule and the surface are evident at low coverage, suggesting that both Pauli repulsion and charge donation from the molecule are important in explaining the charge redistribution that occurs.

In order to investigate the interaction of flat–lying orientations of the zwitterion with the substrate, geometry optimizations were carried out where the center of the molecule was placed over the top (T), bridge (B), or hollow (H) positions of the Au(111) surface, as illustrated in Fig. 3.20. In addition two configurations were considered: one where the axis bisecting the zwitterion (ν) makes an angle (θ) of $0°$ with respect to the x–axis, and another where this angle is $30°$. The bonding energy of the most stable configuration, H30$°$, was calculated as being 0.98 eV. The relative bonding energies with respect to the most stable site, see Fig. 3.3, show that the
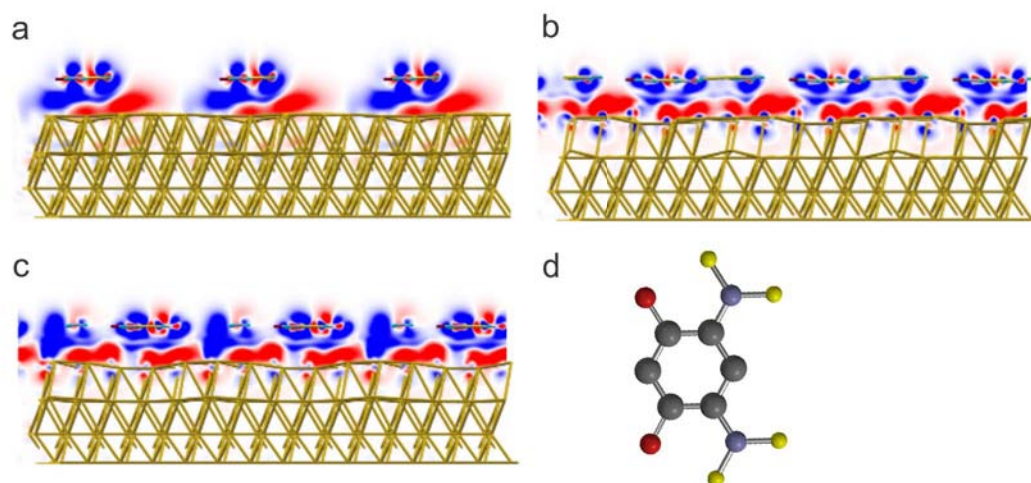
Figure 3.19: The redistribution of charge that occurs upon adsorption of the zwitterion to the Au(111) surface calculated for coverages of (a) 0.32, (b) 0.64 and (c) 0.96 ML. Red indicates a build up, and blue a depletion of charge. (d) Shows the orientation of the PZI from a top view in (a-c). Reproduced from reference [134]

potential energy surface is quite at, with around 0.04 eV corrugation, which is similar to results previously obtained for benzene on various coinage metal surfaces [143,144]. The small di erences in energy imply that the di usion barrier is low. The shortest vertical distance between a carbon atom in the ring and the metal surface was found to be 3.25 A, and the zwitterion remains relatively parallel to the metal surface after optimization. This computational result of only weak corrugation of the potential energy surface is consistent with the experimental observation of a long mean free path of the adsorbed molecules, and an organic adlayer that is incommensurate with the substrate, as was described earlier.
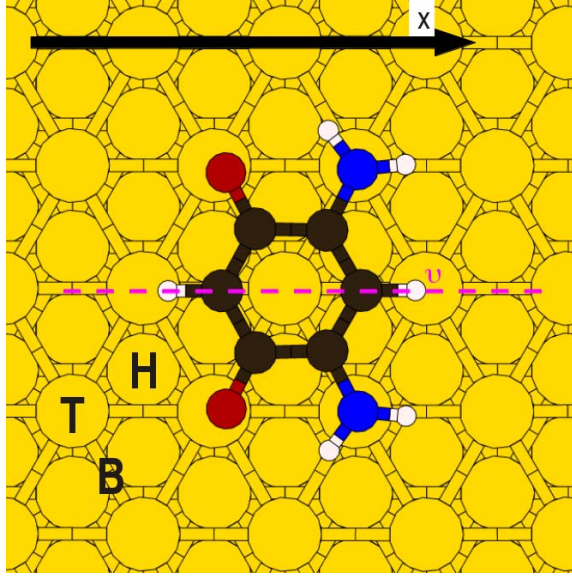
Figure 3.20: The Au(111) surface indicating the top (T), hollow (H), and bridging (B) sites. The axis that bisects the zwitterion, ν, is indicated by the pink dashed line, and the x–axis by the black arrow. In this figure the zwitterion is adsorbed to the T site with $\theta = 0°$. Carbon, nitrogen, oxygen, hydrogen and gold atoms are colored as black, blue, red, white, and yellow, respectively. Reproduced from reference [134].

Site	θ	E_{rel} (eV/molecule)	$d_{\mathrm{PZI\text{-}surf}}$ (Å)
B	0	0.01	3.26
B	30	0.03	3.39
H	0	0.00	3.25
H	30	0.04	3.38
T	0	0.03	3.20
T	30	0.04	3.25

Table 3.3: Adsorption sites, angles (θ) (see Fig. 3.20 for an illustration of the binding sites), and the metal to adsorbate distances ($d_{\mathrm{PZI\text{-}surf}}$) of the quinonoid zwitterion on the Au(111) surface. $d_{\mathrm{ZI\text{-}surf}}$ was taken as the shortest vertical distance between a carbon atom in the zwitterion and a gold atom on the surface.

3.3.2   Coverage Dependent Bond Strength of PZI on Au(111)

Our experimental results in Fig. 3.9 showed a decrease of the intermolecular bond length with increasing molecular coverage. Using DFT theory this contraction can be linked to the interaction between molecules and the surface. These calculations (see reference [134] for computational details) determine the bond energy to the surface and to other PZI as a function of coverage. The results are summarized in Table 3.4. The calculations assumed a uniform distribution of molecules, which is very different from the dense islands separated by large empty space which were observed in the STM experiments. In the theoretical computations, intermolecular bond length was a function of coverage due to the uniform distribution of molecules. In this sense, the high-coverage computational models appear to be a better description of the zwitterionic networks adsorbed on Au(111) at all coverages. As coverage increases in the calculations, less charge is transferred to the PZI and the bond strength of a molecule to the surface decreases, which corresponds with an increased molecule-substrate separation. This coverage dependent charge transfer is understood by examining the molecular orbitals as a function of coverage. As was shown in Fig. 3.17, the HOMO of the PZI broadens significantly upon adsorption to Au(111). The resulting overlap with the Au Fermi level was the primary driver of charge transfer. As coverage increases, the HOMO becomes sharper, which results in less overlap and therefore less charge transfer.

The total bond energy (surface and intermolecular) increases with coverage, since the substantial increase in intermolecular bond strength outweighs the decrease in surface bond strength. This is in constrast to a report of TTF on Au(111) [137] and azoles on Cu(111) [138] in which the magnitude of total energy, due to intermolecular bonds

Coverage (ML)	BE	$BE_{PZI-PZI}$	$BE_{PZI-surf}$	$d_{PZI-surf}$ (Å)
0.96	1.47	0.73	0.74	3.44
0.89	1.04	0.24	0.80	3.34
0.64	1.19	0.42	0.77	3.37
0.50	1.02	0.07	0.96	3.27
0.32	0.98	0.04	0.95	3.25
0.22	1.01	0.02	0.99	3.26
0.16	0.98	0.01	0.97	3.26

Table 3.4: The influence of the surface coverage on the bonding energy (BE), given in eV/molecule. Results are listed for the total energy, the bond energy of PZI to Au(111), the PZI-PZI bond energy, and the metal to adsorbate distance ($d_{ZI-surf}$) of the PZI on the Au(111) surface. For details concerning calculations, see reference [134].

[a] One ML of coverage is defined as 1.73 molecules/nm^2.

as well as surface bonds, decreased with increasing molecular coverage. Fraxedas *et al.* attributed this to increased repulsion between molecular dipole moments as the molecules were closer together at higher coverages. In both reference [137] and in this PZI study, intermolecular interactions become more important relative to surface interactions at higher coverages, however the difference lies in PZI exhibiting attractive behavior whereas TTF exhibits a mixture of attractive and repulsive interactions. Despite the differences in molecular distribution between experiment and theory, the experimental decrease in bond length is seen as a confirmation of the theoretical predicted weakening of the molecule-metal interactions with increasing coverage.

3.3.3 Amine Deprotonation

The experimental results of PZI on Ag(111), Fig. 3.11, and PZI on Cu(111), Fig. 3.6, suggested that the NH$_2$ groups may deprotonate on the surface. This deprotonation shall now be discussed. A number of recent studies have demonstrated the occurance of deprotonation of adsorbed molecules on Ag [145–149], Cu [150–155], and even Au [156]. The energy of activiation for deprotonation depends on both the elemental

composition of the substrate as well as the crystal facet that is exposed, with the (111) facet being the least reactive for Cu, Ag, and Au crystals [157].

If deprotonation is assumed in the experimentally observed networks of PZI on Ag and Cu, a model can be constructed in which the deprotonation serves to stabilize the structures through an additional NH$\cdots$N hydrogen bond. Fig. 3.21 illustrates this model with the additional bond highlighted by a green circle. If one assumes the zwitterions remain intact for either system, neighboring rows would interact through positively charged NH$_2$ groups. This interaction is Coulombicly repulsive, which lends support to the idea of deprotonation. If one assumes the observed structures on Ag and Cu are deprotonated, then deprotonation occurs at room temperature on Cu(111), but annealing is necessary for deprotonation on Ag(111) system. This temperature threshold for deprotonation is in accordance with other molecular systems [145–147,152,153]. Deprotonation also explains the observed angular shift to the left or right of each chain to its neighboring chain. This is because the NH$\cdots$N bonds can only form on one side due to simple geometric considerations, and thus accounts for the experimentally observed symmetry breaking. However, without calculations to support deprotonation, it remains only a possibility.
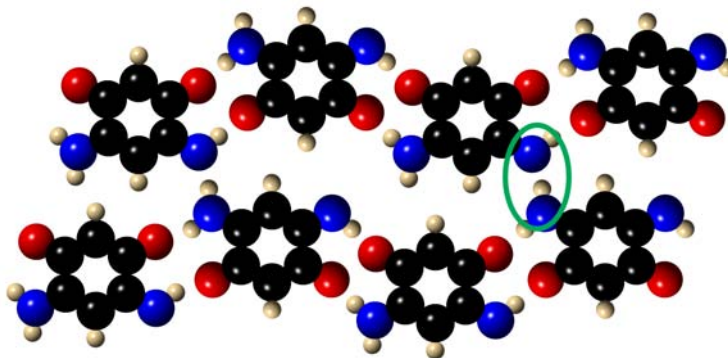
Figure 3.21: Assuming single deprotonation of PZI, an additional NH   N bond, highlighted by a green ellipse, would form stabilizing double chains, as observed on Ag(111) and Cu(111).

3.3.4   Long Range Surface Mediated Interactions

All quinonoid zwitterions form 1D chains on Cu(111) that are separated uniformly, as was demonstrated in Fig. 3.15 and Fig. 3.6(a). This is in stark contrast to the growth on Ag(111) and Au(111), in which chains or molecules attract each other to form 2D islands. There are two possibilities for the repulsive behavior on Cu(111). First, QZI may be aquiring electric charge on the Cu(111) surface, which makes the chains experience Coulombic repulsion. Parent zwitterions were found to aquire a net charge of approximately 0.02 - 0.09 e$^-$ on Au(111) [134], 0.02 e$^-$ on Ag(111) [158] and -0.14 e$^-$ on Cu(111) [158]. While QZI have the highest charge on Cu(111), it is not clear that this is su   cient to cause repulsion between the chains.

A second possibility for the observed repulsive behavior of the QZI chains on Cu(111) is interactions with the Shockley surface state, which consists of electrons that form a nearly-free electron gas. The scattering of such electrons leads to quantum interference patterns in the local density of states and to long-range Friedel-type oscillatory interactions between adsorbates. The energies for these interactions are often on the order of one or more meV [159], which is signi cantly lower than many

relevant energies such as hydrogen bond formation as was discussed in Chapter 2. Thus these long range interactions are likely a secondary driver of the self-assembly. The Shockley state of Ag(111) has been attributed to the formation of similar 1D nanogratings [69]. In this system it was shown that the occasional presence of rows directly next to each other could rule out strong repulsive interactions, such as dipole-dipole repulsion, as the driving force of the observed structures [160].

3.4 Does the Dipole Moment Drive Quinonoid Zwitterion Self-Assembly?

One of the central questions of this thesis, as stated in Chapter 2, is to quantify the role that a dipole moment has in determining the self-assembly of strongly dipolar molecules. Using Equation 2.3 for the experimentally observed structures of PZI, the dipole-dipole energies were calculated. The actual dipole moments of the adsorbed PZI, calculated with DFT and described in the previous section, were used for the calculations. The in-plane component of this dipole moment and the measured experimental geometry was used to estimate the energy of three configurations: molecules all aligned into eletret domains, single alternating chains, and multiple alternating chains. These configurations are illustrated in Fig. 3.22.

Equation 2.3, the Coulombic energy equation, was selected because the bond length is similar to the length of the dipole itself. While this method does not take into account higher order terms such as mirror dipole components, the goal is to rank the structures regarding their electrostatic energies. Note that none of the out of plane components for the dipole moments are included in the simulations. Because these dipole moments are all parallel out of the plane, this component only raises

Energy/Molecule(meV)	Type of Network	Dipole (D)	Substrate
-1	single chain	0.89	Au(111)
-3	multichain	0.89	Au(111)
-2	diamond	0.89	Au(111)
-2	single chain	1.1	Ag(111)
-4	multichain	1.1	Ag(111)
-2	diamond	1.1	Ag(111)
-0.1	single chain	0.3	Cu(111)
-0.5	multichain	0.3	Cu(111)
-0.1	diamond	0.3	Cu(111)

Table 3.5: Dipolar Energies of Adsorbed Parent Quinonoid Zwitterions

the energy of each con guration, as was shown in Chapter 2. Thus the energies presented here can be viewed as a lower limit. The magnitude of the out of plane dipole moments do not vary signi cant for the three systems studied: 1.2 D, 1.1 D, and 1.3 D for Au, Ag and Cu respectively. Therefore the interaction energy of the out of plane components of the dipole moments should be comparable and is thus omitted.
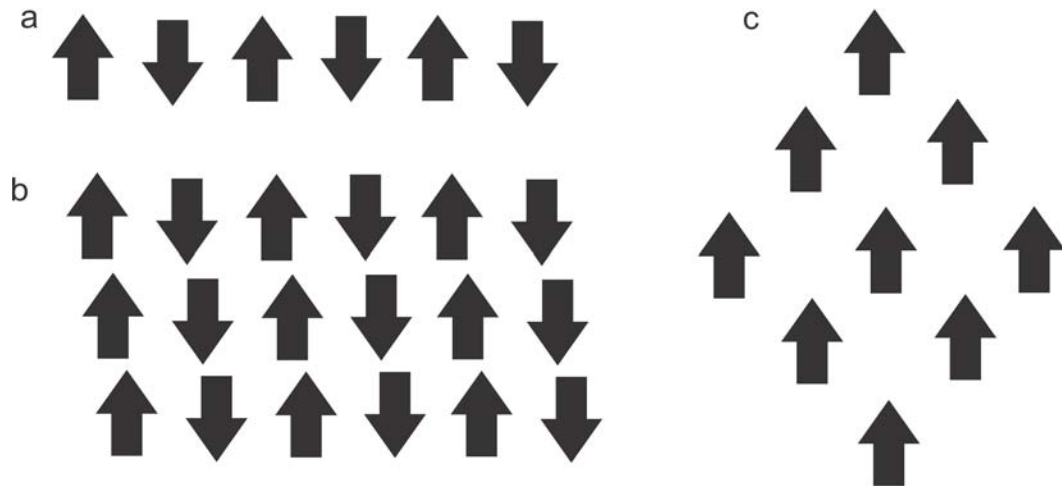

Figure 3.22: Illustrations of dipolar con gurations, for which the energy/molecule was calculated. (a) Single Chain (b) Multichain and (c) Diamond. Note that the calculations were performed for structures containing many molecules (N>100).

Table 3.5 displays dipolar energies of the calculated configurations. Experimentally determined distances were used when available. When not available, a reasonable estimate was used. For example, diamond domains were never observed on Cu, so the same bond distance was assumed as was observed in the chains. The energies vary from -0.1 to -4 meV for the structures analyzed. Comparing the calculated energies to typical energies of H-bonds, 170-650 meV [28] it becomes clear that the dipole energy is not the primary driving factor in self-assembly. For an additional comparison, the difference in bonding site energy for the Au(111) surface was reported to be 40 meV [134], see page 76 for details, which was declared inconsequentially small, yet is still an order of magnitude larger than any of these numbers. As was discussed in Chapter 2, similar calculations have only been reported once, to my knowledge, in the literature. In that case, even with a 100 D dipole moment, the lowest energy was -39 meV/particle which is still significantly less than a hydrogen bond.

It is worth noting that when the surface plays the most limited role, on Au(111), the molecules are relatively free to assemble into the most energetically favored configuration. However, in this case the result is not the structure with the lowest dipole-dipole energy, which would be the multichain, adding further evidence to the point that the dipole moment is not the primary driving force.

Instead the self-assembly is thought to be the result of several competing mechanisms. Hydrogen bonding, which is seen in all quinonoid zwitterion systems studied, is highly important with intermolecular bonding energies above 700 meV for certain cases. Secondary effects that determine the observed structures include site selective dependence, which is on the order of 40 meV for PZI on Au(111), and is possibly higher in other cases. Both attractive and repuslive dipolar forces compete with much smaller energies of <5 meV. It is this complex interplay of forces that when combined, determine network stability and also the relative molecular alignments.

Chapter 4

2D Single Component, Organic Hydrogen Bonded Networks

Hydrogen bonds play a foundational role in the natural world, from holding DNA in a double helix shape to giving water many of its properties. In crystal design, hydrogen bonds are particularly important because of their directional nature, allowing for the rational design of crystals, both in 2D and 3D. Furthermore, the recent discovery of ferroelectricity through switchable hydrogen bonds in croconic acid has sparked attention to the topic or proton tranfer type ferroelectrics [20, 161]. In these materials, ferroelectricity or anti-ferroelectricity is mediated through resonance assisted hydrogen bonds (RAHB), which are discussed in Chapter 2.

One class of molecules that has been tied to RAHB and ferroelectricity are cyclic oxocarbon acids of the form $H_2C_nO_n$, including squaric acid (n=4), croconic acid (n=5) and rhodizonic acid (n=6), illustrated in Fig. 4.1. Squaric acid forms polarized sheets in the bulk that stack in such a fashion that the overal crystal is anti-ferroelectric [162]. Croconic acid (CA) crystals have demonstrated above room temperature ferroelectricity, with a polarization of 21 $\mu C/cm^2$ and a low coercive field

of 11 kV/cm [34]. An applied electric field results in cooperative proton tautomerism, where the electric dipole is reversed via hydroxyl proton displacement along the ferroelectric c axis, see Fig. 4.2 for an illustration of this mechanism and Chapter 2 for a more general discussion. This distinguishes proton ordered organic ferroelectrics from other organic ferroelectrics such as vinylidene fluoride (VDF), which require reoritentations of large molecules in an applied electric field to switch the electric polarization and usually exhibit a high coercive field beyond 1200 kV/cm [163].

By contrast, crystals of CA form stacked, pleated hydrogen bonded sheets of molecules with in-plane dipoles, where the polarizations of all sheets are aligned. Each molecule transfers two hydroxyl protons to the carbonyl groups of adjacent molecules within the same sheet, changing the topology of the π-electron system and with it the polarization of each molecule [34, 164]. This implies that for ferroelectricity to occur in proton transfer systems such as CA, 3D crystal structures are not required [?, 34]. There is potential importance of surface-supported 2D ferroelectrics for applications, including memories, logic devices, printable electronics, and organic spintronics. Such development calls for the fundamental, molecular-level understanding of the material properties so that they can be engineered as needed.

Remarkably, rhodizonic acid (RA) has not yet been crystallized [165]. One reason is that RA is very hygroscopic and often found in the form of rhodizonic acid dihydrate [166, 167]. However, there is promise for its usefulness as a ferroelectric. A 2D multiferroic coordination complex consisting of cobalt and RA was recently investigated through first principles calculations and found to support a large stable electric polarization [168]. Experimentally, so far only a few metal-organic crystals containing the deprotonated RA, $C_6O_6^{2-}$ have been reported [165, 169].

Of course cyclic oxocarbon acids are not the only organic species that form hydrogen bonded crystals with the potential for ferroelectricity. Recently, Horiuchi *et*
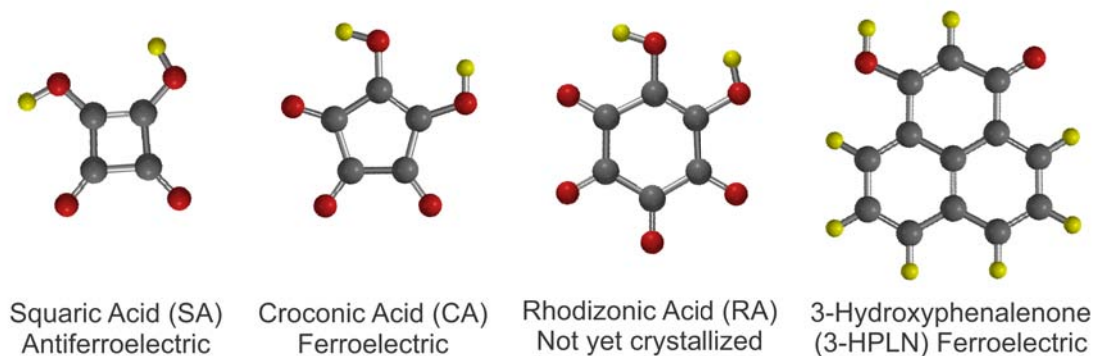
Figure 4.1: Molecules capable of forming resonance assisted hydrogen bonds (RAHB). Of these, three species were chosen for STM studies: croconic acid(CA), rhodizonic acid(RA), and 3-hydroxyphenalenone (3-HPLN).
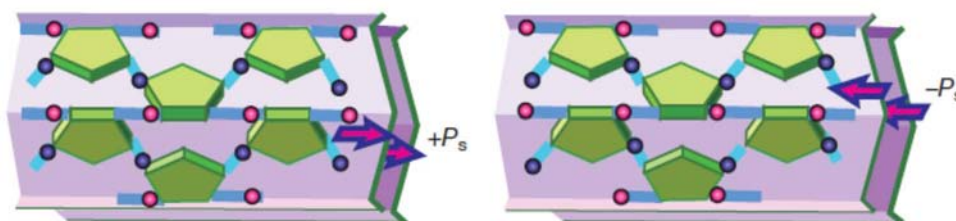
Figure 4.2: Crystalline structure of croconic acid, demonstrating that only single hydrogen bonded sheets are necessary for ferroelectric proton transfer. Reproduced from reference [34].

al. searched the Cambridge Structural Database for possible ferroelectrics by looking for -diketone enol moities with polar crystal structures, and discovered seven new candidates, out of which three proved to be ferroelectric above room temperature [20]. Out of these, 3-hydroxyphenalenone (3-HPLN) has a Curie temperature of >450K and is commercially available. Its crystal structure is composed of 1D chains, which are illustrated in Chapter 2, and which provide the basis for its ferroelectric properties. Thus, similar to CA, surface supported 3-HPLN has the potential to display 2D ferroelectricity.

With this motivation, croconic acid, rhodizonic acid, and 3-hydroxyphenalenone were studied with STM on the (111) faces of Au, Ag, and Cu. Fig. 4.3 displays an overview of the results obtained through STM. Additionally, croconic acid was investigated on a Cu_2N insulting buffer layer to eliminate effects from interactions with metal surfaces. Squaric acid was also examined on the Ag(111) surface. However, the networks were not stable when scanned with an STM tip at 77 K and are not further discussed in this thesis.
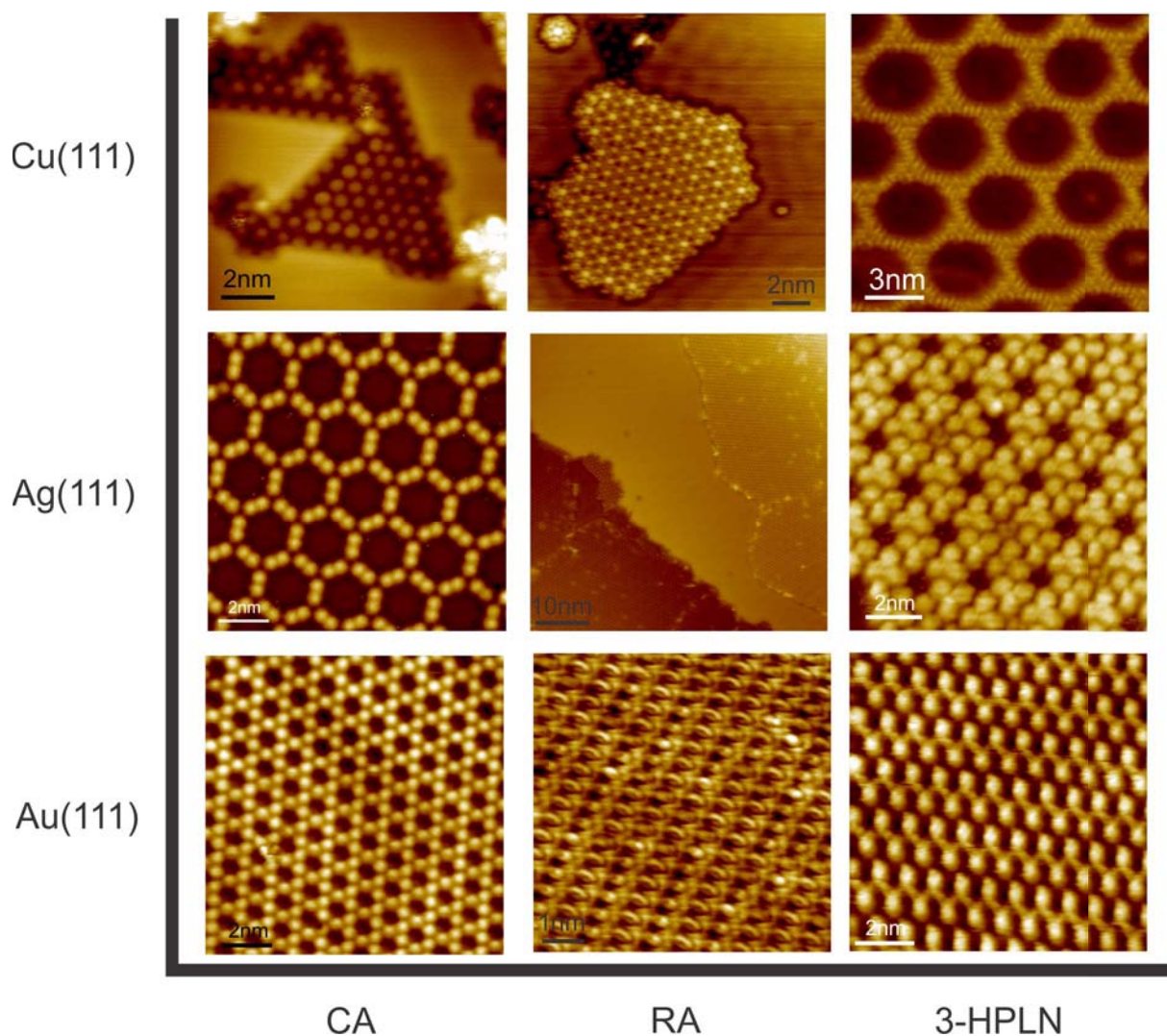
Figure 4.3: Overview of STM images of croconic acid, rhodizonic acid, and 3-hydroxyphenalenone on Au(111), Ag(111), and Cu(111). 3-HPLN on Cu(111) was studied by a colleague and interested readers may see reference [170]. Otherwise, it is excluded from discussion in this thesis.

4.1 STM Investiagations of Surface Supported Croconic Acid

STM investigations were performed on Ag(111), Au(111), Cu(111), and Cu_2N. Experimental observations are complemented by discussion of theoretical results developed

through a collaboration with Dr. Eva Zurek, Dr. James Hooper, and Scott Simpson from the Department of Chemistry at the State Univeristy of New York at Buffalo.

4.1.1   Croconic Acid on Ag(111)

When deposited at room temperature, at low submonolayer coverage, croconic acid (CA) covers Ag(111) with scattered triangular-shaped hexamers, as shown in Fig. 4.4(a). Croconic acid monomers were identified from unfrequent, pseudostable isolated trimers (not shown) to be the individual lobes in (a). From this it follows that CA dimers are the elementary building block for all structures observed, and that each of the triangular-shaped clusters is formed of three such dimers. Upon increasing the coverage to close to one full monolayer, followed by weak annealing to 350 K, honeycomb-type 2D networks as in Fig. 4.4(b) were formed. Images of varied zoom level such as those in Fig. 4.4(b), (c), and (d) reveal important structural details of the networks, labeled with α, β, and γ, which will be discussed later. The observations with STM suggest that the molecules diffuse across the surface, nucleating into dimers which compose the triangular hexamer clusters. At increased coverage the hexamers coalesce, followed by slight rearrangement of the elementary dimers to form the extended 2D networks.

In order to obtain a molecular-level model of the observed structures, molecular and periodic dispersion corrected density functional theory, DFT+D, calculations [172] were carried out, see reference [171] for computational details. Important structural configurations are summarized in Fig. 4.5. The monomer i in Fig. 4.5(a) was found to be 16 meV/atom lower in energy than ii, in agreement with the results presented in reference [173]. Since experiments [165] have shown that the bulk crystal is comprised of the higher–energy monomer ii, it was also considered in our
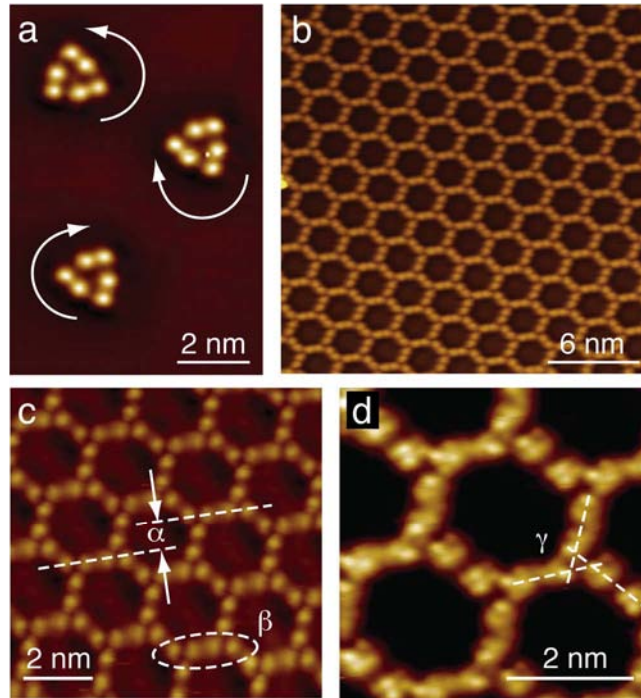
Figure 4.4: Scanning tunneling microscopy images of croconic acid on Ag(111). (a) Triangular hexamers where the arrows indicate the chirality. (b-d) 2D extended networks. See text for explanation of features , , and σ. Reproduced from reference [171].

calculations. The dimerization energy in the gas phase was computed as being 24 and 28 meV/atom for dimers i_2 and ii_2, respectively, with the former being lower in energy by 12 meV/atom. These dimers are the potential building blocks of the hexamers in the low coverage STM images, so these motifs were employed in order to identify structural candidates consistent with those shown in Fig. 4.4.

The lowest-energy hexamer found in our computations was con guration i_6 in Fig. 4.5(b). Rotating the intramolecular C OH bonds a ords a somewhat less stable hexamer ii_6, which, like hexamer i_6, can readily be used to build a model honeycomb lattice that agrees with the high coverage STM image, see Fig. 4.5(d). Hexamers i_6 and ii_6, on the other hand, best resemble the triangular motifs observed at lower coverage in the STM images. Like their i_6 and ii_6 counterpart hexamers which de-

91
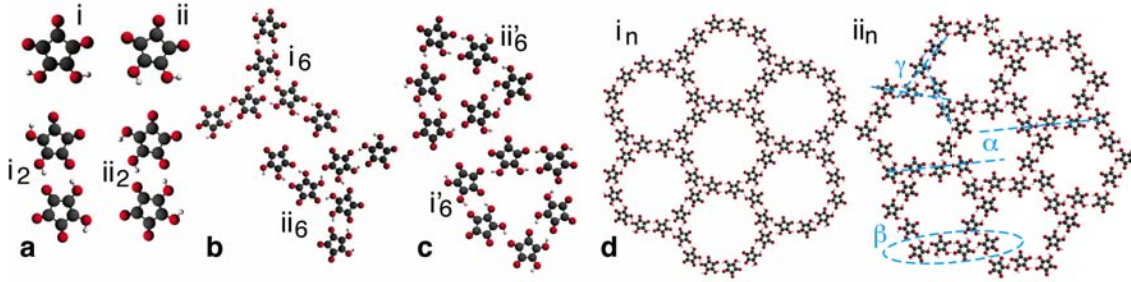
Figure 4.5: Structures of plenary croconic acid monomers, dimers and hexamers, as obtained using rst-principles calculations (a-c). The 2D networks in (d) were constructed from the hexamers in (b). The features and σ are highlighted for comparison with the experiment, see Figure 4.4. Reproduced from reference [171]

scribe the higher coverage regimes, i_6 and ii_6 are composed of three dimeric building blocks, but are 4-6 meV/CA atom higher in energy in the gas-phase. Since clusters of type i_6 or ii_6 are the only observed species at lower coverage in the STM images, it is likely that the actual energy di erence between the hexamer con gurations is di erent for surface supported clusters.

It is interesting to note that the 2D arrangements of CA molecules do not resemble the pleated sheet structure and local molecular arrangement in the bulk crystals. An important consequence of the proposed structures is that they are chiral with respect to the surface. The chirality of a CA molecule of type ii with respect to the surface plane results from the orientation of the two hydroxyl groups, while molecules of type i are not chiral. The dimer ii_2 can only be formed from two molecules of the same chirality. The triangular clusters observed at low coverage consist of three dimers containing molecules only of the same type, and are chiral themselves, also when the atomistic structure of the molecules is ignored. This is indicated by the arrows in Fig. 4.4(a). Interestingly, this chirality can be achieved with the chiral molecule ii as well as with the non-chiral molecule i, as the hexamer models i_6 and ii_6 in Fig. 4.5(c) show.

Extended, two-dimensional networks were constructed from both hexamers, i_6 and ii_6 and are shown in Fig. 4.5(d). There are distinctive structural differences between both types of networks, which we can use to identify the nature of the 2D networks in Fig. 4.4. The symmetry of both networks is described by the wallpaper group $p6$. They both lack reflection symmetry if the atomistic structure is considered, which implies that they are chiral in 2D. Characteristic for network ii_n is that molecular dimers on opposite corners of the hexagonal cell are not aligned collinear (α), 4 molecules on each side of the hexagons appear to be aligned along a linear chain (β) and lines connecting the dimers at the nodes of the network do not meet at the center of the nodes (γ). Careful comparison of those features with the STM images in Fig. 4.4(b, c) shows that the experimentally observed structures must be of type ii_n. The molecules forming it must therefore be of type ii. Network ii_n can be constructed to be left-handed or right handed. The network in Fig. 4.4 is containing only left-handed CA molecules ii.

It should be noted that we also observed networks of type i_n (see Fig. 4.6), albeit with much lower frequency. The symmetry of this network, if only the molecular sites are considered but the atomistic structure of the molecules is ignored, has reflection symmetry and the wallpaper group is $p6m$. This network agrees with honeycomb structures constructed from monomer i and consideration of the atomistic structure of the molecules lowers the symmetry; the wallpaper group is reduced to $p6$, which means that the reflection symmetry is removed. This implies that this network is also chiral.

Because concerted proton transfer is the key mechanism of ferroelectricity in bulk CA, calculations were performed to determine the energy barrier to proton transfer for a dimer of ii_2, as in Fig. 4.5. The energy of proton transfer was calucated along the pathway A-B-C for both the gas phase, black line in Fig. 4.7, and Ag(111) supported
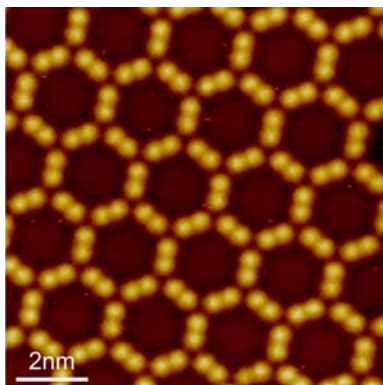
Figure 4.6: STM image of an achiral network corresponding to architecture i_n, described above.

system, red line in Fig. 4.7.
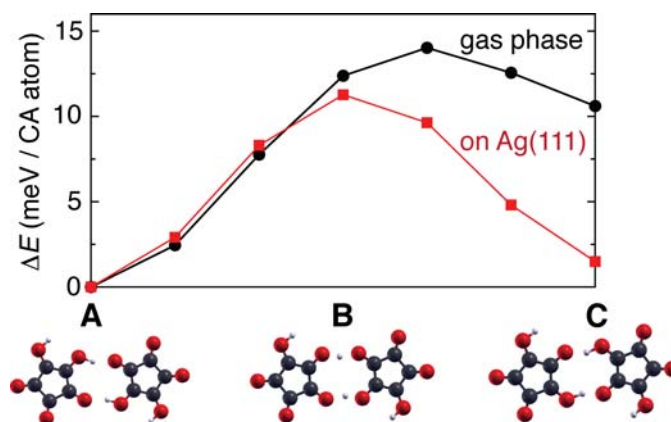
Figure 4.7: Relative energies of hydrogen transfer pathway for dimer ii_2, A to C, calculated using DFT-D2 and a periodic program. The points along the pathway were taken from a linear interpolation of the position between A and C. Reproduced from reference [171].

An extended honeycomb network, which corresponds to the experimentally observed network in Fig. 4.4(b)-(d), was constructed, labled HC_A in Fig. 4.8. Molecular dynamics simulations were carried out for this network constrained to lie in a plane, both in the gas phase and on a two-layer Ag(111) slab. In both cases spontaneous

proton transfer occurs. In the gas phase, the structure optimizes after 130 fs to HC_B. This structure is polarized, such that each molecule has nearly an 8 D dipole moment. In the simulations on the Ag(111) surface, the structure optimizes to HC_D, with proton transfer occuring after approximately 100 fs.
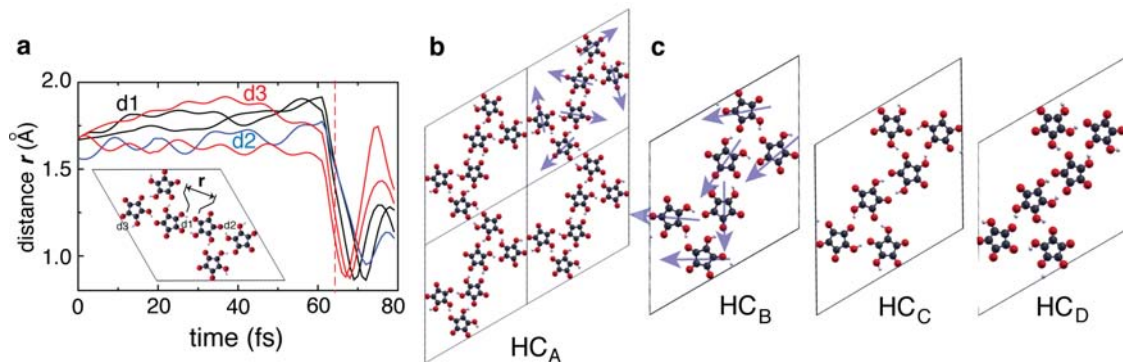
Figure 4.8: (a) Select $O\cdots H$ distances in HC_A, as labelled in the inset, computed during an ab–initio MD simulation where all of the atoms were constrained to remain in the plane of the honeycomb. The inter and intramolecular OH bond in a CA dimer measures 1.65 and 1.01 Å. (b) A honeycomb network which corresponds to the high–coverage STM images. (c) Three other honeycomb structures which differ mostly in the arrangement of the hydrogen atoms. The direction of the molecular dipoles is indicated with blue arrows. The configuration HC_B exhibits a net dipole..

In the gas-phase simulations, HC_D was found to optimize back to HC_A. However, on the Ag(111) surface, even though the energy per molecule was 64 meV higher for HC_D compared to HC_A, HC_D was stable and did not spontaneously optimize to HC_A. As such, this presents the intriguing possibility in materials design to engineer the interface such that a system mimics these DFT results. Namely, the goal is to optimize the potential energy surface such that the energy difference between HC_A and a polar network, such as HC_B, decreases.

4.1.2 Croconic Acid on Au(111)

When deposited at room temperature on Au(111), croconic acid self-assembles into extended porous networks, in which the basic building block is a hydrogen bonded trimer of CA, visible in Figure 4.9(a). Each molecule forms hydrogen bonds with four nearest neighbors. The networks are large, often over 100 nm across, and singly domained. A proposed model for these networks is shown in Figure 4.9(c). The networks exhibit *p3* symmetry when taking into account the shape of each croconic acid molecule, and thus display a chiral structure. If the internal structure of CA is ignored, the networks exhibit *p6m* symmetry which is achiral. These networks are in sharp contrast to the networks previously reported by us on Ag(111) in which a dimer, and not a trimer, is the basic building block and for which different phases corresponding to different monomer building blocks were observed, as described in the previous section.
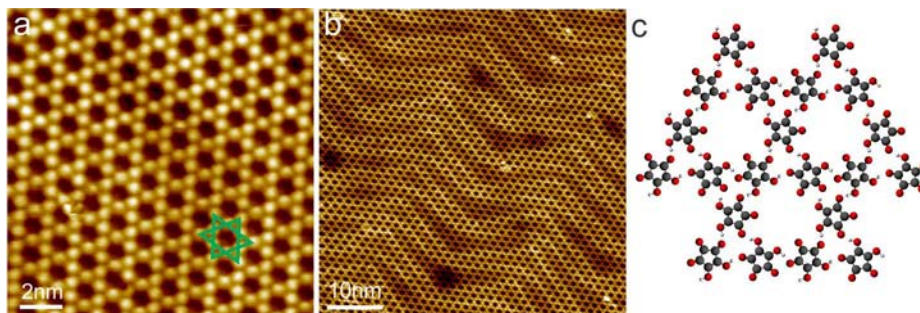
Figure 4.9: (a) STM image of croconic acid deposited at room temperature on Au(111) taken at -0.1 V, 350 pA; green triangles highlight Kagome geometry. (b) STM image exhibiting uniformity of large domains, taken at 0.7 V, 350 pA and (c) proposed model of porous croconic acid network with trimer as the building block.

The Au(111) surface reconstructs into a herringbone pattern, which can be seen rippling underneath the CA networks, especially in Fig. 4.9(b). These herringbone ridges lie along the ⟨212⟩ directions and thus are aligned 30° to the densely packed directions of the underlying Au lattice [132, 133]. The direction of molecular rows

with respect to the Au substrate varies between different islands and a number of different orientations exist. This implies that there is not a strong epitaxial fit to the Au surface and that the molecules do not bind to specific sites on the surface. The average molecular separation along a molecular row is 7.2 Å $\pm$ 0.2 Å, from which is it concluded that the networks are incommensurate with the underlying surface. To further strengthen the picture of a weak surface/CA interaction, at low coverages of CA, approximately less than 0.5 ML, the networks are highly unstable when scanned. The networks often break apart as the tip scans over them. However, above a critical coverage the honeycomb networks become more stable. Finally, the observation of few nucleation events followed by the growth of very large islands is consistent with a high mean free path of CA.

Closer inspection of the geometry reveals that CA forms a 2D Kagome-like lattice on Au(111), highlighted in green in Figure 4.9(a). Kagome lattices are of wide scientific interest, ranging from being theoretically linked to a variety of novel magnetic properties including high temperature superconductivity [174–176] to being excellent templates for studying host guest chemistry due to having two differently sized regular pores. Admittedly, the smaller pore here is impractically small. Despite scientific interest in Kagome lattices, there are few natural examples and synthetic Kagome lattices have proved difficult to create. Until recently, the only Kagome lattices were complex, inorganic structures that were difficult to make defect free [174]. The first reported nanoscale Kagome lattice was synthesized in 2002 [177] and since then a spate of new nanosized organic Kagome lattices have been synthesized with the help of modern surface science techniques. These lattices exhibit a variety of chemical bonds, including hydrogen bonds [178–181], metal coordination bonds [182], CN-π bonds [183], and van der Waals forces [184–187]. More broadly, Kagome lattices have been recently synthesized in a liquid crystal form [188], using DNA [189], and even

on the micrometer scale using colloidal spheres [190]. Therefore, this newly created CA network joins a rapidly expanding group of novel Kagome lattices.

4.1.3   Metal Organic Networks of Croconic Acid/Cu

When deposited at room temperature onto Cu(111), CA self-assembles into small islands which display a high level of disorder, as is illustrated in Fig. 4.10(a). Dark holes, or etch pits, appear in the surface which are one atomic layer high, implying missing Cu atoms. Similarly, the step edges are eroded, further suggesting missing Cu atoms. From this it is inferred that even at room temperature, CA is pulling atoms from the surface. Because there are no islands of Cu visible, it is concluded that the Cu atoms are being incorporated into the islands of CA.

The sample was annealed incrementally, up to a temperature of approximately 165°C. With each annealing stage, the step edges become increasingly eroded and larger holes appear in the Cu surface. The degraded areas (both steps and holes) are filled with CA molecules. Fig. 4.10(b) shows two holes on the left of the image, with a heavily degraded Cu step running down the center of the image. CA fills the area to the right of the image where Cu has been removed. One triangular shaped hole that is filled with CA is highlighted in Fig. 4.10(c). While small domains of CA appear ordered, large scale ordering is never achieved.

The geometry of the small ordered domains varies from rectangular as in Fig. 4.10(b) to hexagonally symmetric, as in Fig. 4.10(c), which is striking given the five-fold symmetry of the CA carbon ring. Atomic resolution was never achieved for the Cu adatoms that are presumed to be metal linkers in the networks. Therefore, bonding models can not be inferred from the images.

The formation of metal organic bonds is often accompanied by a deprotonation
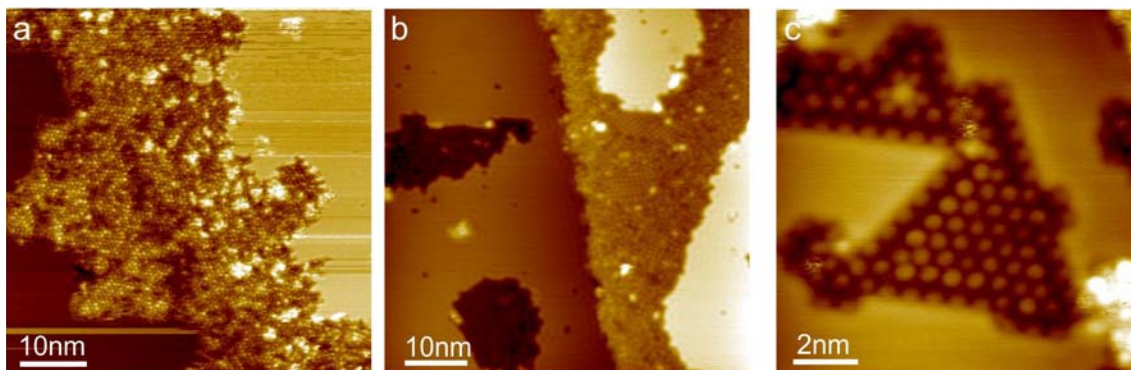
Figure 4.10: STM images of croconic acid on Cu(111). (a) As deposited at room temperature. (b) After annealing to ∼165 C large holes appear in the surface, indicitive of atoms being removed and utlized by CA. (c) Zoom in on a hole in the Cu surface after being annealed to ∼87 C. Note the holes are lled with molecules which occasionally exhibit order. Tunneling parameters: (a) 1 V, 400 pA (b) 0.15 V, 300 pA (c) 0.8 V, 250 pA

reaction [153, 154, 191]. For the case of CA, deprotonation would exclude the possibility of proton transfer type ferroelectricity on the Cu(111) surface. However, the inclusion of Cu adatoms into bonds opens the possibility for the future use of utilizing magnetic linker atoms to create novel magnetic materials.

4.1.4 Croconic Acid on an Insulating Copper Nitride Bu er Layer

As demonstrated throughout this thesis, surface-molecule interactions control many functional properties of organic adlayers. In order to determine what role the substrate plays in STM studies of CA, the metal could, for instance, be replaced by something that is inert, or electrically neutral, such as an insulating bu er layer. A few di erent bu er layers have successfully demonstrated this functionality. Namely, boron nitride monolayers grown on Rh(111) have been used to decouple C_{60} [192], Sn and Pb atoms [193], and Co nanoclusters [194]. Single and multilayer NaCl lms

grown on Cu(111) and Cu(100) decouple pentacene molecules from the metal surface, allowing for imaging of their true geometry [195]. Noble gas buffer layers, such as Xe, have been used in buffer layer assisted growth (BLAG) of metal clusters, in which the adsorbed metal atoms are decoupled from the substrate by the noble gas layer [196, 197]. Cu_3N was shown to decrease the interaction between Co-TPP and a Cu(110) substrate such that the density of states appeared similar to the gas-phase predictions [198]. Finally, a Cu_2N buffer layer magnetically decoupled a spin-crossover complex from a Cu(100) surface. The effect of this was that the spin state was pinned on the bare metal surface, but spin state switching was allowed on the insulating layer [18].

With this in mind, an ultrathin insulating buffer layer was utilized to study croconic acid decoupled from any metal surface. Due to the ease of synthesis, and previous success in the literature, Cu_2N was chosen as the prefered buffer layer. The synthesis procedure described in reference [199] was followed. Namely, a clean Cu(100) crystal was sputtered in an N_2 atmosphere of pressure $3 \cdot 10^{-6}$ T with an electron energy of 500 eV for twenty minutes. Then the sample was annealed to a temperature of approximately 350°C for five minutes. This resulted in approximately full monolayer coverage of Cu_2N, for which a typical STM image is shown in Fig. 4.11(a). Monolayer deep trenches are observed and ascribed to N-N repulsion, which is fully described in reference [199]. On some Cu_2N terraces, bright lines are also faintly observed, as in Fig. 4.11(a) . These are Cu ridges, which do not contain N. They appear brighter in an STM image despite being geometric depressions due to their increased conductivity. N adsorbs onto the Cu(100) lattice into the fourfold hollow sites, creating a square lattice rotated 45° from the underlying Cu(100) lattice. A model showing the two overlying lattices is presented in Fig. 4.11(b).

Room temperature deposition of CA onto prepared Cu_2N layers results in a disor-
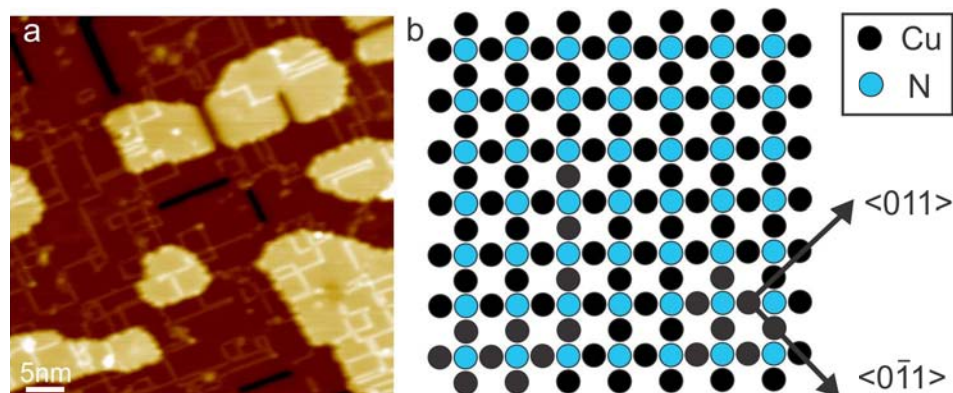
Figure 4.11: Typical STM image of bare Cu_2N bu er layer as grown on Cu(100). Tunneling parameters: 0.6 V, 500 pA.(b)Model of N lattice oriented 45 from the underlying Cu lattice.

Measured Feature	Spacing(nm)	Uncertainty(nm)	Model Spacing(nm)
Along a chain	0.72	0.04	0.72
Across a chain	0.76	0.08	0.81

Table 4.1: Measured spacings of croconic acid on Cu_2N

dered phase, such that in STM images individual CA molecules cannot be discerned. However, annealing to approximately 110-120 C results in the ordering of CA. A large scale image of CA on Cu_2N post annealing is shown in Fig. 4.12(a). The molecules primarily self-assemble to form chains that are two molecules across. The chains attract each other and typically align along the two directions of densely packed N atoms. The measured molecular spacings are summarized in Table 4.1. Zoomed-in images, such as the image shown in Fig. 4.12(b) show the atomically resolved N lattice.

From analyzing STM images, such as those in Fig. 4.12, a few points can be discussed. First, note that the molecules do not fully wet the surface, meaning that short, separated chains are observed and not large 2D networks. Increasing the annealing temperature does not cause the islands to grow larger. This is in contrast to fullerene deposited on Cu_2N which fully wets the surface at room temperature [200].
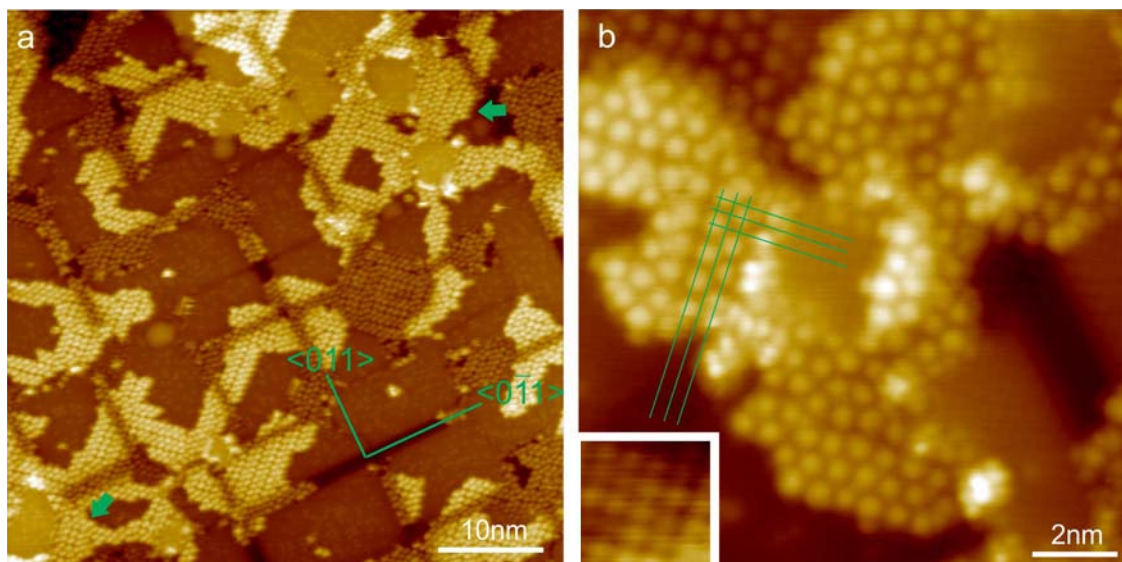
Figure 4.12: (a) STM image of croconic acid adsorbed onto a Cu_2N bu er layer grown on Cu(100). The densely packed directions of the Cu(100) lattice are marked, implying the the CA chains align along the N lattice direction. Green arrows indicate CA chains that bridge monolayer steps. (b) STM image with green lines highlighting N atomic lattice. Note that some disorder and competing CA phases exist on the sample. Inset shows zoom in of atomically resolved N lattice. Tunneling parameters (a) -1 V, 700 pA (b) 0.65 V, 280 pA

It is, in fact, more similar to metal growth, namely Fe and Ni, which both do not wet the surface at low coverages [201, 202].

A second observation is that nucleation of CA in the second layer is frequently observed. For example, in Fig. 4.12(a) green arrows indicate areas in which two steps are observed that di er by a monolayer height. However, the CA chains on both islands have the same aparent height. From this it can be inferred that the lower island consists of a double layer. Under this assumption, it is observed that second layer CA molecules adsorb directly on top of rst layer molecules. This suggests -stacking of molecules, similar to the bulk crystalline structure, which is discussed in detail below.

From STM images showing the atomically resolved N lattice, such as Fig. 4.12(b),

it is determined that the molecules bind along the densely packed direction of N atoms, i.e the 100 direction of the Cu(100) surface. Furthermore, by extending gridlines over the N atomic lattice, it is seen that each CA molecules binds directly over an N atom. By placing the molecules at the experimentally determined distances, given in Table 4.1, a bonding scheme that accounts for these observations is proposed in Fig. 4.13.

Figure 4.13: A proposed model for the bonding of CA on Cu_2N. N is represented by blue atoms and Cu by brown atoms. Note that surface epitaxy and not intermolecular bonds are driving the self-assembly.

It is worthwhile to compare the 3D crystalline form of CA to its 2D bonding on Cu_2N. The 3D structure of croconic acid consists of sheets of hydrogen bonded
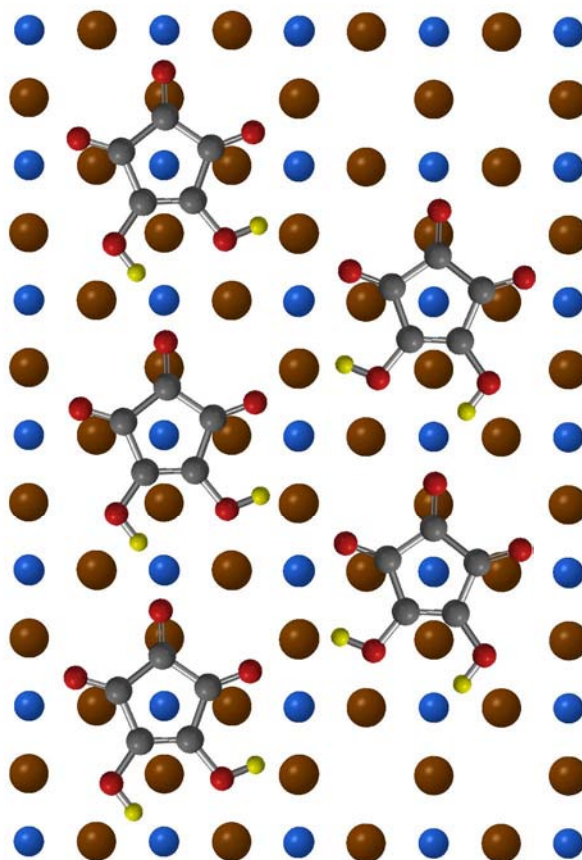
molecules, with each molecule having one H-bond to each of four neighbors, as is illustrated in Fig. 4.14(a). These sheets are not flat, however. Instead there is a 69.9° kink between every other row, with a black box indicating the double rows which are parallel to each other in Fig. 4.14(a). A side view of the crystal, shown in (b) and (c), illustrates this pleated shape. The related compound squaric forms similar hydrogen bonded sheets. However these remain flat, without the kinks observed for CA [203]. It is still currently unknown whether the kinks result from strain or an electronic effect [203]. Both the 3D crystal and the 2D surface supported structures exhibit close-packing of the CA molecules, in contrast to surface supported assemblies on noble metals. However, the 2D structures here are determined from the N-N lattice spacing, whereas the bulk structure is driven by hydrogen and π-π bonding.

Fig. 4.15 compares the self-assembled structures of CA on the metal surfaces discussed above, Ag(111) and Au(111), with the results obtained on Cu_2N. From these images, it is clear that the areal density of molecules in one monolayer increases from Ag to Au to Cu_2N. The number of hydrogen bonds per molecule is constant at four for all cases, however the number of neighbors per molecule differs from four on Au to three on Ag and Cu_2N. Two possible explanations for this trend will be proposed next.

Croconic acid aquires different quantities of charge on each of these surfaces, ranging from approximately -0.30 e^- on Ag [204], to -0.07 e^- on Au [204], and it can be assumed appoximately 0 e^- on Cu_2N. Coulombic repulsion between charged molecules would account for the decrease in packing density observed for Ag compared to Au. Since CA remains neutral on Cu_2N, it is free to adopt the close packed configuration that is observed.

Thermodynamic considerations provide a second possibility for explaining the different observed packing densities. Self-assembly can be understood as forming
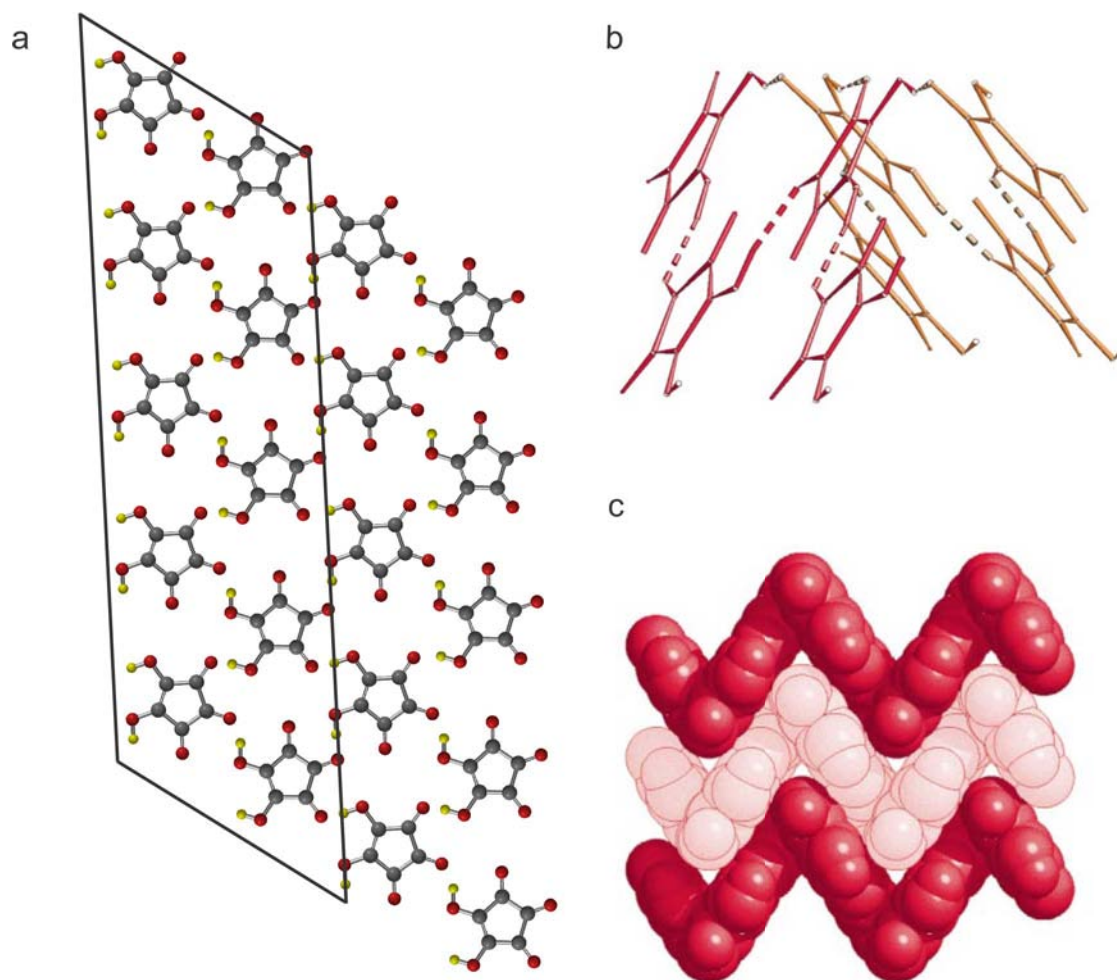
Figure 4.14: (a) The crystalline structure of croconic acid. (b) Side view highlighting the chain nature of sheets. (c) Side view indicating pleated structure. (b,c) Reproduced from reference [165].

structures which minimize the Gibbs free energy [205]. Recall that the Gibbs free energy is given by:

$$G = H - TS \tag{4.1}$$

where H is the enthalpy, T the temperature, and S the entropy of the system. When molecules condense into solid structures, they lose various entropic contribu-
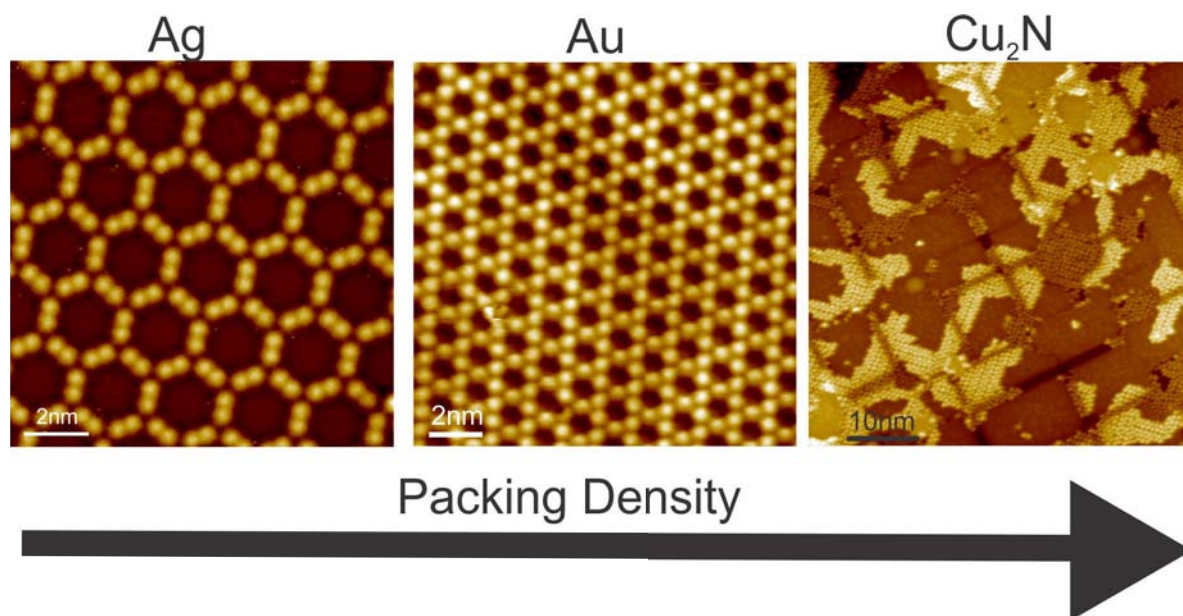
Figure 4.15: STM images showing increased molecular density of croconic acid as deposited on Ag, Au, and Cu_2N.

tions, such as translational and rotational entropy, which increases the Gibbs free energy by decreasing S. However, adsorption to a surface makes æ H more negative, which decreases the Gibbs free energy. It is the relative competition of H and S which potentially drives the equilibrium self-assembly of organics.

There are examples in the literature of molecules at the liquid-solid interface switching from a porous to densely packed con guration with increased solute concentration that were explained by calculating these thermodynamic quantities [205,206]. It was found in one case that a strong surface interaction was responsible for the signi cant enthalpic contribution to the Gibbs free energy [205], which was the driving force for an observed densely packed structure. CA exhibits a strong epitaxial t to the Cu_2N surface, implying a strong surface interaction. Thus, enthalpic considerations may be the driving factor for the di erent packing densities. However, theoretical thermodynamic calculations are needed to resolve this question.

4.2 STM Studies of Surface Supported Rhodizonic Acid

This section presents STM studies of rhodizonic acid (RA) on the noble metal surfaces of Au(111), Cu(111), and Ag(111). First principles density functional theory calculations, performed by Dr. Eva Zurek, Dr. James Hooper, and Scott Simpson of the State University of New York at Buffalo, are also discussed here. These calculations provide a deeper theoretical underpinning to the experimental results.

4.2.1 First Crystallization of Rhodizonic Acid on Au(111)

As noted in the introduction, rhodizonic acid has not yet been crystallized in 3D, in part due to its hygroscopic nature. The hydration of the carbonyl groups opposite the hydroxyl groups in RA was established as one of the first controllable and reversible dehydrations of a solid hexol, in this case $H_8C_6O_8$ [165]. The experimental treatment of the RA in this study, however, strictly followed a procedure that has been proven to dehydrate the RA [167]. The dihydrated RA was gently warmed under ultra-high vaccuum conditions until fully converted in pure RA. This conversion was confirmed by monitoring the color change. Dihydrate RA is described as being "colorless" [166], pure RA as deep orange [165], and $C_6O_6{}^{2-}$ as deep yellow [207]. Shown in Fig. 4.16(a) is the RA powder before putting it into the vacuum chamber which shows a gray, "colorless" hue. After performing the dehydration procedure, the powder was removed from UHV, see Fig. 4.16(b), and was a bright orangish color, consistant with the literature. Keeping the sample under atmospheric conditions for 90 minutes resulted in the powder adsorbing water and returning to the original gray color, as is shown in Fig. 4.16(c). Considering this, it is concluded that the experimental RA layers were

formed of the dehyrated substance under UHV.
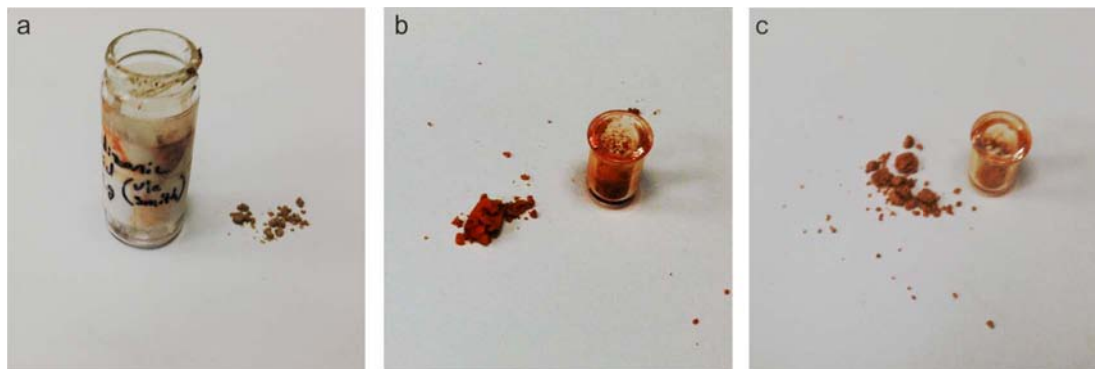
Figure 4.16: Photographs demonstrating the color change associated with dehydration of dihydrate RA into pure RA. (a) Dihydrate powder with a gray color. (b) Subsequent vacuum heating dehydrates the powder into RA which is a deep orange.(c) After leaving the powder in atmosphere for 90 minutes the color begins to change back to (a) as water vapor is absorbed.

When evaporated under ultra-high vacuum onto Au(111) at room temperature, RA forms extended molecular networks exhibiting extremely large domains of hexagonal symmetry, with an intermolecular spacing of 6.8 0 2 A, as illustrated in Fig. 4.17. The networks grow across the herringbone reconstruction of Au [132], which is visible as bright ridges below the molecular layer, without lifting this reconstruction. They are limited in size by the coverage alone, meaning that often only one extended island is observed on a terrace. This observation is characteristic of a large mean free path for the molecules upon adsorption and a low di usion barrier on the Au(111) surface. It is also found that annealing the sample even slightly above room temperature results in the gradual decrease in the island size due to desorption of the RA from the gold surface, which implies that the molecules are only weakly bound to the surface. No changes in the network architecture itself were observed after annealing. Imaging at certain bias voltages achieved submolecular resolution and reveals an alternating crescent shape pattern, as is illustrated in Fig. 4.17(b), which was obtained

at -1.4 mV.
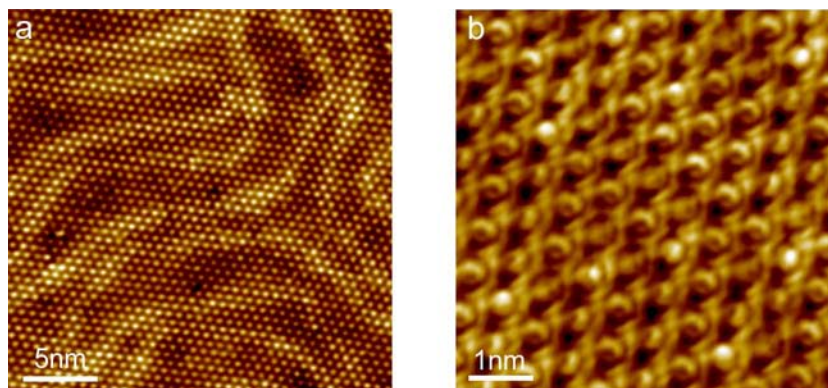
Figure 4.17: STM images of RA on Au(111). (a) Note the hexagonal symmetry and large domain size of the networks. (b) Zoom in of RA, with submolecular resolution. Tunneling parameters: (a) 1 V, 700 pA (b) -1.4 mV, 250 pA

Density functional theory calculations were performed on a simulated RA network, computational details are provided in reference [42]. The calculated spatial distributions of the LUMO (lowest unoccupied molecular orbital), HOMO (highest occupied molecular orbital) and HOMO-1 of RA all show a crescent shape (see Fig. 4.18), but the orbitals of the deprotonated RA (rhodizonate) $C_6O_6^{2-}$ do not, see Fig. 4.18. For example, the HOMO-1 orbital of RA (and therefore its charge density), which is of -symmetry with respect to the plane of the molecule, is localized mostly on the hydroxyl-side of the carbon ring. The HOMO (-symmetry) and LUMO (- symmetry) are localized on the opposite side of the molecule (Fig. 4.18). The crescent shape observed for the molecular orbitals of RA corresponds well with the sub-molecular resolution achieved in STM images, such as Fig. 4.17(b). From the symmetry of the appearance of the molecules in STM images and its agreement with the shape of the calculated frontier orbitals, it is concluded that the molecules adorbed on Au(111) are in fact RA and not the deprotonated analog. Thus, the results presented in Fig. 4.17 and in reference [42] represent the rst reported crystallization of RA.
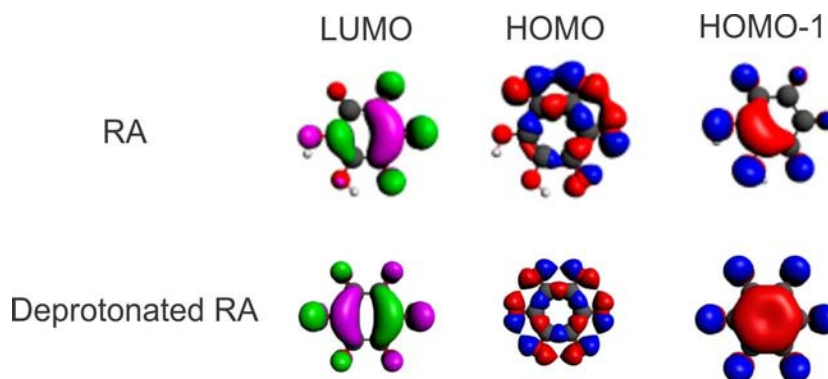
Figure 4.18: Molecular orbitals of rhodizonic acid (RA) top, and the doubly deprotonated analog, rhodizonate ($C_6O_6^{2-}$) bottom. Note that the molecular orbitals of RA have a crescent shape while the deprotonated species are symmetric.

4.2.2 Metal Organic Networks of Rhodizonate on Cu(111)

In designing 2D crystal structures with potential applications in mind, it is desirable to have bonds that are strong enough to be stable at room temperature, but not so strong as to impede defect correction at the molecular level. Metal coordination bonds are stronger than hydrgoen bonds and van der Waal forces as was shown in Chapter 2, but weak enough to self-correct and provide low defect networks [208]. Metal organic coodination networks can be tailored to have mesoscale pores [209], and are su ciently adaptable to grow over step edges and defects seamlessly [210]. Furthermore, they provide an opportunity to study magnetic metals as linkers [191] and unique coordination which is not observed in 3D [211]. Thus with broad applications to both devices and fundamental physics and chemistry in mind, studies of surface supported metal organic chemistry are important.

When deposited at room temperature on Cu(111), RA forms small, isolated islands that contain structural defects, with occasional nucleation of a second layer (Fig. 4.19(a)). Given the identical symmetry of this network and the intermolecular spacing of 0.65 nm   0.05 nm that is, within experimental error, identical to the

spacing of RA on Au(111) in Fig. 4.17, it is concluded that this network is identical to the hydrogen-bonded network reported on Au(111), even though the asymmetric appearance of the molecules was never recorded.
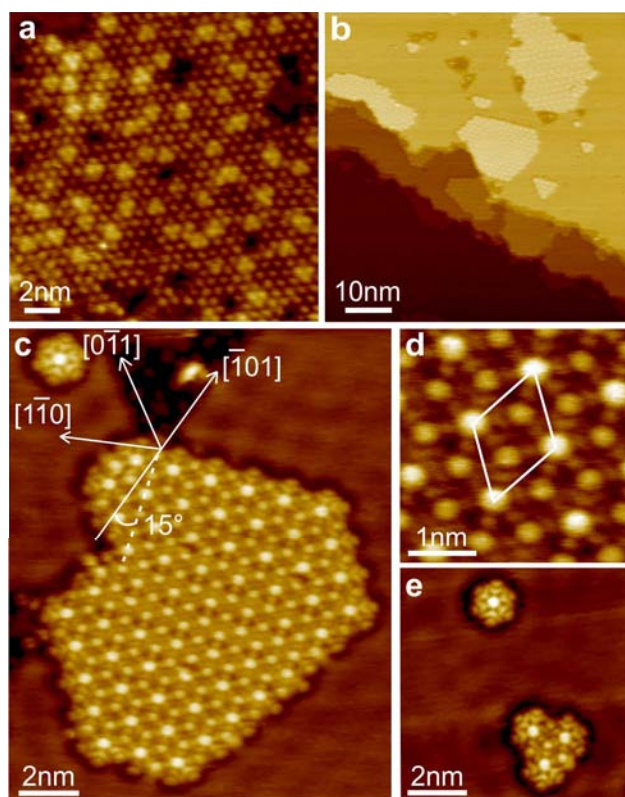
Figure 4.19: STM images, recorded at 77K, of rhodizonic acid (RA) on Cu(111) deposited at room temperature (a) and after annealing (b-e). Note that on (b) the step edges are jagged and that holes in the substrate are visible. Image (c) highlights a 15 orientation relation between the 110 substrate direction and the symmetry axis of the island. (d) Close up of one island with unit cell highlighted. (e) Magic clusters of RA. Tunneling parameters: (a) 0.6V, 400pA (b-e) 0.08V, 250 pA

Weak annealing of the sample to approximately 360 K, however, results in new structural phases of RA, seen in Fig. 4.19(b e). The annealed islands are more uniform in shape, exhibit fewer defects, and are of single layer height. Characteristic monolayer deep holes in the terraces of the Cu(111) substrates are now observed, along with a roughening of the substrate step edges. Some of the holes in the ter-

races are filled with molecules, where they form the same network as on top of the terraces. What is striking is that the architecture of the networks has changed drastically, exhibiting a change in the local environment and the apparent height of each molecule.

Isolated clusters, which appear to be the basic building blocks of the networks, are frequently observed, such as in Fig. 4.19(c,e). Such clusters always appear in groups of 1 or 3 (Fig. 4.19(e)). The molecules are visible as the bright lobes in the islands, and every third molecule in a row has increased brightness that corresponds to an increased apparent height of 0.2 Å. There are smaller structures connecting these bright lobes, visible in Fig. 4.19(d,e), which are identified as Cu atoms linking the molecules together. The clusters at the top of Fig. 4.19(e) are considered to be "magic" because they occur only in this particular configuration and size. The concept of magic clusters originates from gas phase cluster physics [212] and has been recently applied to surface-supported clusters [76]. It refers to particularly stable configurations of atoms or molecules [212–214]. Magic clusters, including the RA/Cu clusters, will be discussed in depth in Chapter 6.

The molecule-to-molecule spacing, measured at 77 K increased from 6.5 ± 0.5 Å to 7.3 ± 0.3 Å after annealing at approximately 360 K. Together with the observation of triangular holes in the surface and visibly rough steps, this increased spacing supports the proposal that substrate Cu atoms serve as linkers in the networks, thus enabling the formation of a two-dimensional metal–organic coordination network (MOCN). While atomic resolution was not achieved for the (111) surface of Cu, the $\langle 1\bar{1}0 \rangle$ orientations within the surface plane can be inferred from the orientation of the boundaries of the holes in the substrate. Using this as a guideline, it is noted that the three symmetry directions of the networks are aligned approximately 15° offset to the $\langle 1\bar{1}0 \rangle$ crystallographic directions of the surface, as illustrated in Fig. 4.19(c).

Thus, two different orientations of molecular islands $\pm$ 15° to the Cu substrate lattice are expected, and both are observed experimentally.

As a starting point for the detailed structural analysis of the MOCN of RA with Cu, a molecular first-principles program was used to calculate the energy of substituting hydrogen atoms in a RA dimer with Cu or Au atoms, $(H_2C_6O_6)_2$ + 2 M $(HC_6O_6)_2M_2$ + H_2, where the metal, M, is either Cu or Au. See reference [42] for the computational details. The right-hand side of the reaction is favored by an additional 1.22 eV when Cu is introduced versus Au, suggesting that the coordination bond of RA with Cu is substantially stronger than with Au.

Structural models developed from STM results were also tested by DFT, see reference [42]. Fig. 4.20(a) displays the bonding model that reproduces all of the key experimentally observed features. It consists of deprotonated rhodizonate molecules bonded in a hexagonal lattice with Cu adatoms as linkers, with an intermolecular spacing of approximately 7.4 Å, in excellent agreement with experiment. Simulated STM images, such as that shown in Fig. 4.20(b), show the observed difference in brightness of every third molecule. From close inspection of Fig.4.20(a) one can note that every third atom occupies a different surface adsorption site (top or hollow) and also varying number of Cu atoms to which it is coordinated (six or three). One may ask whether the observed difference in contrast between molecules is due to differences in adsorption sites or to the uneven Cu adatom coordination. In order to answer this question, STM images of the rhodizonate molecules on different adsorption sites were calculated. No significant contrast differences was obserserved. Thus, it is concluded that the different apparent height in STM images of rhodizonate molecules is due to different Cu coordination.

The deprotonation of the RA molecules on the Cu surface upon annealing is analogous to findings for several other classes of molecules on Cu [191, 215–217]. Notably,
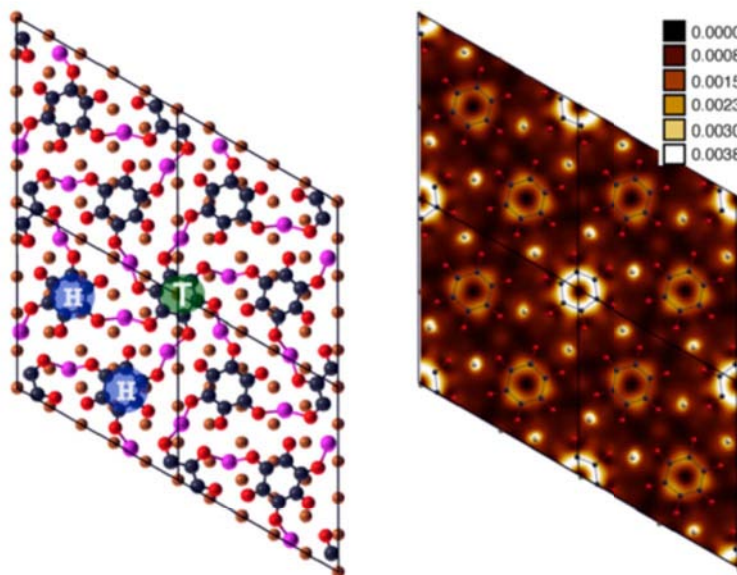
Figure 4.20: (a) Model of rhodizonate and Cu MOCN on Cu(111). Molecules adsorb to either hollow (H) or top (T) binding sites. Molecules on top sites coordinate to six Cu atoms, whereas molecules on H sites coordinate to three atoms. (b) Simulated STM image of MOCN. Reproduced from reference [42].

a wide variety of different molecules, including 1,3,5-tris(4-mercaptophenyl)benzene (TMB), 1,3,8,10-tetrazaperopyrene (TAPP), oxalic acid, among many others deprotonate upon adsorption to crystalline Cu, which for carboxyl groups is known to be catalyzed by the lattice gas of Cu adatoms [149, 154, 218]. Once deprotonated, molecules often form metal coordination bonds with the present Cu adatoms, which was demonstrated conclusively for trimesic acid (TMA) [191]. Some of these molecules require thermal activation in order to deprotonate. The temperature at which deprotonation occurs depends not only on the type of molecule used, but also on which crystal face of Cu is exposed, since the density of adatoms evaporating from Cu is higher for the (110) facet than the (111) facet [219]. Interestingly, the properties of surface-supported metal coordination networks are often different than their traditional solution or crystalline counterparts. Two-dimensional metal coordination net-

works can exhibit nontraditional electronic properties, such as charge-donating metal linkers that are directly attributable to the influence of the surface [220]. This surface hybridization makes determining unambiguously the oxidation state of the metal coordinating atoms impossible. While deprotonation of RA on Cu(111) excludes the possibility of proton transfer type ferroelectricity, the coordination of metal atoms makes possible the use of magnetic linker atoms for novel magnetic RA based materials.

4.2.3   Rhodizonic Acid on Ag(111)

When deposited on Ag(111) at room temperature, RA forms extended islands exhibiting hexagonal symmetry, as is shown in Fig. 4.21(a). The average intermolecular spacing is 0.70 ± 0.01 nm which, within the uncertainty, is equivalent to the room temperature networks observed on both Au(111) and Cu(111). Thus it is concluded that these networks exhibit the same bonding as was described for those systems. Occasionally, networks with a brighter contrast and a larger spacing of 0.78 ± 0.03 nm are observed. One of these is highlighted with a green arrow in Fig. 4.21(b). These networks correspond with areas in which the step edges appear to be partially eroded. As was discussed for RA on Cu(111), step edge erosion is indicitive of metal adatoms being utilized in the networks.

Anealing the sample to approximately 82°C results in the disappearance of the original room temperature networks and a conversion to the larger, brighter networks, shown in Fig. 4.17(c). Annealing increases the density of adatoms, and the resulting networks are consistent with the proposal of a metal-organic coordination network. Unlike the Cu/RA metal-organic coordination network, Ag atoms were unable to be resolved with STM. However, the spacing of these networks, 0.78 ± 0.03 nm is,
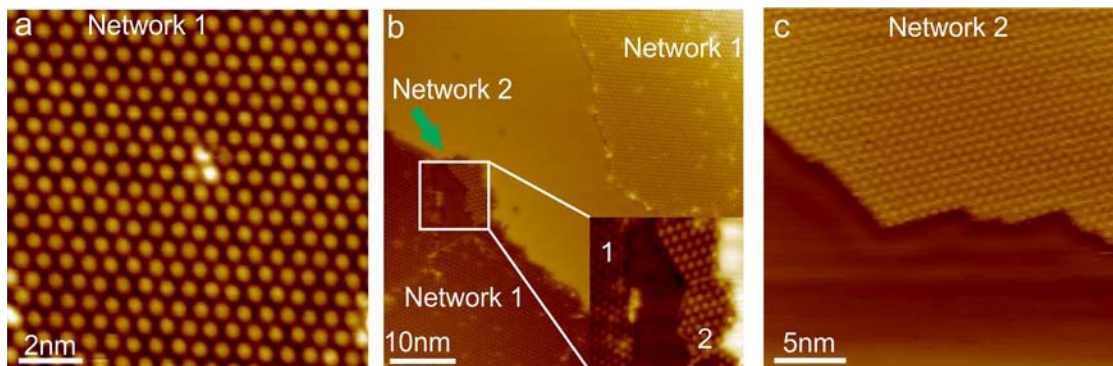
Figure 4.21: (a,b) STM images of room temperature deposition of RA on Ag(111). Green arrow highlights eroded step edge and network with larger spacing. (c) STM image of RA on Ag(111) after annealing to 82 C. Network 1 indicates hydrogen bonded networks and network 2 indicates MOCN. Tunneling parameters: (a) 0.2 V, 300 pA (b) 0.2 V, 300 pA (c) 0.1 V, 500 pA.

within the experimental error, equal to the MOCNs observed on Cu(111). Therefore, it is concluded that rhodizonic acid forms a similar MOCN as the one observed on Cu(111).

4.3   3-Hydroxyphenalenone on Noble Metals

3-Hydroxyphenalenone (3-HPLN) was studied with STM on Ag(111) and Au(111). Results of 3-HPLN on Cu(111), displayed in Fig. 4.3, were completed by a co-worker, Sumit Beniwal, and are outside the scope of this thesis. As part of the theoretical collaboration with Dr. Eva Zurek, Dr. James Hooper, and Scott Simpson, DFT results are presented which provide additional depth and understanding to the experimental results.

4.3.1 Chiral Networks of 3-Hydroxyphenalenone on Ag(111)

When deposited onto Ag(111) at room temperature, 3-HPLN coalesces into short chains that are two molecules across, similar to the chain-like arrangements observed in the bulk 3-HPLN crystal structure [20, 221]. The zipper-like chains attract each other on the surface to form small clusters, as shown in Fig. 4.22(a). There exists a high level of disorder in the networks, i.e. short chain segments, isolated clusters, and other defects. The chains orient themselves along the $\langle 1\bar{1}0 \rangle$ directions of the surface. It is reasonable to assume that the molecules are H-bonded, with each molecule forming a single H-bond to two different molecules along the chain length as illustrated in Fig. 4.22(b), reminiscent of the bulk crystal. The chains must attract each other through van der Waals interactions since, within the model, the chemically active hydroxyl and carbonyl groups are all participating in hydrogen bonding along the chains. Calculations performed with the DFT-D2 functional, discussed below, suggest that in clusters and networks of 3-HPLN, the intermolecular hydrogen bonding interactions are about an order of magnitude larger than dispersion.

Annealing the sample to approximately 400 K drastically changes the structure of 3-HPLN on Ag(111), with the emergence of a new ordered network. Fig. 4.23(a) shows the co-existence of a close packed phase, around the edges of the image, with an ordered porous network in the center. Note that in addition to the trimer based network, sometimes when utilizing the same sample preparation procedures we observe different ordered phases, including one with a dimer comprising the unit cell. This shows that several structural configurations of similar energy coexist, as can also be seen in Figure 4.23(a). The basic building block of the porous ordered network is a trimer of 3-HPLN, and two trimers within a rhombus represent the unit
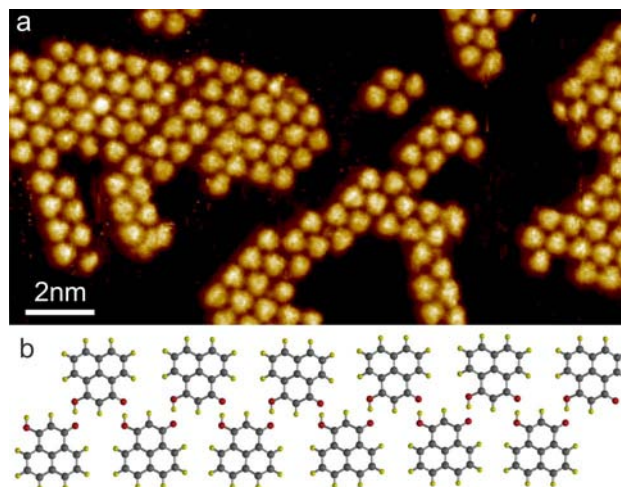
Figure 4.22: (a) STM image after room temperature deposition of 3-HPLN on Ag(111) tunneling parameters: 1 V, 400 pA. (b) Proposed structure of hydrogen bonded 3-HPLN chains.

cell of the extended network. The unit cell, highlighted in Fig. 4.23(c) by a dashed white line and illustrated in Fig. 4.23(d), has measured dimensions of 2.15   0.09 nm. By measuring the uncovered Ag(111) surface with atomic resolution, it is found that the angle the unit cell makes with the underlying 110 direction is 12.6 2.2 . These measurements correspond to a commensurate $(2\ \overline{13}\ \mathrm{x}\ 2\ \overline{13})R$ 13.9 3-HPLN/Ag(111) lattice.

Each 3-HPLN molecule within the trimer has a single H-bond with each of its two nearest neighbors. Since each carbonyl and hydroxyl group participates in a hydrogen bond within the trimer, there are no carbonyl/hydroxyl groups left to participate in hydrogen bonds between trimers. It is presumed that these networks must also be held together by van der Waals forces, similar to the chain-like room temperature phase. The extended network resembles others reported in the literature, for example those formed between perylene tetra-carboxylic di-imide (PTCDI) and melamine on a silver-terminated silicon surface or during the assembly of SubPc on Au(111) [223
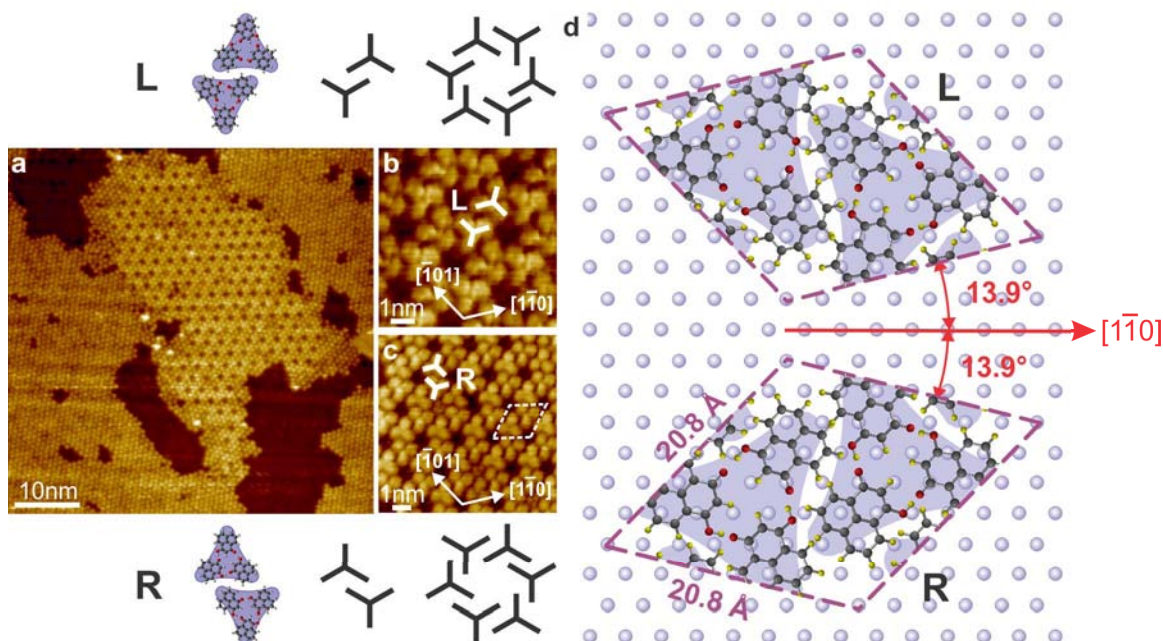
Figure 4.23: Networks of 3-HPLN on Ag(111) after annealing the sample to 400 K, followed by cooling to 77 K for STM imaging. (a) STM image highlighting the coexistence of a close packed phase and trimer network phase of 3-HPLN on Ag(111). (b, c) Examples of STM images of left and right-handed networks (enantiomorphs). The structural unit cell is highlighted by dashed lines in (c). Tunneling parameters: (a) -0.2V, 600pA (b) 0.2 V, 600pA (c) -0.2V, 500pA. (d) Bonding schematic of two trimers in a unit cell and how this leads to L (left-handed) and R (right-handed) chirality. The epitaxial orientation of the unit cell to the substrate is described as $(2 \; 13 \quad \bar{2} \; 13)R13.9^o$ in Woods notation. Also shown is how dimers of trimers assemble to form handed porous networks. Reproduced from reference [222].

227]. Remarkably, TiOPc deposited on Ag(111) was reported to form an identical commensurate lattice when deposited at a low ux [228]. Further strengthening the comparison, isolated 3-HPLN molecules are occasionally imaged in the pores of the honeycomb network. A few of these molecules can be seen by close inspection of Fig. 4.23(c). These are likely molecules that are kinetically trapped during network formation and are not commonly observed. Similar trapped molecules were found to stabilize the similar honeycomb network of TiOPc [228].

The van der Waals attraction between adjacent trimers in the porous lattice works as an effective lock and key mechanism, giving the islands long range order. Fig. 4.23(d) shows a schematic of a single 3-HPLN trimer coming together to link with an adjacent trimer via the presumably weaker van der Waals interactions thereby forming the pores of the network.

The structure of the C_{3h}–symmetry 3-HPLN trimer is reduced to C_3 symmetry upon adsorption to the Ag(111) surface (neglecting the atomic arrangement of the underlying surface atoms). As shown in Fig. 4.23(d), this allows a "handedness" (left or right) to be defined for the cluster, depending on whether the direction of the O-H$\cdots$O hydrogen bonding contacts point in a clockwise direction around the trimer's center of mass or in a counterclockwise direction. The lack of a mirror plane or glide plane of symmetry perpendicular to the surface gives the adsorbed 3-HPLN trimer local surface chirality at the point group level. Importantly, it is noted that while each pair of 3-HPLN trimers in Figure 4.23(d) is shown with only one type of trimer, i.e. each trimer within the pair has the same handedness, there is no reason why this must be the case (unless the mechanism by which they form induces it). Indeed, it is reasonable to assume that each chiral network can be made up of a random mixture of right and left-handed trimers giving rise to an overall racemic mixture. However, the asymmetric (tilted) packing of the trimers with respect to the diagonals of the unit cell ensure that the extended model networks exhibit surface chirality at the space group level, regardless of the underlying molecular orientation. Thus, the chirality of the networks is due to the offset between the trimer-trimer pairs, and their initial nucleation by the lock and key mechanism. The chirality is likely not a result of the inherent chirality of the trimers, or of the 2D-chirality of the 3-HPLN molecules themselves. However, the STM images do not reveal the handedness of individual molecules or trimers.

4.3.2   3-Hydroxyphenalenone on Au(111)

When deposited at room temperature on Au(111), 3-HPLN forms 1D hydrogen bonded chains, as in Fig. 4.24. These chains are similar to the 1D chains that compose the bulk crystal structure and also similar to the segments observed on Cu(111) at room temperature [170], where they by contrast bunch together into 2D islands. See Chapter 2 for a discussion of the crystal structure [20]. At high coverages close to 1 ML, the chains are long, often over 100 nm, see Fig. 4.24(b). Whereas at lower coverages, many short chains are observed as in (c). The chains grow over the step edges, highlighted by a green arrow in Fig. 4.24(b), which has been demonstrated for metal-organic networks previously [210].

The herringbone reconstruction of the Au(111) surface is visible below the chains of 3-HPLN, in images such as Fig. 4.24(b). From atomically resolved images of the Au(111) surface, it is determined that the chains align parallel to the $\langle 1\bar{1}0 \rangle$ directions of the underlying Au(111) surface. The intermolecular distances a and b, shown in Fig. 4.24(a) are 0.91 nm $\pm$ 0.01 nm and 0.86 nm $\pm$ 0.06 nm respectively. As was discussed in Chapter 3, the herringbone reconstruction of Au(111) results in a 5% compression of the Au atoms along the $\langle \bar{1}01 \rangle$ direction. This compression is only local, with three 120° rotational domains observed over large scales. While the Au surface templates the direction of chain growth, it is unclear, due to the experimental error, the exact epitaxial fit to the surface.
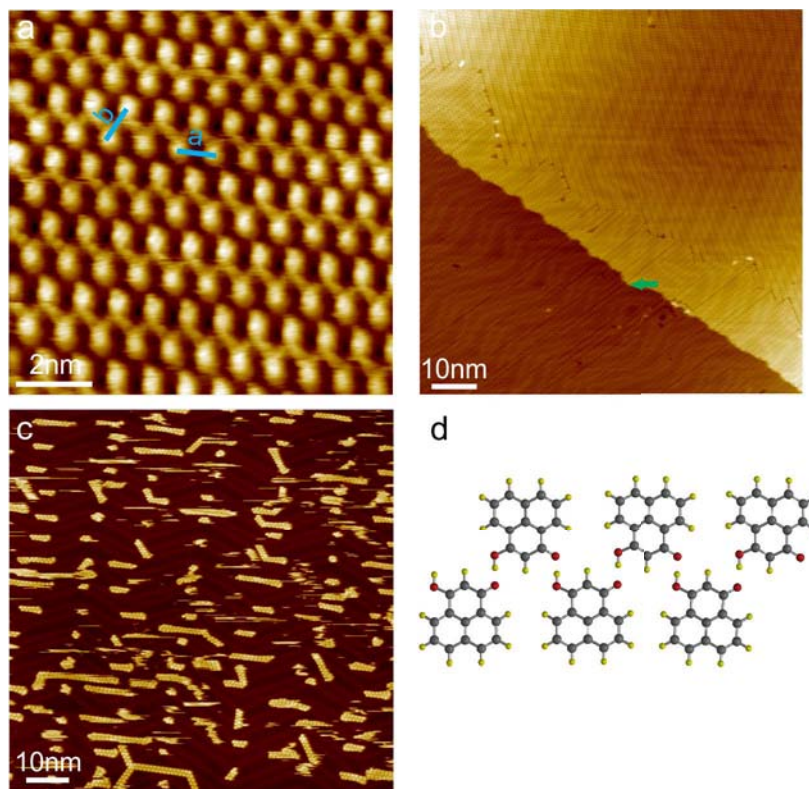
Figure 4.24: STM images of 3-HPLN on Au(111) deposited at room temperature. (a) Demonstrates bonding into 1D chains. See text for explanation of a and b. Tunneling parameters: 0.6 V, 700 pA (b) Chains are often observed to be over 100 nm long. Green arrow highlights bonding over step edge. -1.3 V, 1 nA. (c) Low coverage sample exhibiting short chains. -1.3 V, 1 nA (d) Model of hydrogen bonded chains of 3-HPLN observed on Au(111).

To conclude this chapter, for all molecules discussed, the structure observed depends on the substrate. For CA, the networks vary from porous honeycombs on Ag(111) and Au(111) to densely packed on an insulating Cu_2N bu er layer. For RA, hydrogen bonded close packed networks are observed on Au(111), whereas metal-organic coordination networks are seen on Cu(111). For 3-HPLN, extended 1D chains form on Au(111), porous honeycomb networks are seen on Ag(111), and 3D porous networks grow on Cu(111). Seemingly, the only commonality to these is that hydrogen bonds are formed, with the exception of metal coordination networks on reactive

Cu(111). In other words, there is an unsurpassed structural richness possible going from bulk to surface supported structures. Therefore, it is fair to say that the surface is a control parameter in the growth. All while the hydrogen bonds that give those materials their ferroelectric properties are preserved.

Chapter 5

Multi-Component Hydrogen Bonded Organic Structures

Driven by the weath of results from the single component structures described earlier in this thesis, I strove to study what structures emerge if two materials are combined on a single surface. Thus, this chapter describes STM investigations into multi-component hydrogen bonded organic materials. The search for ferroelectric organic co-crystals provides part of the motivation for this research and thus a brief review on this topic is provided first. Second an overview on previous surface supported organic co-crystals is given. Then, STM studies pertaining to two novel organic co-crystals are detailed. Finally, a brief overview of the 3D growth of organic co-crystals inspired by this STM work is given.

5.1 Introduction

5.1.1 3-D Ferroelectric Organic Co-crystals

With the advent of organic ferroelectrics that can compete with traditional inorganic ferroelectrics in terms of functional properties [229], the search for new functional organic materials has gained significant traction. One way to control material properties is to combine known species into multi-component co-crystals. The goal is to combine the desired properties of one molecule with those of another. Organic co-crystals have shown promise in a wide range of fields, spanning pharmaceutical research [230], explosives [231], opto-electronic devices [232], and molecular electronics [233, 234]. For example, the solubility of a drug can be improved this way in pharmaceutical co-crystals [235]. In recent years a few prototypical cases demonstrated that ferroelectric co-crystals are possible. However, they have yet to display the full range of desirable properties for applications.

Despite the great promise for co-crystals to serve as functional materials, challenges are associated with their growth. Organic compounds only rarely form co-crystals, and make up only approximately 0.5% of crystals archived in the Cambridge Structural Database as of 2009 [236]. Difficulties in finding suitable solvents for co-crystal formation has led to mechanical grinding as a preferred substitute for many compounds [237]. Moreover, the sythesis of novel co-crystals often relies on trial and error for determining the proper preparation procedure [238]. Thus, there is a need for rational design principles and new screening techniques to speed the search for novel organic co-crystals.

Ferroelectric organic co-crystals have thus far displayed three main ferroelectric switching mechanisms: displacive (including charge-transfer) [239–244], collective proton transfer [245], and order-disorder [246]. Below, I provide a brief review of

each of these classes of co-crystals.
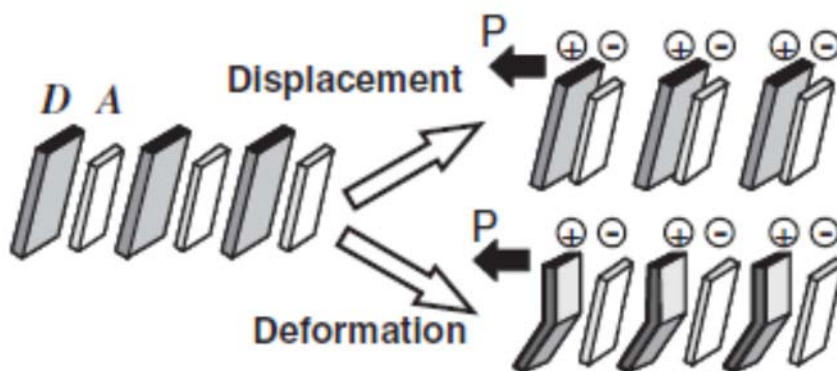
Figure 5.1: Diagram of charge-transfer type crystals. Two dimerizations are possible: displacement or deformation. Adapted from reference [245].

Charge transfer or mixed stack crystals consist of alternating donor and acceptor molecules that dimerize creating an electric polarization. The dimerization can result from either a displacement or deformation in the organics, shown in Fig. 5.1. While many charge transfer crystals are known, only a few charge transfer crystals exhibit ferroelectric switching. Notably, Tayi *et al.* discovered above room temperature ferroelectricity in three related compounds, which are shown in Fig. 5.2 [242]. These crystals were notable for being over 1 cm long and one co-crystal (**1-4** in Fig. 5.2) exhibited one of the largest known organic remenant polarizations of 55 $\frac{C}{cm^2}$, albeit at 7K. Two previous examples of mixed stack co-crystals had Curie temperatures below liquid nitrogen temperature, limiting their potential for applications [243, 244].

Three displacement type ferroelectric organic co-crystals have been reported, consisting of phenazine and chloranilic acid or bromanilic acid [240, 241] and tartaric acid and 1,4-diazabicyclo[2.2.2]octane N,N -dioxide [239]. The crystal containing tartaric acid exhibited switching at the highest known operating frequency of any organic ferroelectric (>10 kHz), but had a below room temperature Curie point (T_C=254.5K)

Figure 5.2: **1-2**, **1-3**, and **1-4** exhibit above room temperature ferroelectricity. Adapted from reference [242].

and a small spontaneous polarization ($< 1\frac{C}{cm^2}$) [239]. The crystal containing chloranilic acid also su ered from a small spontaneous polarization $<1\frac{C}{cm^2}$ at 254 K [240]. However, deuterating it led to above temperature ferroelectricity [241].

Additionally, there is one known example in which a proton transfer mechanism is responsible for ferroelectricity in an organic co-crystal, consisting of iodanilic acid and 5,5 -dimethyl-2,2 -bipyridine [245]. While the Curie temperature is below room temperature, the deuterated form has a T_C=335K. However, it has a small polarization of approximately $1\frac{C}{cm^2}$ which is an order of magnitude smaller than traditional inorganic ferroelectrics.

Finally, there is a report of an order-disorder type transition in two ferroelectric organic co-crystals consisting of TPPZ and chloranilic acid or bromanilic acid [246]. In these systems, a double proton transfer occurs. Suprisingly, the proton transfer is not responsible for the observed ferroelectric behavior here. Above T_C, four protons in the crystal are disordered, as illustrated as yellow dots in Fig. 5.3. Cooling below the Curie temperature of each co-crystal (T_C= 334K,172 K) causes one proton to localize (illustrated as a green dot) which leads to a polarization. The operating parameters of these crystals are impractical for applications, however. For example, the coercive

eld is >30 kV and could only show switching at extremely slow frequencies (20-30mHz), thereby making them unsuitable for devices.
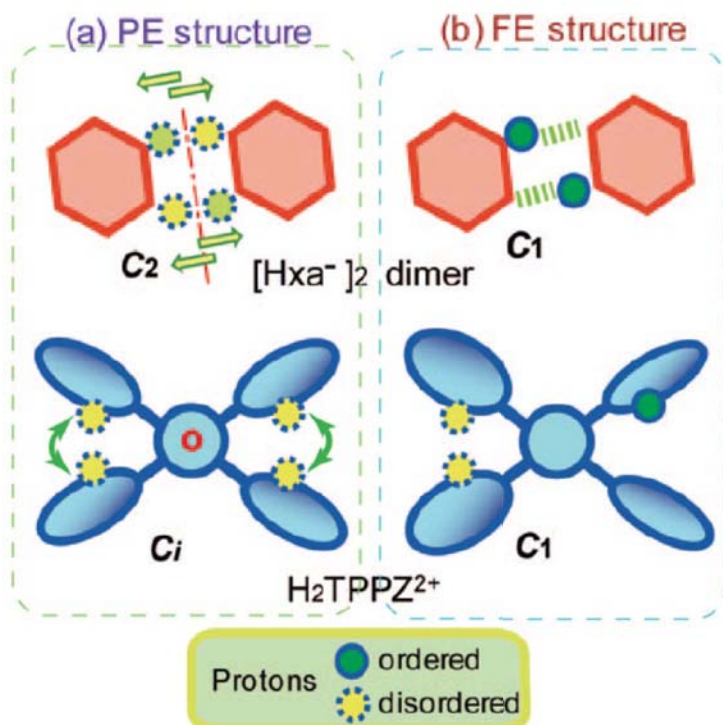
Figure 5.3: Schematic of an order-disorder type ferroelectric organic co-crystal. (a)The electrons are disordered in the paraelectric phase. (b)Only one electron localizes below the Curie temperature resulting in a polarization and leading to ferroelectricity. Reproduced from reference [246].

While there has been initial success in the synthesis of organic ferroelectric co-crystals, they have yet to rival traditional inorganic ferroelectrics in terms of operating parameters. Thus, there is a need to put signi cant e ort towards discovering new organic ferroelectric co-crystals that may one day compete with, or even replace, inorganic ferroelectric materials.

5.1.2   2D Organic Co-crystals

As was shown in Chapter 4, transitioning from bulk materials to their 2D analogs allows for an incredible diversity of novel materials as well as an additional control parameter, i.e. the substrate. This is not only true for the single component systems discussed previously, but also for mulit-component co-crystals as well. Furthermore, the study of co-crystals has provided new avenues for studying host-guest chemistry, such as the adsorption of heptamers of C_{60} into a PTCDI-melamine lattice [226]. In this thesis I propose that the study 2D co-crystals on surfaces can provide an effective route for the rapid screening of miscible compounds to form novel 3D co-crystals. This will be demonstrated for two distinct organic co-crystals.

Two-dimensional organic co-crystals were first reported in 2002 by Hipps *et al.* with the discovery of a self-assembled structure consisting of two large organics: NiTPP and $F_{16}CoPc$ [247]. Organic co-crystals have since been studied both at UHV [226, 247–260] and at the liquid-solid interface [63, 261–267].

Because of the directional nature of hydrogen bonds, they are a natural choice for use in designed self-assembled systems. As such, many of the reports on organic co-crystals have focused on hydrogen bonded systems [226, 251, 258–261, 263, 265, 266]. Other studies have reported co-crystals grown with weak van der Waals forces [249, 255, 261, 264, 267], dipole-dipole interactions [63], and even ionic bonds [257]. Combinations of these bond types in one co-cyrstal are also often observed, especially as the complexity of the co-crystal grows, as for example three component systems studied by Lei *et al.* [261].

Many different factors have been attributed to driving the structures formed during the crystal growth. The stoichiometry, or the relative ratio of molecular species in the co-crystal for instance can change its observed structure and properties. This

can include switching from disordered to ordered growth [248, 259] or the observation of different ordered phases [255, 266]. Depending on the order of deposition of the constituents, either co-crystals or phase separated systems were reported for PTCDA and melamine [253], PTCDA and CuPc [249], and C_{60} and ACA [251]. At the liquid solid interface, time of immersion was the driving factor in the observation of different phases for co-crystals of CuOEP and CoPc, as CoPc slowly replaced CuOEP resulting in the formation of different structures [262]. Finally, different network geometries are observed on different metal surfaces [259], with the crystallographic face of the metal being important in some cases [264].

5.2 STM Observations of Multi-Component Hydrogen Bonded Organics

5.2.1 3-Hydroxyphenalenone/Croconic Acid Co-crystals

In Chapter 4, it was explained that ferroelectricity occurs within the molecular plane for croconic acid (CA), 3-hydroxyphenalenone (3-HPLN), and related compounds. 2D ferroelectricity should therefore be possible in principle. It was with this motivation, that two compounds, CA and 3-HPLN were selected for co-crystallization. In particular, organic co-crystals of these compounds were examined via STM. 3-HPLN and CA by themselves form ordered, 2D hydrogen bonded structures on a range of metals, which is discussed in Chapter 4. Au(111) was selected as the substrate on which to test co-crystal growth because it is the most inert of the noble metals studied and therefore most closely mimics the gas-phase growth.

As was previously discussed, croconic acid is highly mobile at low coverages on Au(111), even at liquid nitrogen temperature. Thus, CA was first deposited onto

Au(111), and subsequently 3-HPLN was added. STM images of the as-grown lm, such as Fig. 5.4, show that the islands are fully intermixed with each island containing both CA and 3-HPLN. The molecules are easily identi ed by their shape, with 3-HPLN appearing as a large triangle, and croconic acid as a small circle. While small areas appear ordered, there is no long range order. The herringbone reconstruction of Au(111) is visible in this image both on the bare surface and below the intermixed islands. The Au(111) reconstruction remaining below the islands suggests that the interactions between the surface and adsorbates are relatively weak.
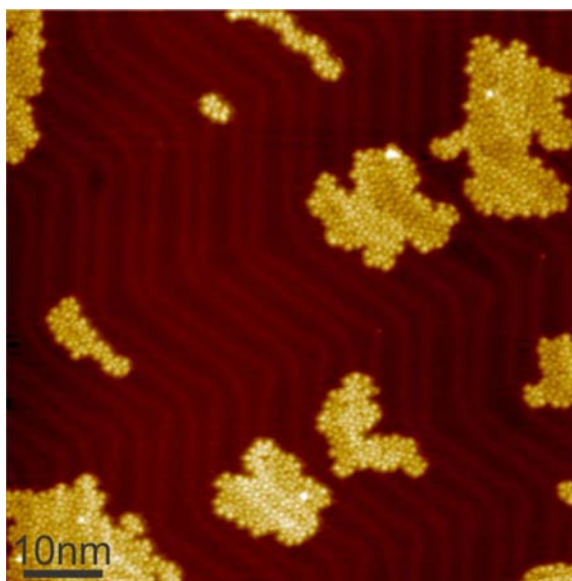
Figure 5.4: STM images of 3-HPLN and CA as grown at room temperature. CA was deposited rst, followed by 3-HPLN. Tunelling parameters: -0.5 V, 300 pA.

Next, the dependence of the co-crystal structure on the stoichiometric ratio of the components was studied. Each sample was prepared by depositing the desired ratio of CA:3-HPLN and subsequently annealing to approximately 65 C. By systematically varying the stoichiometry, three distinct ordered co-crystals are observed as shown in Fig. 5.5. With excess 3-HPLN, each CA tends to bind to ve 3-HPLN molecules, with the remaining 3-HPLN forming the same 1D hydrogen bonded chains it does

for solitary growth, as is seen in Fig. 5.5(d). For 1:1 stoichiometry, two distinct bonding patterns are observed. They are referred to as the bowtie (Fig.5.5(b)) and perpendicular (e) configurations. For CA-rich structures with composition 2:1 CA to 3-HPLN, a different bonding motif is observed, termed 2:1 and shown in Fig. 5.5(c). For samples with stoichiometries between those described above, multiple phases are observed to coexist on the same sample. However, each island consists of only a single phase.
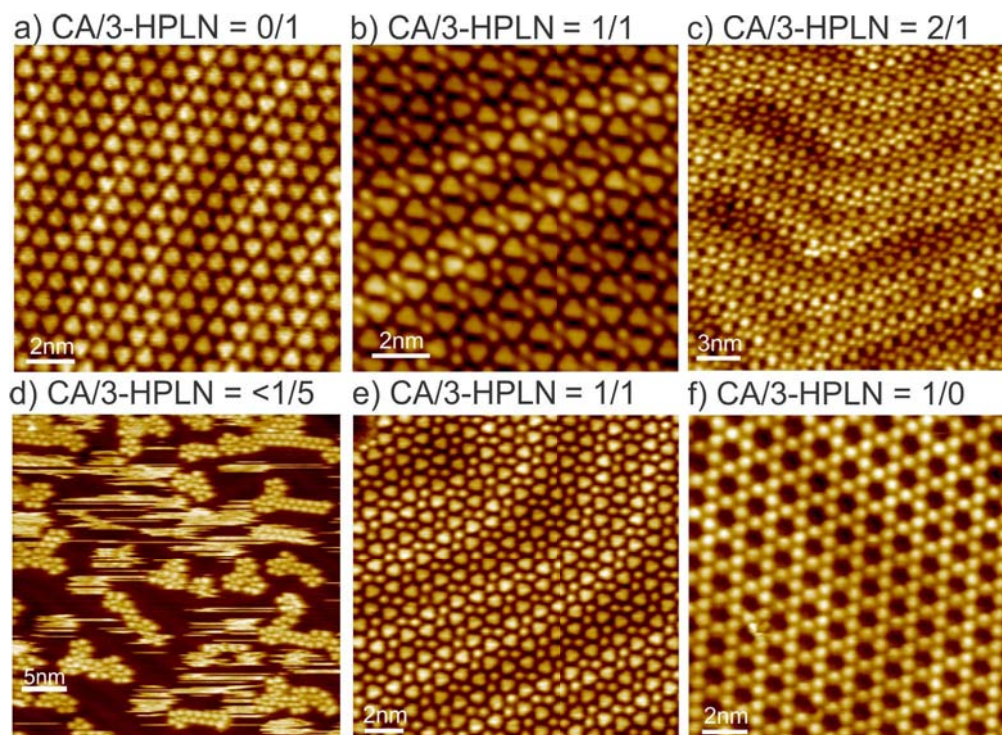
Figure 5.5: STM images demonstrating how self-assembly of CA and 3-HPLN depends on the stoichiometry of the constituents. (a) Pure CA (b) Bowtie configuration (c) 2:1 phase (d) Excess 3-HPLN (e) Perpendicular phase and (f) Pure CA.

The two observed polymorphs with CA/3-HPLN = 1/1 stoichiometry (bowtie and perpendicular) are composed of the same building block, a tetramer consisting of two molecules of CA and two molecules of 3-HPLN. A proposed structure for the tetramer, consistent with the STM images, is drawn in Fig. 5.6. Note that the way the

CA molecules hydrogen bond to each other in the tetramer is similar to the bonding observed in CA on Ag(111), discussed in Chapter 4.

Network Type	a (nm)	b (nm)
Bowtie	1.32 ± 0.04	0.61 ± 0.07
Perpendicular	1.44 ± 0.05	0.66 ± 0.04
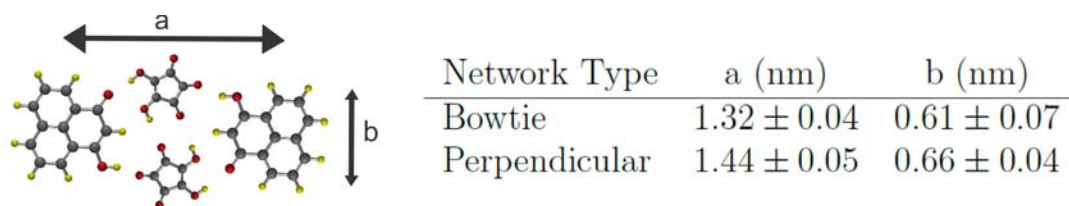
Figure 5.6: Proposed structure of CA/3-HPLN = 1/1 building block consisting of two molecules of 3-HPLN and a dimer of CA.

From examining STM images of the bowtie structure as well as the atomically resolved Au(111) surface, a bonding model can be constructed. The tetramers align such that the 101 direction bisects the tetramer along its long axis, as is shown in Fig. 5.7(a). Similarly a bonding model of the perpendicular networks is proposed in Fig. 5.7(b). In the perpendicular case, the tetramers pack perpendicularly to their neighbors. This means that the 101 direction bisects half the tetramers along their short axis and half along their long axis. In short, the key difference between the two observed 1:1 polymorphs is the relative arrangement of the $CA_2$3-$HPLN_2$ tetramers.

Note that each tetramer is held together solely by hydrogen bonds. Each tetramer can only bind to another through weak interactions such as van der Waals forces, because all the H-containing hydroxyl groups are already involved in bonds to form the tetramers. Both the bowtie and the perpendicular configurations are often seen to coexist on the same sample. Thus, it is concluded that they are of similar energy.

The measured intermolecular distances are given for the two different networks bowtie and perpendicular in Fig. 5.6. While there is not perfect agreement between the 3-HPLN to 3-HPLN separation in the bowtie and perpendicular networks, it appears in STM images that the basic building block is in fact the same
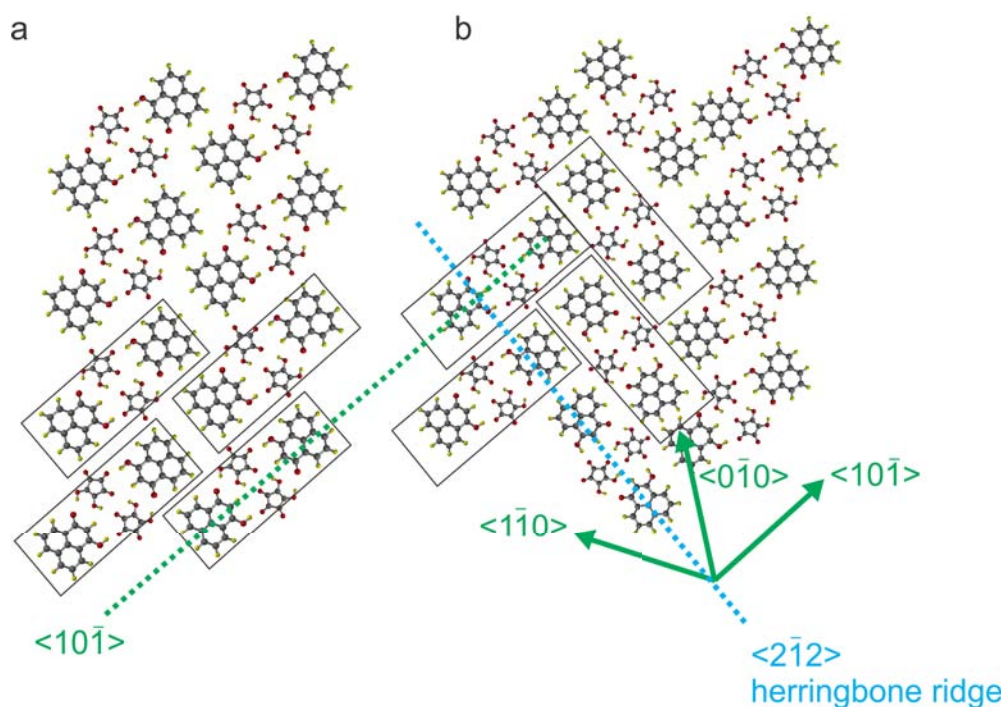
Figure 5.7: Proposed structures of the CA/3-HPLN = 1/1 networks (a) bowtie con-guration and (b) perpendicular binding.

for both networks. This is because the 3-HPLN-3-HPLN bond length may be slightly in uenced by the overall bonding pattern.

Figure 5.8(a) displays a high resolution image of the croconic acid rich CA/3-HPLN = 2/1 structure. From analyzing STM images, such as that one, a bonding model is proposed in Fig. 5.8(b) which accounts for all observations. Qualitatively, this structure appears to consist of CA_23-$HPLN_2$ tetramers and CA_2 dimers as shown. The tetramers appear to be identical to those in the CA/3-HPLN = 1/1 networks, and are highlighted with a red box in Fig. 5.8(a). Dimers of CA connect these tetramers to each other. The measured distance between croconic acid molecules in a dimer 6 4   0 4A, which is consistent with the CA/3-HPLN = 1/1 structures described above. The tetramers are oriented on Au(111) such that the 010 direction bisects the tetramers along their short axis, parallel to the CA dimers. This orientation was

also observed for half of the tetramers in the perpendicular networks.
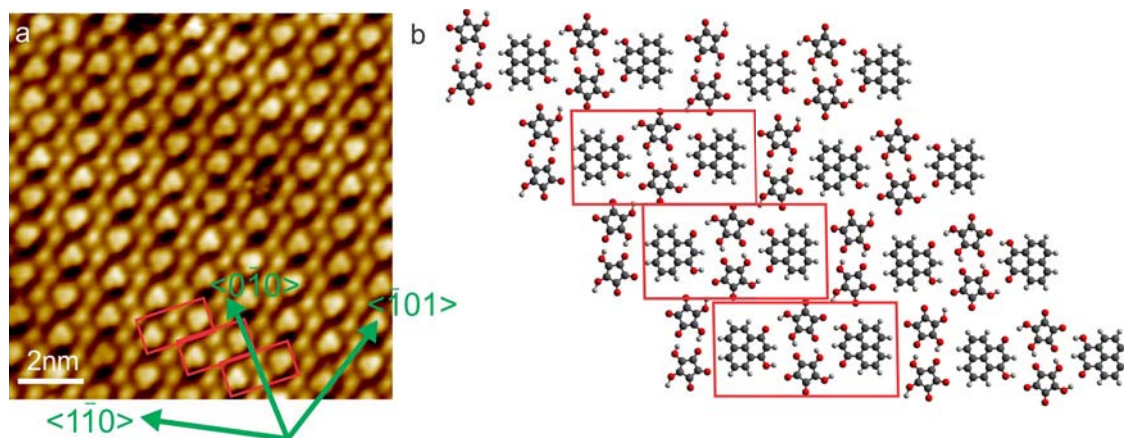
Figure 5.8: (a) STM image of CA/3-HPLN = 2/1 co-crystal. The larger triangles are 3-HPLN, whereas the smaller circles are CA. Tunneling parameters: -0.06 V,1000 pA (b) Proposed structure model based on close inspection of STM images.

In the following I will show that structural transitions from CA rich co-crystals to CA poor co-crystals can be induced by weak annealing. Starting from a CA/3-HPLN = 2/1 sample, annealing above approximately 65 C results in the selective desorption of the smaller CA molecules. This causes a transformation from the CA/3-HPLN = 2/1 structure to the 1:1 structures described above. Further annealing results in small CA poor clusters consisting of a single CA molecule surrounded by ve 3-HPLN molecules, and chains consisting of only 3-HPLN, as shown in Fig. 5.5(d).

However, the opposite transition from CA poor co-crystals to CA rich co-crystals by adding CA to a CA poor co-crystal is not possible. Starting from a prepared CA/3-HPLN = 1/1 sample, the additional deposition of CA results in a phase separation of pure CA, like in Fig. 5.5(f), and 1:1 co-crystal islands. Annealing to 65 C evaporates the CA, but does not convert it into the 2:1 structure described above. Thus, in order to form CA containing co-crystals, CA must be deposited rst.

5.2.2 Co-crystals of Parent Quinonoid Zwitterion/Croconic Acid

The co-crystallization of PZI and CA was attempted next. Again, exploiting the fact that croconic acid is gas phase at room temperature on Au(111), it was deposited prior to PZI addition. PZI were deposited in a second step at room temperature. As deposited, the molecules appeared disordered. Upon annealing to approximately 125°C, two distinct networks formed. STM images of these crystals are shown in Fig. 5.9. First note that each phase is distinct from that of single phase PZI, which forms square networks with domains (Fig. 3.7), and single phase CA, which forms porous trimer based networks (Fig. 5.5(f)). Thus, it is concluded that each of these networks is in fact the result of the combination of PZI and CA. Unlike the 3-HPLN and CA system, PZI and CA cannot be identified by their shapes in STM images due to their similar size. Similarly, no difference in apparent height was observed that may allow to distinguish between both types of molecules.

One phase was close packed, consisting of two, alternating tetramers visible in Fig. 5.9(a) and marked by red and blue rhombuses in Fig. 5.9(b). These tetramers have slightly different dimensions which are provided in Table 5.1. Whereas the second observed network was significantly more porous as is visible in Fig. 5.9(c) and (d).

The stoichiometry of the constituents was systematically varied, as was performed for the CA/3-HPLN system. However, both close packed as well as porous networks were observed on every sample prepared. When a large excess of one molecule was deposited disordered areas were also observed. Because both networks were observed on each sample, it can be concluded that they are of similar energy.

Since CA and PZI are indistinguishable in STM images, a bonding scheme cannot
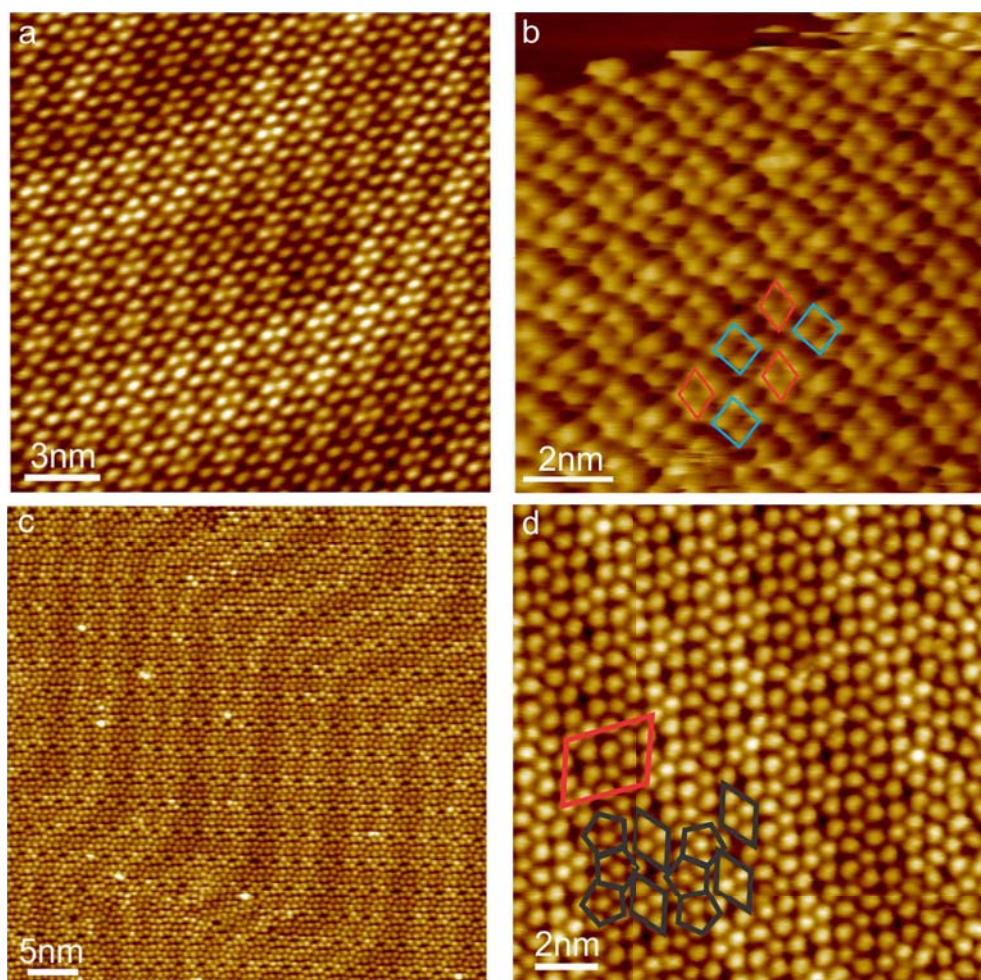
Figure 5.9: STM images of co-crystals of parent quinonoid zwitterions and croconic acid. (a) and (b) display the close packed, tetramer based network with tetramer 1 from Table 5.1 corresponding to the red rhombus and tetramer 2 the blue rhombus (c) and (d) show the porous network with alternating pentagons and tetramers composing the twelve membered unit cell, highlighted with a red box. Tunneling parameters: (a) 0.5 V, 300 pA, (b) 0.5 V, 300 pA (c) -0.5 V, 500 pA (d) -0.5 V, 500 pA.

be unambiguously established from STM images. However, some insight can be gleamed from closer examination of the networks. Tetramers were established to be the buliding block of the close packed network. While many tetramers are possible, Fig. 5.10(a) shows one possible bonding model that is consistent with STM images of the close packed co-crystals.

Table 5.1: Experimentally measured dimensions of tetramers shown in Fig. 5.9, where a is the long dimension and b is the shorter.

Network Type	a (nm)		b (nm)	
Tetramer 1	1 2	0 2	0 66	0 02
Tetramer 2	1 2	0 2	0 80	0 05

A close examination of the porous networks, from images such as Fig. 5.9(d), reveals the bonding is made of a combination of pentagons and rhomboids. Due to the pentagonal shape of croconic acid, it was assumed that these pentagons consist solely of CA, and a possible bonding scheme for the co-crystals is provided in Fig. 5.10(b). Because these pentagons are not observed if only CA is on the surface, it is concluded that PZI must act to stabilize these pentagons. This was achieved by adding a CA_2PZI_2 tetramer to the network. However, without calculations the proposed bonding models remain speculative. Nevertheless, co-crystallization of CA and PZI on surfaces was successful and will be further investigated.
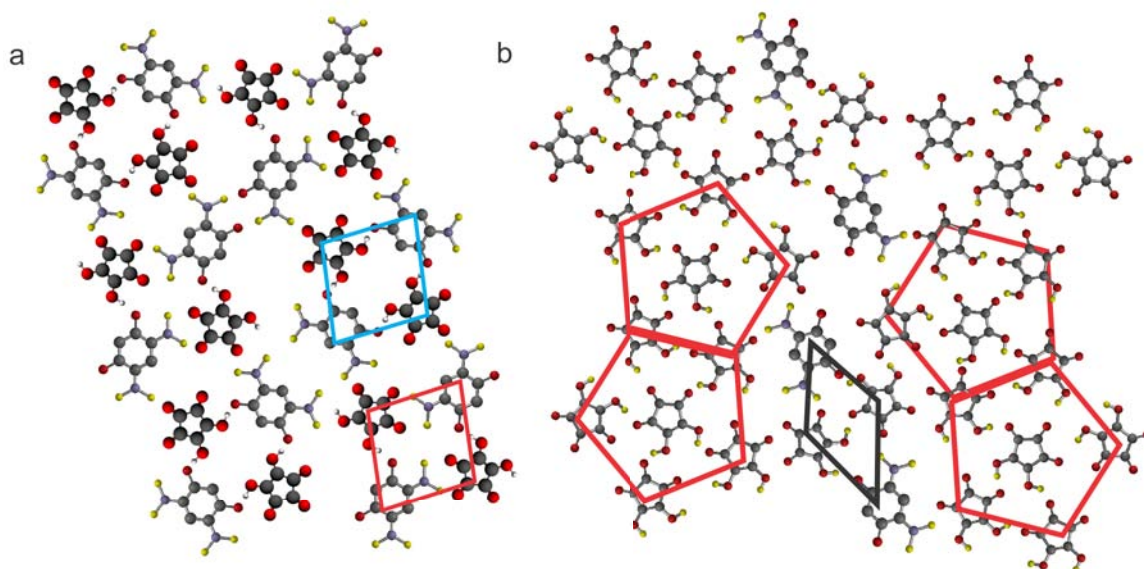
Figure 5.10: Possible bonding structures for (a) close packed co-crystal and (b) porous co-crystal consisting of PZI and CA.

5.2.3 Phase Separation in Bicomponent Organic Materials

As was discussed in the introduction, there are still significant barriers to the development of co-crystals. Computational screening methodologies for new co-crystals are only now being developed [268]. Both experimental and computational approaches are very time consuming and there remains a need for efficient screening mechanisms.

Surface science presents an interesting opportunity to predict which organic compounds are likely to form three dimensional co-crystals. By depositing two compounds on an unreactive surface, it is possible to quickly determine if the molecules favor bonding with the other species or themselves. Above, two examples of 2D co-crystal growth were examined. Using the same approach, other species were found to phase separate on a surface, from which it can be inferred that they are poor candidates for 3D crystal growth. This was determined in less than one week, whereas running computations or experimentally trying 3D growth would have likely taken considerably longer.

Rhodizonic acid has been predicted to have useful electronic properties [168], and self-assembles into regular islands at room temperature, as discussed in Chapter 4. The growth of CA and its electronic properties have likewise already been touted in this thesis. Therefore, co-crystal formation for RA and CA were tested. Similar to the examples above, both CA and RA molecules were deposited on Au(111) due to its typical weak interactions with organic adlayers. However, regardless of deposition order or post-annealing procedure, the organic species separated into islands of a single phase. Representative STM images are shown in Fig. 5.11. In these, two different networks are visible, a porous trimer network to the bottom-left and a close packed hexagonal lattice at the top-right.

While CA and RA molecules are indistinguishable in STM images, these two

networks can be di erentiated by knowledge of their single component growth. From
analyzing just CA on Au(111), and only RA on Au(111), see Chapter 4 for more
information, it is clear that Fig. 5.11 shows a phase separated sample, with CA on
the left and RA on the right. Furthermore, because the same dehydration procedures
were followed for RA on Au(111) as was discussed in Chapter 4, and the close packed
network seen here is identical to that found for pure RA, deprotonation of RA is ruled
out. From this we can infer that it is energetically favorable for CA to bind with other
CA molecules and similarly for RA to bind with RA, compared with supramolecular
bonds. Thus, we can safely exclude CA/RA co-crystals from the possibilities that are
worth pursuing.
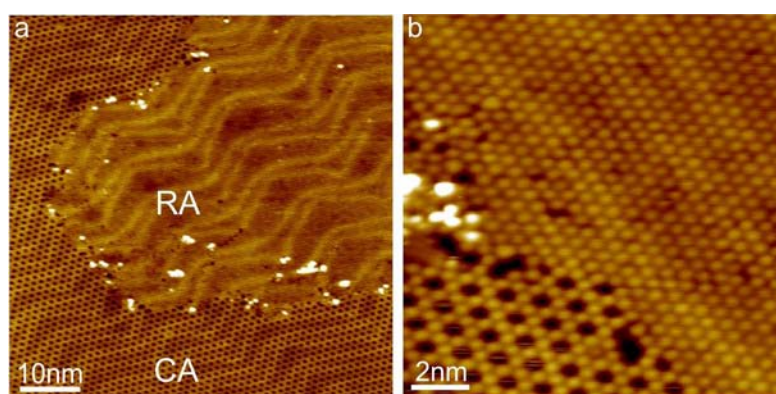
Figure 5.11: (a) STM image of croconic acid (porous network to the left) and rh-
odizonic acid (close packed network to the right). Note that there is no intermixing
between these species. Tunneling parameters: 0.6 V, 500 pA. (b) Zoom in of boundary
between CA and RA, 0.6 V, 300 pA.

STM turns out to be useful for the pre-screening of organic molecules regarding
their co-crystallization. Two combinations of organic molecules presented here were
found to readily form surface supported co-crystals, and thus are good candidates
for 3D growth. Whereas, RA and CA phase separate and can be discarded from
future co-crystallization studies. The use of STM to quickly pre-screen organics can
therefore accelerate the discovery of novel co-crystals.

5.3   3D Organic Co-crystal Growth

Guided by the STM results presented above, a collaboration with colleagues from the University of Nebraska s chemistry department, Dr. Sinitskii and Wayz Kahn, was formed to pursue the 3D growth of two sets of co-crystals. Grown through solution based chemistry, 3-HPLN and CA were found to readily form square shaped co-crystals. Photographs of the co-crystals are presented in Fig. 5.12. While the experimental determination of their exact crystal structure, as well as their electronic properties is still underway, it has been determined through initial Raman spectroscopy results that the crystals are in fact co-crystals of the components.
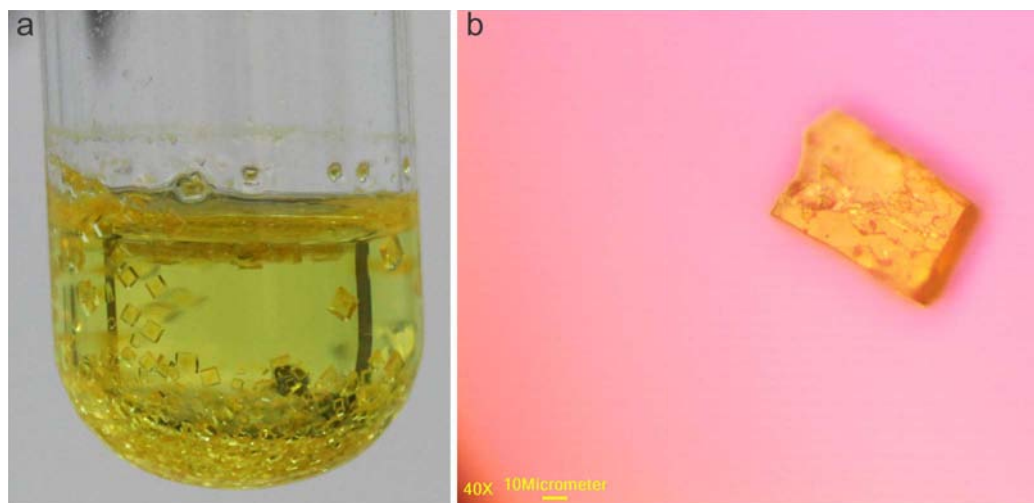
Figure 5.12: Photographs of co-crystals of 3-HPLN and croconic acid. (b) Zoomed in photograph taken under an optical microscope.

Other 3D co-crystals containing parent quinonoid zwitterions (PZI) and CA were grown, see Fig. 5.13. Two di erent crystal structures were observed one which has a square shape and one which is long and needle like. Both of these are visible in the photograph in Fig. 5.13(a). An optical microscope was used to image the needle like structure, shown in Fig. 5.13(b,c). These crystals both di er from single crystals

of PZI and CA in color and shape. Also here, determination of their structure and electronic properties is still an active pursuit.
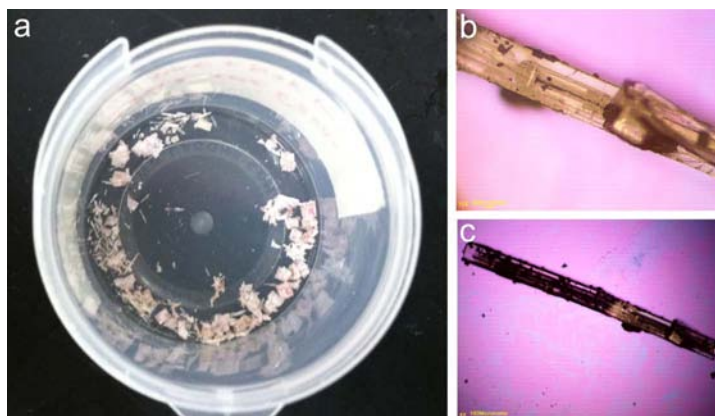
Figure 5.13: Photographs of co-crystals of parent quinonoid zwitterions and croconic acid. Images with (b) 10 x and (c) 4 x magni cation taken under an optical microscope.

In summary, scanning tunneling microscopy experiments explored two di erent hydrogen bonded co-crystals. For 3-HPLN and CA, due to the potentially switchable nature of the hydrogen bonds forming these crystals, 2D proton transfer type ferroelectricity remains an open possibility. Furthermore, the observed phases of crystal growth could be controlled by modifying the relative ratios of deposited organics. 3D analogs of each of the co-crystals were successfully grown, demonstrating the use of surface science as an e ective screening tool for co-crystal growth.

Chapter 6

Magic Organic Surface Clusters

6.1   Introduction

In the course of studying the self-assembled organic networks described in Chapters 3-5, small organic clusters containing less than 10 molecules were often observed. For each system, one particular cluster size and geometry was predominantly seen. In cluster physics, the term "magic clusters" has been established for those clusters of particularly high abundance in experiments, due to their exceptionally high stability. This phenomena of "magic" clusters that are especially stable has been actively studied for atoms in the gas phase, but it is relatively unexamined for organic clusters on surfaces. This chapter will provide a brief background on magic clusters, and present experimental observations of novel surface supported organic clusters. It is the goal of this chapter to bring attention to this topic as one that is worthy of further study.

In the gas phase, magic clusters typically form due to geometric considerations [269,270], electronic shell filling [214], or occasionally minima in the Gibbs free energy [271]. Geometric considerations, in which certain shapes of 3D clusters are more stable than others, can easily translate to certain 2D organic systems. However,

there are some complicating factors on a surface. In the gas phase only molecule-molecule interactions exist. Whereas on a surface, molecule-surface interactions can be significant, as was discussed in Chapter 2, so that the concept does not necessarily apply to surface-supported clusters. Secondly, organic species with certain functional groups may participate in directional covalent or hydrogen bonds. These directional bonds will influence the shape and possibly the size of the clusters, adding more complexity than gas phase atomic systems.

Electronic shell filling arguments do not translate as readily to 2D organic systems. In a 2D organic cluster, large molecular orbitals that encompass all organic molecules in the cluster do not form, in general. However, these molecular orbitals are the "shell" that is required for electronic shell filling. Additionally, fractional charge is often transferred between the surface and organic adsorbate, as was discussed in Chapter 2. This fractional charge limits the applicability of electronic shell filling ideas.

Nevertheless, magic clusters are observed experimentally with Fig. 6.1 displaying a selection from the literature, and the mechanisms that cause their formation are many and much discussed. For instance, charge transfer [76, 78, 272, 273] and surface epitaxial fit [274] have been suggested. In the case of an epitaxial mismatch between the organic and surface, strain bulids up across the cluster, potentially limiting its size. Additionally, cluster size has been found to depend on the coverage [275] and functional end groups [275–277]. Also, clusters often only exist at low molecular coverages, condensing into 1D [273, 278] or 2D [46, 277, 278] networks at increased molecular density. The details of bond formation, such as bond angle may also play a role.

In general, these clusters can be understood to form due to a combination of attractive and repulsive forces. For example, 4-fluorostyrene aquires a charge through sur-

face interactions leading to Coulombic repulsion between the molecules, see Fig.6.1(j) [76]. This repulsion is partially balanced by attractive van der Waals forces. Depending on the surface, the amount of charge aquired by each molecule differs, leading to different magic cluster sizes on different surfaces. It is this balancing of attractive and repulsive forces that leads to a particular size and geometry being relatively stable.

A variety of organic molecule sizes have been studied ranging from methanol [279] to large TPP derivatives [275, 277, 278]. Similarly, many different types of chemical bonds have been observed in the bonding of magic clusters, including metal-organic [275], hydrogen [76, 273, 276, 277], CH-π [274], dipolar [78, 278], Coulombic [46] and van der Waals [76, 272, 278]. A sample of STM images demonstrating the wide variety of observed clusters is shown in Fig. 6.1.

Chirality is nearly always present in surface supported organic magic clusters. For example, Lawton *et. al* were able to switch the chirality of self-assembled hexamers of methanol by performing voltage pulses near clusters [279]. In a particularly beautiful example, Blüm *et. al* observed three nested levels of enantiopure chiral species, as shown in Fig. 6.1(a) [280].

As of now, there does not exist a set of rules that explain the stabilty of small organic clusters on surfaces, in general. Thus, additional studies on magic organic clusters are encouraged, which will enable more general conclusions about the principles that govern organic cluster growth on surfaces.
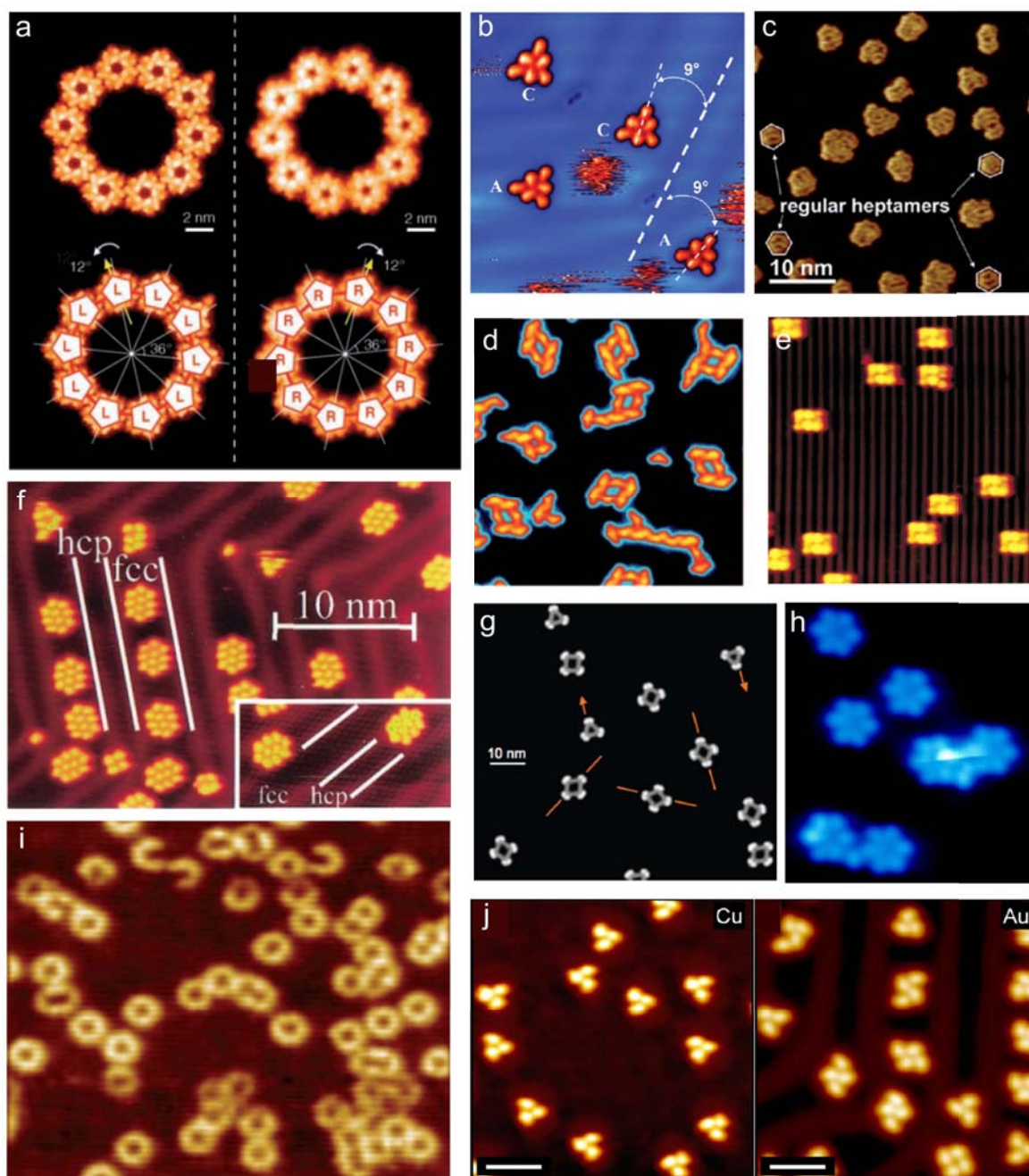
Figure 6.1: Gallery of examples of magic organic clusters as reported in the literature. STM images are of the following molecules: (a) rubrene [280] (b) phenylacetylene [274] (c) borazine [272] (d) Co(5,5 -Cl$_2$-Salen) [46] (e) cysteine [281] (f)1-nitronaphthalene [273] (g) disubstitued pyridylporphyrin [275] (h) methanol [279] (i) styrene [78] (j) 4- uorostyrene [76]

6.2 Observations of Organic Surface Clusters

In the course of studying the organic networks previously discussed in this thesis, a number of novel magic organic clusters were observed. These include both metal-organic clusters and hydrogen bonded clusters. They were observed on Ag(111) and Cu(111) and are presented here.

6.2.1 Quinonoid Zwitterion Magic Clusters

While studying the 2D and 1D growth of quinonoid zwitterions (QZI), see Chapter 3, magic organic clusters were routinely observed on Ag(111). However, these clusters were not disscussed until now. Three different species of QZI were studied with varying substituent end groups. Parent zwitterions form a variety of magic clusters when deposited at room temperature. Four membered clusters and seven-membered hexagonal clusters are routinely observed, as well as a variety of clusters with missing molecules or extra molecules. A typical STM image showing the array of clusters observed is shown in Fig. 6.2(a). However, ethyl and butyl zwitterions only form four membered clusters, as shown in Fig. 6.2(b) and (c) respectively.

By comparing the shape of these molecules in STM images, with those found for extended networks such as in Fig. 3.13(a), the orientation of the molecules within the clusters is determined. Each molecule in a cluster is oriented with the O end of the molecule pointing toward the center of the cluster. This is true for all QZI: parent, and functionalized with ethyl and butyl.

Close inspection of the tetramer clusters shows that the molecules are offset slightly from a perfect square, as is highlighted by green lines in Fig. 6.2(c). A bonding schematic that reproduces the appearance and chirality of the cluster in the STM image is proposed in Fig. 6.3. In this model of the BZI, each molecule forms
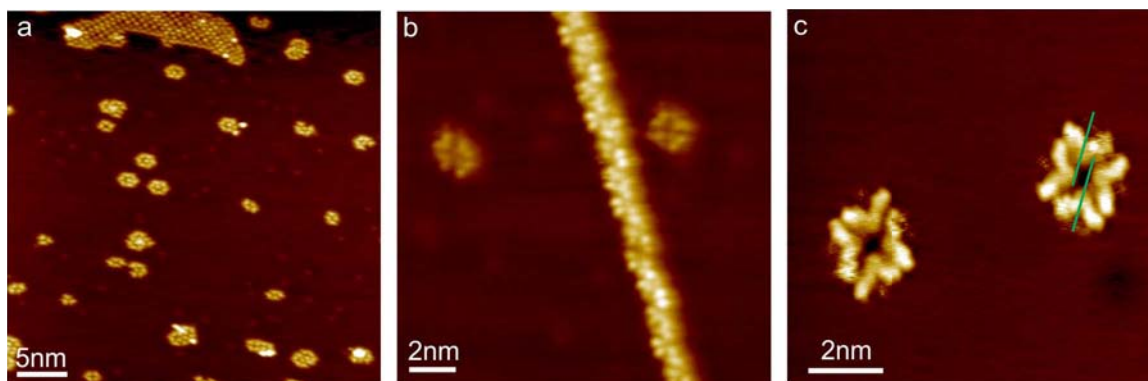
Figure 6.2: Magic organic clusters of quinonoid zwitterions on Ag(111) as grown at room temperature. (a) Parent zwitterions form clusters of primarily four or seven molecules. However, many clusters have defects, and a few other cluster sizes are observed. (b) Ethyl zwitterions form magic clusters of four molecules. An H-bonded chain is visible in the center. (c) Butyl zwitterions form four-membered clusters. Green lines highlight the o set of molecules across a tetramer. Tunneling parameters: (a) -0.7 V, 400 pA (b) -0.3 V, 350 pA (c) 0.3 V, 700 pA.

hydrogen bonds with two neighbors using carboxyl and amine groups, and the alkane chains are close, maximizing van der Waals forces.
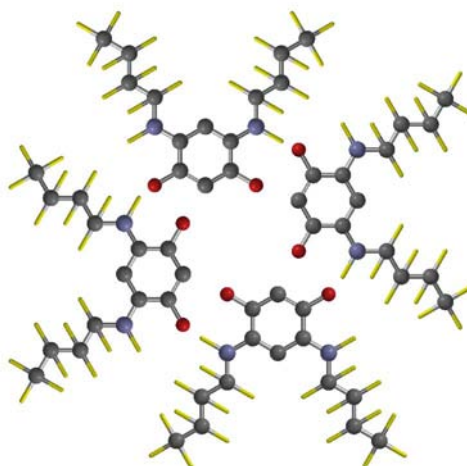
Figure 6.3: Bonding schematic for magic clusters of butyl zwitterions. The same bonding applies for the ethyl and parent zwitterions as well.

A pressing question is why is four the magic cluster size for the butyl and ethyl zwitterions. We speculate that adding more molecules in a similar fashion results in

closer packing of the alkane tails, which would increase the Pauli repulsion between the tails. Thus, the alkane-alkane distance that results from four molecules is likely an energetic minimum. Note that for all cases of QZI, charging effects are excluded, since we also observe extended 1D or 2D architectures, as described in Chapter 3.

The variety of cluster sizes for PZI compared with ethyl and butyl zwitterions can be explained by the absence of substituents. Because the PZI lack bulky alkanes, and alkane-alkane repulsion was the primary reason for the four-membered clusters, it is consistant that PZI would be free to form many different cluster sizes. The number of members in these clusters and the overall appearance must be the result of maximizing the number of bonds, balance between attractive (hydrogen bonds and Van der Waals forces) and repulsive (Pauli repulsion) forces and the bond angle of the hydrogen bond. Also note that the eptaxial relation between the clusters and the surface influences the growth of the clusters, as can be seen by the PZI tetramers only adopting three distinct rotational orientations with respect to the Ag(111) surface. Obviously, the factors driving magic clusters on surfaces are quite different than those established for gas phase clusters.

6.2.2   Croconic Acid Magic Clusters

In studying the honeycomb network that croconic acid (CA) forms on Ag(111), see Chapter 4, small clusters of CA were routinely observed, but were ignored in the discussion of this system. When deposited at room temperature, stable six-membered clusters form, which were mentioned in Fig. 4.4(a). Nearly without exception, the only cluster size observed is the hexamer. A representative STM image is shown in Fig. 6.4, similar to Fig. 4.4(a). Similar to the honeycomb networks, the buliding block of these hexamers is a dimer of CA. No isolated dimers were observed, however. The

dimers of CA contain two unpaired hydroxyl groups, making them eligible to form hydrogen bonds with other dimers and thus explaining the lack of isolated dimers. The question of why dimers and not a dierent unit, such as trimers of CA, are particularly stable on Ag(111) remains an open question.

As discussed in Chapter 4, two dierent monomers of CA are possible upon adsorption, one of which is chiral. Each of these monomers is capable of bonding to form a hexamer, both of which are displayed in Fig. 6.4(b). Due to the extreme similarity of these two clusters it cannot be determined which one is experimentally observed. This is much dierent than the case of extended networks of croconic acid. In that case, the dierent monomers resulted in large scale dierences to the geometry of the extended networks. Note that here the clusters obtain their chirality not from the individual molecules, but instead from the way in which they assemble.
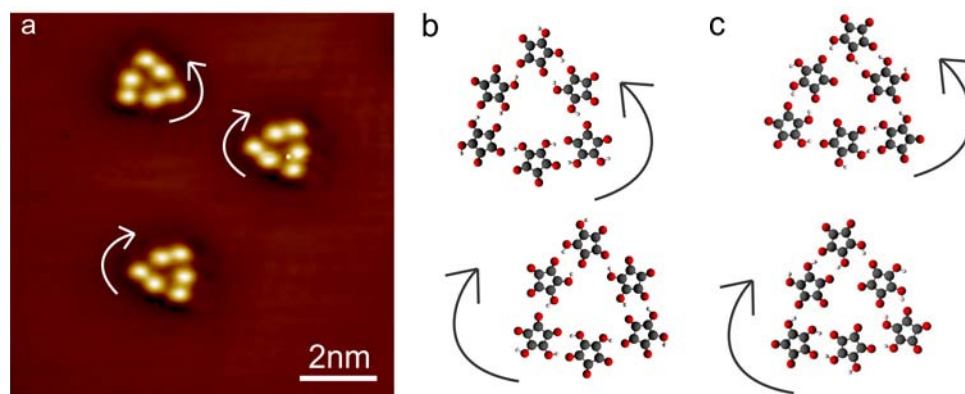
Figure 6.4: (a) STM image of magic clusters of croconic acid on Ag(111) as deposited at room temperature. Arrows indicate chirality of clusters. Tunneling parameters: -1 V, 500 pA (b) and (c) possible bonding models of CA in which (b) is composed of achiral CA molecules and (c) chiral CA molecules due to the location of the hydroxyl groups.

After annealing the sample, these clusters disappear and the molecules join the extended honeycomb networks described in Chapter 4. This implies that the clusters

are not the most energetically favorable state for CA and the term "magic" might be a stretch. Nevertheless, if isolated clusters of CA are observed on Ag(111), then those are nearly always traingular hexamers, also trimers of dimesrs. The relative stability of the networks is likely due, at least in part, to the number of hydrogen bonds per molecule. In the extended networks each CA molecule has four hydrogen bonds per molecule, but the CA in clusters only has three hydrogen bonds per molecule. One hypothesis is that these clusters form at room temperature instead of the extended networks because of the relatively high diffusion barrier CA experiences on Ag, i.e. the mean free path of CA at room temperature is too short to allow for the growth of large networks.

Again the question arises as to why six-membered clusters are favored over other possible cluster sizes. We could easily envision clusters containing four dimers, but these were nearly never observed. Because the molecules form extended 2D networks, charging effects may safely be excluded.

One hypothesis again is that the bond angle is the driving factor. The dimer has hydrogen bond angles of approximately $180°$, from which it can be inferred that this angle is particularly favorable. The hexamers also exhibit a bond angle of nearly $180°$, as is highlighted by a green dashed line in Fig. 6.5(a). However, an eight membered cluster can easily be constructed which has a similar bond angle, shown in Fig. 6.5(b). Further studies are required to solve this question of the stability of CA clusters.

6.2.3   Rhodizonate/Cu Magic Clusters

Rhodizonic acid deprotonates on Cu(111) when annealed to approximately 360 K, and forms metal organic coordination networks (MOCN) which were discussed in Chapter 4. In addition to the extended 2D networks, isolated clusters are also observed to
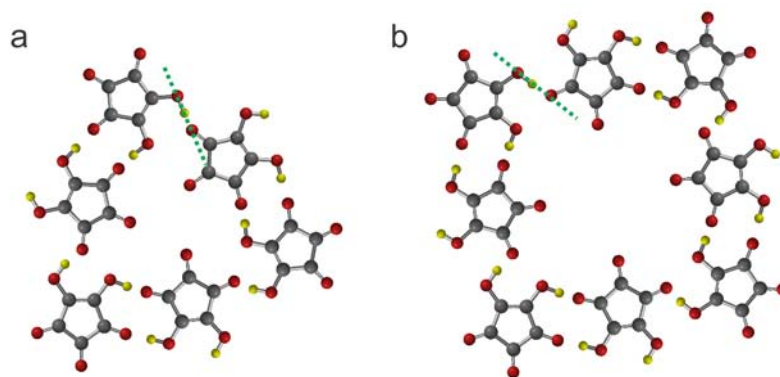
Figure 6.5: (a) Model of CA hexamers as observed on Ag(111). Bond angle of nearly 180 between dimers is highlighted with a green dashed line. (b) Hypothetical eight membered cluster with a similar bond angle.

coexist on the same sample. With virtually no exceptions, only single clusters, visible at the top of Fig. 6.6(a), or combinations of three such clusters (bottom of Fig. 6.6(a)) were observed. We have shown by DFT calculations in Section 4.2 that these clusters consist of a central rhodizonate molecule, surrounded by six Cu adatoms and six other rhodizonate molecules. A bonding schematic is provided in Fig. 6.6(b).
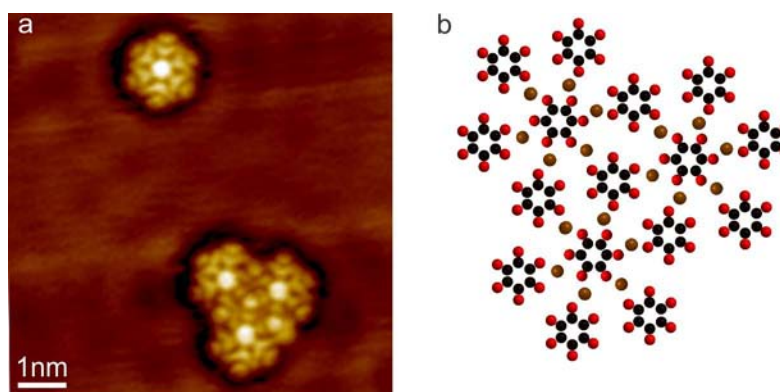
Figure 6.6: (a) Two magic clusters consisting of rhodizonate and Cu atoms imaged on Cu(111) Tunneling paramters: 0.08 V, 250 pA. (b) Bonding scheme of magic cluster composed of three single clusters. Similar to extended networks discussed in Chapter 4, a mixture of 6-fold and 3-fold Cu coordination is observed.

Also here the question is why these clusters consisting of seven molecules are

particularly stable. Why do we never observe an added rhodizonate or Cu atom? Charging effects cannot be the cause of rhodizonate/Cu cluster formation, because the exact same bonding is oberseved for the 2D extended islands, and charging would prevent the formation of extended networks, similar to the QZI and CA systems discussed previously.

For this rhodizonate system, the molecules are commensurate with the surface, see Chapter 4 for details. Further, the commensurability extends through extended networks without any obvious signs of strain on the system. Therefore, epitaxy can likewise be excluded from the possibilities of the stability of these cluster sizes.

When rhodizonic acid deprotonates into rhodizonate, it becomes hexagonally symmetric. Also, by doing so it likely loses its electric dipole moment. Thus dipolar interactions can also be ruled out as the source of the stability of these clusters. Geometric considerations, as discussed in Section 6.1, are a likely candidate. The hexagonal shape of the clusters may maximize the attractive forces, resulting a a particularly stable unit.

In conclusion, the field of gas phase cluster physics is not directly applicable to surface systems without major modifications. Certain organic systems, such as the BZI shown above, form clusters in which all bond attachment points, such as carboxyl groups, are involved and no further attachment points exist. Do these clusters also qualify as "magic"? While that is an open question, these clusters are certainly different than any encountered in gas phase cluster physics. For most of the systems shown here, we do not understand why these particular sizes are exculsively observed. Epitaxy, charging, and other such ideas were ruled out as the cause of these clusters. While this chapter is very inconclusive, these results are provided here in the interest of furthering the discussion of surface supported organic clusters.

Chapter 7

Concluding Remarks

This thesis provides a compelling examination of polarization phenomena in 2D organic nanostructures. Two distinct classes of organic molecules were considered: quinonoid zwitterions which possess an intrinsic dipole moment of nearly 10 D and organic species, such as croconic acid, which aquire a switchable dipole moment through intermolecular bonding. Scanning tunneling microscopy was used to examine these species in real space, with sub-molecular resolution.

Quinonoid zwitterion self-assembly can be switched from networks with zero net polarization to networks with a net dipole moment by modifying either the substituent end group or by changing the substrate. Frontier orbital overlap with the Fermi level of Au(111), Ag(111), or Cu(111) causes significant charge rearrangement on all surfaces, resulting in a nearly 9 Debye decrease in the dipole moment, and a change in orientation of the dipole moment from in the plane of the molecule to nearly perpendicular to it. Within this comprehensive, comparitive study using strongly dipolar species, I found no evidence showing that the electrostatic energy minimization drives or dominates the self-assembly. Instead, the self-assembly is the result of several competing mechanisms. Hydrogen bonding, which is seen in all quinonoid

zwitterion systems studied, is highly important with intermolecular bonding energies above 700 meV for certain cases. Secondary effects that determine the observed structures include site selective dependence, which is on the order of 40 meV for PZI on Au(111), and is possibly higher in other cases. Both attractive and repulsive dipolar forces compete with much smaller energies of <5 meV. It is this complex, hierarchical interplay of forces that when combined, determine network stability and also the relative molecular alignments.

Three organic species that either exhibit proton transfer type ferroelectricity (croconic acid (CA) and 3-hydroxyphenalenone (3-HPLN)) or are predicted to display ferroelectricity (rhodizonic acid (RA)) are examined on Cu(111), Ag(111), Au(111), and an insulating Cu_2N buffer layer. The structure observed depends heavily on the substrate. For CA, the networks vary from porous honeycombs on Au(111) and Ag(111) to close-packed chains on Cu_2N. For RA, densely packed hydrogen bonded networks are observed on Au(111), whereas metal organic coordination networks are seen on Cu(111). For 3-HPLN, extended 1D chains form on Au(111), porous honeycomb networks are seen on Ag(111), and 3D porous networks grow on Cu(111). Seemingly, the only commonality to these is that hydrogen bonds are formed, as long as substrate metal atoms are not involved in the self-assembly. In other words, there is an unsurpassed structural richness possible going from bulk to surface supported structures. The surface can be viewed as a control parameter, through which surface interactions, such as switchable hydrogen bonds, may be optimized. It turns out that the substrate is of critical importance for the polarization of the organic adlayer: on Ag(111) the switching barrier to proton transfer is considerably lowered as compared to the free organic structure. This opens the possibility of optimizing surface/organic interactions to create a true 2D organic ferroelectric.

Scanning tunneling microscopy is shown to be an original and efficient route for

screening the miscibility of organic compounds. This method directly led to the discovery of two novel 3D organic co-crystals, as well as the surface supported analogs. Of note, 3-HPLN and croconic acid form stoichiometry dependent, hydrogen bonded co-crystals on Au(111). Additionally, parent quinonoid zwitterions and croconic acid are found to be highly miscible on the Au(111) surface, and likewise form bulk co-crystals.

Finally, this thesis pioneers the subject of 2D magic organic clusters as one worthy of pursuit. The few reports of 2D magic organic clusters remain isolated in the literature, and there has not been a comprehensive discussion of this topic. Five new magic organic clusters are reported here, which add significantly to the known 2D magic organic clusters.

The key findings of this thesis can be summarized as follows:

- The demonstration that the growth of highly dipolar organic molecules can be switched from polarized to non-polarized structures by utilizing different substrates.

- Ascertaining that dipole-dipole energy minimization is not the primary driver of self-assembly of highly dipolar organic molecules.

- The discovery of chiral honeycomb networks of croconic acid, in which the interaction with the substrate is key to ferroelectric switching barriers.

- Determining that resonance assisted hydrogen bonds can exist in a metal supported organic system.

- The first synthesis of rhodizonic acid crystalline structures by dehydration of the strongly hygroscopic substance in ultra-high vacuum.

- The identification of a new, chiral phase of hydrogen-bonded trimers of 3-HPLN.

- The discovery of novel organic co-crystals, both 2D and 3D, of croconic acid and 3-HPLN.

- Pioneering the concept of surface supported magic organic clusters.

The scientific findings presented in this thesis, inspire a number of new questions and topics for future research. These include: How can one measure experimentally an in-plane polarization at the molecular scale? In-plane polarizations cannot be measured with an STM. While piezoforce response microscopy can measure both in-plane and out of plane polarizations, it has not yet achieved the sub-nanometer resolution that is necessary for detecting molecular polarizations. Additionally, which metal/organic interface is optimal for proton transfer in ferroelectric hydrogen bonded systems? How should organic ferroelectrics be integrated into current data storage devices? Should entirely new paradigms be constructed, or should work towards integration with current circuitry be a priority? What is actually driving the growth and stability of magic organic clusters? Can more general design rules be determined such that clusters can be predicted, or at least explained more fully? With the wealth of possibilities, the study of polarized organic nanostructures is seen as an emergent area of research which will potentially stimulate and enable new types of applications in the future.

Bibliography

[1]   N. Koch, N. Ueno, and A. T. S. Wee. *The Molecule-Metal Interface.* Wiley.
       com (2013).

[2]   S.M. Goetz, C.M. Erlen, H. Grothe, B. Wolf, P. Lugli, and G. Scarpa, Organic
       Field-Effect Transistors for Biosensing Applications, Org. Electron. **10**(4), 573–
       580 (2009).

[3]   J.C. Blakesley, P.E. Keivanidis, M. Campoy-Quiles, C.R. Newman, Y. Jin,
       R. Speller, H. Sirringhaus, N.C. Greenham, J. Nelson, and P. Stavrinou, Or-
       ganic Semiconductor Devices for X-ray Imaging, Nucl. Instrum. Methods Phys.
       Res., Sect. A **580**(1), 774–777 (2007).

[4]   C. R Newman, H. Sirringhaus, J. C. Blakesley, and R. Speller, Stability of
       Polymeric Thin Film Transistors for X-ray Imaging Applications, App. Phys.
       Lett. **91**(14), 142105–142105 (2007).

[5]   R. C. G. Naber, K. Asadi, P. W. M. Blom, D. M. de Leeuw, and B. de Boer,
       Organic Nonvolatile Memory Devices Based on Ferroelectricity, Adv. Mater.
       22(9), 933–945 (2010).

[6]   B. Choi, J. Rhee, and H. H. Lee, Tailoring of Self-Assembled Monolayer for
       Polymer Light-Emitting Diodes, Appl. Phys. Lett. **79**(13), 2109–2111 (2001).

[7]   M. Fahlman, M. Lögdlund, S. Stafström, W. R. Salaneck, R. H. Friend, P. L.
       Burn, A. B. Holmes, K. Kaeriyama, Y. Sonoda, F. Meyers, and *et al.*, Ex-
       perimental and Theoretical Studies of the Electronic Structure of Poly (p-
       phenylenevinylene) and Some Ring-Substituted Derivatives, Macromolecules
       28(6), 1959–1965 (1995).

[8]   M. Fahlman, D. D. Gebler, N. Piskun, T. M. Swager, and A. J. Epstein, Experi-
       mental and Theoretical Study of Ring Substituent Induced Effects on the Struc-
       tural and Optical Properties of Poly (p-pyridylvinylene-phenylenevinelyne)s, J.
       Chem. Phys. **109**, 2031 (1998).

[9]   G. Heimel, L. Romaner, J.-L. Brédas, and E. Zojer, Interface Energetics and
       Level Alignment at Covalent Metal-Molecule Junctions: π-Conjugated Thiols
       on Gold, Phys. Rev. Lett. **96**(19), 196806 (2006).

[10] H. Ishii, K. Sugiyama, E. Ito, and K. Seki, Energy Level Alignment and Interfacial Electronic Structures at Organic/Metal and Organic/Organic Interfaces, Adv. Mater. **11**(8), 605–625 (1999).

[11] S. Kobayashi, T. Nishikawa, T. Takenobu, S. Mori, T. Shimoda, T. Mitani, H. Shimotani, N. Yoshimoto, S. Ogawa, and Y. Iwasa, Control of Carrier Density by Self-Assembled Monolayers in Organic Field-Effect Transistors, Nature Mater. **3**(5), 317–322 (2004).

[12] L. Romaner, G. Heimel, J.-L. Brédas, A. Gerlach, F. Schreiber, R. L. Johnson, J. Zegenhagen, S. Duhm, N. Koch, and E. Zojer, Impact of Bidirectional Charge Transfer and Molecular Distortions on the Electronic Structure of a Metal-Organic Interface, Phys. Rev. Lett. **99**(25), 256801 (2007).

[13] I. Carmeli, G. Leitus, R. Naaman, S. Reich, and Z. Vager, Magnetism Induced by the Organization of Self-Assembled Monolayers, J. Chem. Phys. **118**, 10372 (2003).

[14] T. Van Woudenbergh, P. W. M. Blom, M. C. J. M. Vissenberg, and J. N. Huiberts, Temperature Dependence of the Charge Injection in Poly-dialkoxy-p-phenylene Vinylene, App. Phys. Lett. **79**(11), 1697–1699 (2001).

[15] T. van Woudenbergh, P.W.M. Blom, and J.N. Huiberts, Electro-Optical Properties of a Polymer Light-Emitting Diode with an Injection-Limited Hole Contact, Appl. Phys. Lett. **82**(6), 985–987 (2003).

[16] F. So. *Organic Electronics: Materials, Processing, Devices and Applications.* CRC press (2010).

[17] S. Braun, W. R. Salaneck, and M. Fahlman, Energy-Level Alignment at Organic/Metal and Organic/Organic Interfaces, Adv. Mater. **21**(14-15), 1450–1472 (2009).

[18] T. Miyamachi, M. Gruber, V. Davesne, M. Bowen, S. Boukari, L. Joly, F. Scheurer, G. Rogez, T. K. Yamada, P. Ohresser, and *et al.*, Robust Spin Crossover and Memristance across a Single Molecule, Nature Commun. **3**, 938 (2012).

[19] Y.-L. Loo and I. McCulloch, Progress and Challenges in Commercialization of Organic Electronics, MRS bulletin **33**(07), 653–662 (2008).

[20] S. Horiuchi, R. Kumai, and Y. Tokura, Hydrogen-Bonding Molecular Chains for High-Temperature Ferroelectricity, Adv. Mater. **23**(18), 2098–2103 (2011).

[21] A. Gerlach, T. Hosokai, S. Duhm, S. Kera, O. T. Hofmann, E. Zojer, J. Zegenhagen, and F. Schreiber, Orientational Ordering of Nonplanar Phthalocyanines

on Cu (111): Strength and Orientation of the Electric Dipole Moment, Phys. Rev. Lett. **106**(15), 156102 (2011).

[22] S. Berner, M. De Wild, L. Ramoino, S. Ivan, A. Baratoff, H.-J. Güntherodt, H. Suzuki, D. Schlettwein, and T. A. Jung, Adsorption and Two-Dimensional Phases of a Large Polar Mmolecule: Sub-phthalocyanine on Ag (111), Phys. Rev. B **68**(11), 115410 (2003).

[23] Y. Li Huang, Y. Lu, T. C. Niu, H. Huang, S. Kera, N. Ueno, A. T. S. Wee, and W. Chen, Reversible Single-Molecule Switching in an Ordered Monolayer Molecular Dipole Array, Small **8**(9), 1423–1428 (2012).

[24] T. Yokoyama, T. Takahashi, K. Shinozaki, and M. Okamoto, Quantitative Analysis of Long-Range Interactions between Adsorbed Dipolar Molecules on Cu(111), Phys. Rev. Lett. **98**, 206102 (2007).

[25] J. N. Israelachvili. *Intermolecular and Surface Forces: Revised Third Edition.* Academic press (2011).

[26] L. Xu, X. Miao, X. Ying, and W. Deng, Two-Dimensional Self-Assembled Molecular Structures Formed by the Competition of van der Waals Forces and Dipole–Dipole Interactions, J. Phys. Chem. C **116**(1), 1061–1069 (2011).

[27] G. A. Rojas. *Self Assembly and Interface Chemistry of Non-Metallated Tetraphenyl Porphyrin.* PhD thesis, University of Nebraska, Lincoln (2011).

[28] T. Steiner, The Hydrogen Bond in the Solid State, Angew. Chem. Int. Ed. **41**(1), 48–76 (2002).

[29] D. V. Talapin, E. V. Shevchenko, C. B. Murray, A. V. Titov, and P. Král, Dipole-Dipole Interactions in Nanoparticle Superlattices, Nano Lett. **7**(5), 1213–1219 (2007).

[30] L. Sobczyk, S. J. Grabowski, and T. M. Krygowski, Interrelation between H-bond and Pi-electron delocalization, Chem. Rev. **105**(10), 3513–3560 (2005).

[31] G. Gilli, F. Bellucci, V. Ferretti, and V. Bertolasi, Evidence for Resonance-Assisted Hydrogen Bonding from Crystal-Structure Correlations on the Enol form of the β-diketone fragment, J. Am. Chem. Soc. **111**(3), 1023–1028 (1989).

[32] P.-G. Jönsson and W. C. Hamilton, Hydrogen Bond Studies. LX. A Single Crystal Neutron Diffraction Study of Trichloroacetic Acid Dimer, J. Chem. Phys. **56**, 4433 (1972).

[33] J. Trotter and T. Zobel, Stereochemistry of Arsenic. Part XVI. Cacodylic Acid, J. Chem. Soc. pages 4466–4471 (1965).

[34] S. Horiuchi, Y. Tokunaga, G. Giovannetti, S. Picozzi, H. Itoh, R. Shimano, R. Kumai, and Y. Tokura, Above-Room-Temperature Ferroelectricity in a Single-Component Molecular Crystal, Nature **463**(7282), 789–792 (2010).

[35] Otero, R. and Schöck, M. and Molina, L. M. and Lægsgaard, E. and Stensgaard, I. and Hammer, B. and Besenbacher, F., Guanine Quartet Networks Stabilized by Cooperative Hydrogen Bonds, Angew. Chem. Int. Ed. **44**(15), 2270–2275 (2005).

[36] C. Fonseca Guerra, H. Zijlstra, G. Paragi, and F. M. Bickelhaupt, Telomere Structure and Stability: Covalency in Hydrogen Bonds, Not Resonance Assistance, Causes Cooperativity in Guanine Quartets, Chem. Eur. J. **17**(45), 12612–12622 (2011).

[37] A. Terentjevs, M. P. Steele, M. L. Blumenfeld, N. Ilyas, L. L. Kelly, E. Fabiano, O. L. A. Monti, and F. Della Sala, Interfacial Electronic Structure of the Dipolar Vanadyl Naphthalocyanine on Au (111):Push-Back vs Dipolar Effects, J. Phys. Chem. C **115**(43), 21128–21138 (2011).

[38] A. Crispin, X. Crispin, M. Fahlman, M. Berggren, and W. R. Salaneck, Transition Between Energy Level Alignment Regimes at a Low Band Gap Polymer-Electrode Interfaces, Appl. Phys. Lett. **89**(21), 213503–213503 (2006).

[39] I. G. Hill, A. Rajagopal, A. Kahn, and Y. Hu, Molecular Level Alignment at Organic Semiconductor-Metal Interfaces, Appl. Phys. Lett. **73**(5), 662–664 (1998).

[40] J. Lü, E. Delamarche, L. Eng, R. Bennewitz, E. Meyer, and H.-J. Güntherodt, Kelvin Probe Force Microscopy on Surfaces: Investigation of the Surface Potential of Self-Assembled Monolayers on Gold, Langmuir **15**(23), 8184–8188 (1999).

[41] V. Palermo, M. Palma, and . Samorì, Electronic Characterization of Organic Thin Films by Kelvin Probe Force Microscopy, Adv. Mater. **18**(2), 145–164 (2006).

[42] D. A. Kunkel, J. Hooper, S. Simpson, S. Beniwal, K. L. Morrow, D. C. Smith, K. Cousins, S. Ducharme, E. Zurek, and A. Enders, Rhodizonic Acid on Noble Metals: Surface Reactivity and Coordination Chemistry, J. Phys. Chem. Lett. **4**(20), 3413–3419 (2013).

[43] G. Rojas, S. Simpson, X. Chen, D. A. Kunkel, J. Nitz, J. Xiao, P. A. Dowben, E. Zurek, and A. Enders, Surface State Engineering of Molecule–Molecule Interactions, Phys. Chem. Chem. Phys. **14**(14), 4971–4976 (2012).

[44] T. Niu, C. Zhou, J. Zhang, S. Zhong, H. Cheng, and W. Chen, Substrate Reconstruction Mediated Unidirectionally Aligned Molecular Dipole Dot Arrays, J. Phys. Chem. C **116**(21), 11565–11569 (2012).

[45] K. R. Harikumar, T. Lim, I.R. McNab, J. C. Polanyi, L. Zotti, S. Ayissi, and W. A. Hofer, Dipole-Directed Assembly of Lines of 1, 5-dichloropentane on Silicon Substrates by Displacement of Surface Charge, Nature Nanotech. **3**(4), 222–228 (2008).

[46] S. Kuck, S.-H. Chang, J.-P. Klöckner, M. H. Prosenc, G. Hoffmann, and R. Wiesendanger, Steering Two-Dimensional Molecular Growth via Dipolar Interaction, Chem. Phys. Chem. **10**(12), 2008–2011 (2009).

[47] D. A. Kunkel, S. Simpson, J. Nitz, G. A. Rojas, E. Zurek, L. Routaboul, B. Doudin, P. Braunstein, P. A. Dowben, and A. Enders, Dipole Driven Bonding Schemes of Quinonoid Zwitterions on Surfaces, Chem. Commun. **48**(57), 7143–7145 (2012).

[48] M. Toader and M. Hietschold, SnPc on Ag (111): A Scanning Tunneling Microscopy Study at the Submolecular Level, J. Phys. Chem. C **115**(25), 12494–12500 (2011).

[49] B. de Boer, A. Hadipour, M. M. Mandoc, T. van Woudenbergh, and P. W. M. Blom, Tuning of Metal Work Functions with Self-Assembled Monolayers, Adv. Mater. **17**(5), 621–625 (2005).

[50] D. M. Alloway, M. Hofmann, D. L. Smith, N. E. Gruhn, A. L. Graham, R. Colorado, V. H. Wysocki, T. R. Lee, P. A. Lee, and N. R. Armstrong, Interface Dipoles Arising from Self-Assembled Monolayers on Gold: UV-Photoemission Studies of Alkanethiols and Partially Fluorinated Alkanethiols, J. Phys. Chem. B **107**(42), 11690–11699 (2003).

[51] I. H. Campbell, S. Rubin, T. A. Zawodzinski, J. D. Kress, R. L. Martin, D. L. Smith, N. N. Barashkov, and J. P. Ferraris, Controlling Schottky Energy Barriers in Organic Electronic Devices using Self-Assembled Monolayers, Phys. Rev. B **54**(20), R14321 (1996).

[52] I. H. Campbell, J. D. Kress, R. L. Martin, D. L. Smith, N. N. Barashkov, and J. P. Ferraris, Controlling Charge Injection in Organic Electronic Devices Using Self-Assembled Monolayers, App. Phys. Lett. **71**(24), 3528–3530 (1997).

[53] S. D. Evans and A. Ulman, Surface Potential Studies of Alkyl-Thiol Monolayers Adsorbed on Gold, Chem. Phys. Lett. **170**(5), 462–466 (1990).

[54] R. W. Zehner, B. F. Parsons, R. P. Hsung, and L. R. Sita, Tuning the Work Function of Gold with Self-Assembled Monolayers Derived from X-$[C_6H_4-$

$C \equiv C-]_n C_6 H_4 - SH (n = 0, 1, 2; X = H, F, CH_3, CF_3,$ and OCH_3), Langmuir **15**(4), 1121–1127 (1999).

[55] S. Howell, D. Kuila, B. Kasibhatla, C. P. Kubiak, D. Janes, and R. Reifenberger, Molecular Electrostatics of Conjugated Self-Assembled Monolayers on Au (111) using Electrostatic Force Microscopy, Langmuir **18**(13), 5120–5125 (2002).

[56] M. Bruening, R. Cohen, J. F. Guillemoles, T. Moav, J. Libman, A. Shanzer, and D. Cahen, Simultaneous Control of Surface Potential and Wetting of Solids with Chemisorbed Multifunctional Ligands, J. Am. Chem. Soc. **119**(24), 5720–5728 (1997).

[57] L. F. N. Ah Qune, H. Akiyama, T. Nagahiro, K. Tamada, and A. T. S. Wee, Reversible Work Function Changes Induced by Photoisomerization of Asymmetric Azobenzene Dithiol Self-Assembled Monolayers on Gold, App. Phys. Lett. **93**(8), 083109 (2008).

[58] N. Koch, A. Gerlach, S. Duhm, H. Glowatzki, G. Heimel, A. Vollmer, Y. Sakamoto, T. Suzuki, J. Zegenhagen, J. P. Rabe, and *et al.*, Adsorption-Induced Intramolecular Dipole: Correlating Molecular Conformation and Interface Electronic Structure, J. Am. Chem. Soc. **130**(23), 7300–7304 (2008).

[59] H. Fukagawa, S. Hosoumi, H. Yamane, S. Kera, and N. Ueno, Dielectric Properties of Polar-Phthalocyanine Monolayer Systems with Repulsive Dipole Interaction, Phys. Rev. B **83**(8), 085304 (2011).

[60] S. Kera, Y. Yabuuchi, H. Yamane, H. Setoyama, K. K. Okudaira, A. Kahn, and N. Ueno, Impact of an Interface Dipole Layer on Molecular Level Alignment at an Organic-Conductor Interface Studied by Ultraviolet Photoemission Spectroscopy, Phys. Rev. B **70**(8), 085304 (2004).

[61] M. L. Blumenfeld, M. P. Steele, and O. L. A. Monti, Near-and Far-Field Effects on Molecular Energy Level Alignment at an Organic/Electrode Interface, J. Phys. Chem. Lett. **1**(1), 145–148 (2009).

[62] Y. Wei, W. Tong, C. Wise, X. Wei, K. Armbrust, and M. Zimmt, Dipolar Control of Monolayer Morphology: Spontaneous SAM Patterning, J. Am. Chem. Soc. **128**(41), 13362–13363 (2006).

[63] Y. Wei, W. Tong, and M. B. Zimmt, Self-Assembly of Patterned Monolayers with Nanometer Features: Molecular Selection Based on Dipole Interactions and Chain Length, J. Am. Chem. Soc. **130**(11), 3399–3405 (2008).

[64] W. Tong, X. Wei, and M. B. Zimmt, Dipolar Control of Monolayer Morphology on Graphite: Self-Assembly of Anthracenes with Odd Length Diether Side Chains, J. Phys. Chem. C **113**(39), 17104–17113 (2009).

[65] W. Tong, Y. Wei, K. W. Armbrust, and M. B. Zimmt, Dipolar Side Chain Control of Monolayer Morphology: Symmetrically Substituted 1, 5-(Mono-and diether) Anthracenes at the Solution- HOPG Interface, Langmuir **25**(5), 2913–2923 (2009).

[66] M. K. Kim, Y. Xue, T. Pašková, and M. B. Zimmt, Monolayer Patterning using Ketone Dipoles, Phys. Chem. Chem. Phys. **15**(30), 12466–12474 (2013).

[67] M. M. S. Abdel-Mottaleb, G. Götz, P. Kilickiran, P. Bäuerle, and E. Mena-Osteritz, Influence of Halogen Substituents on the Self-Assembly of Oligothiophenes-A Combined STM and Theoretical Approach, Langmuir **22**(4), 1443–1448 (2006).

[68] Y. Fang, P. Nguyen, O. Ivasenko, M. P. Aviles, E. Kebede, M. S. Askari, X. Ottenwaelder, U. Ziener, O. Siri, and L. A. Cuccia, Charge-Assisted Hydrogen Bond-Directed Self-Assembly of an Amphiphilic Zwitterionic Quinonemonoimine at the Liquid–Solid Interface, Chem. Commun. **47**(40), 11255–11257 (2011).

[69] A. Schiffrin, A. Riemann, W. Auwärter, Y. Pennec, A. Weber-Bargioni, D. Cvetko, A. Cossaro, A. Morgante, and J. V. Barth, Zwitterionic Self-Assembly of L-methionine Nanogratings on the Ag(111) Surface, Proc. Natl. Acad. Sci. **104**(13), 5279–5284 (2007).

[70] S. Lukas, G. Witte, and Ch. Wöll, Novel Mechanism for Molecular Self-Assembly on Metal Substrates: Unidirectional Rows of Pentacene on Cu(110) Produced by a Substrate-Mediated Repulsion, Phys. Rev. Lett. **88**, 028301 (2001).

[71] S. Blankenburg and W. G. Schmidt, Spatial Modulation of Molecular Adsorption Energies Due to Indirect Interaction, Phys. Rev. B **78**, 233411 (2008).

[72] T. Bauert, L. Zoppi, G. Koller, A. Garcia, K. K. Baldridge, and K.-H. Ernst, Large Induced Interface Dipole Moments without Charge Transfer: Buckybowls on Metal Surfaces, J. Phys. Chem. Lett. **2**(21), 2805–2809 (2011).

[73] J. N. Hohman, P. Zhang, E. I. Morin, P. Han, M. Kim, A. R. Kurland, P. D. McClanahan, V. P. Balema, and P. S. Weiss, Self-Assembly of Carboranethiol Isomers on Au {111}: Intermolecular Interactions Determined by Molecular Dipole Orientations, ACS Nano **3**(3), 527–536 (2009).

[74] H. Huang, S. L. Wong, J. Sun, W. Chen, and A. T. S. Wee, Trapping Single Polar Molecules in SiC Nanomesh via Out-of-Plane Dipoles, ACS Nano **6**(3), 2774–2778 (2012).

[75] Z. Mu, Q. Shao, J. Ye, Z. Zeng, Y. Zhao, H. H. Hng, F. Y. C. Boey, J. Wu, and X. Chen, Effect of Intermolecular Dipole- Dipole Interactions on Interfacial Supramolecular Structures of C 3-Symmetric Hexa-peri-hexabenzocoronene Derivatives, Langmuir **27**(4), 1314–1318 (2010).

[76] A. D. Jewell, S. Simpson, A. Enders, E. Zurek, and E. C. H. Sykes, Magic Electret Clusters of 4-Fluorostyrene on Metal Surfaces, J. Phys. Chem. Lett. **3**(15), 2069–2075 (2012).

[77] A. E. Baber, S. C. Jensen, and E. C. H. Sykes, Dipole-Driven Ferroelectric Assembly of Styrene on Au {111}, J. Am. Chem. Soc. **129**(20), 6368–6369 (2007).

[78] O. P. H. Vaughan, A. Alavi, F. J. Williams, and R. M. Lambert, Dipole Amplification: A Principle for the Self-Assembly of Asymmetric Monomers on Metal Surfaces, Angew. Chem. Int. Ed. **47**(13), 2422–2426 (2008).

[79] I. Fernandez-Torrente, S. Monturet, K. J. Franke, J. Fraxedas, N. Lorente, and J. I. Pascual, Long-Range Repulsive Interaction between Molecules on a Metal Surface Induced by Charge Transfer, Phys. Rev. Lett. **99**(17), 176103 (2007).

[80] C. Ganzorig, K.-J. Kwak, K. Yagi, and M. Fujihira, Fine Tuning Work Function of Indium Tin Oxide by Surface Molecular Design: Enhanced Hole Injection in Organic Electroluminescent Devices, Appl. Phys. Lett. **79**(2), 272–274 (2001).

[81] N. D. Lang and W. Kohn, Theory of Metal Surfaces: Charge Density and Surface Energy, Phys. Rev. B **1**(12), 4555 (1970).

[82] G. A. Somorjai and Y. Li. *Introduction to Surface Chemistry and Catalysis.* John Wiley & Sons (2010).

[83] R. W. Strayer, W. Mackie, and L. W. Swanson, Work Function Measurements by the Field Emission Retarding Potential Method, Surf. Sci. **34**(2), 225 – 248 (1973).

[84] A. Zangwill. *Physics at Surfaces.* Cambridge University Press (1988).

[85] J. F. Jia, K. Inoue, Y. Hasegawa, W. S. Yang, and T. Sakurai, Variation of the Local Work Function at Steps on Metal Surfaces Studied with STM, Phys. Rev. B **58**(3), 1193 (1998).

[86] A. Hauschild, K. Karki, B. C. C. Cowie, M. Rohlfing, F. S. Tautz, and M. Sokolowski, Molecular Distortions and Chemical Bonding of a Large π-Conjugated Molecule on a Metal Surface, Phys. Rev. Lett. **94**(3), 036106 (2005).

[87] J. I. Martínez, E. Abad, C. González, J. Ortega, and F. Flores, Theoretical Characterization of the TTF/Au (111) Interface: STM Imaging, Band Alignment and Charging Energy, Org. Electron. **13**(3), 399–408 (2012).

[88] P. S. Bagus, V. Staemmler, and C. Wöll, Exchangelike Effects for Closed-Shell Adsorbates: Interface Dipole and Work Function., Phys. Rev. Lett. **89**(9), 096104–096104 (2002).

[89] P. S. Bagus, K. Hermann, and C. Wöll, The Interaction of C6H6 and C6H12 with Noble Metal Surfaces: Electronic Level Alignment and the Origin of the Interface Dipole, J. Chem. Phys. **123**(18), 184109 (2005).

[90] G. Witte, S. Lukas, P. S. Bagus, and C. Wöll, Vacuum Level Alignment at Organic/Metal Junctions:Cushion Effect and the Interface Dipole, Appl. Phys. Lett. **87**(26), 263502 (2005).

[91] L. Vitali, G. Levita, R. Ohmann, A. Comisso, A. De Vita, and K. Kern, Portrait of the Potential Barrier at Metal-Organic Nanocontacts, Nature Mater. **9**(4), 320–323 (2010).

[92] H. Vázquez, F. Flores, and A. Kahn, Induced Density of States model for Weakly-Interacting Organic Semiconductor Interfaces, Org. Electron. **8**(2), 241–248 (2007).

[93] H. Vázquez, Y. J. Dappe, J. Ortega, and F. Flores, Energy Level Alignment at Metal/Organic Semiconductor Interfaces:Pillow Effect, Induced Density of Interface States, and Charge Neutrality Level, J. Chem. Phys. **126**, 144703 (2007).

[94] M. G. Betti, A. Kanjilal, C. Mariani, H. Vázquez, Y. J. Dappe, J. Ortega, and F. Flores, Barrier Formation at Organic Interfaces in a Cu (100)-Benzenethiolate-Pentacene Heterostructure, Phys. Rev. Lett. **100**(2), 027601 (2008).

[95] I. G. Hill, J. Schwartz, and A. Kahn, Metal-Dependent Charge Transfer and Chemical Interaction at Interfaces Between 3, 4, 9, 10-perylenetetracarboxylic Bisimidazole and Gold, Silver and Magnesium, Org. Electron. **1**(1), 5–13 (2000).

[96] I. G. Hill, A. Rajagopal, and A. Kahn, Energy-Level Alignment at Interfaces Between Metals and the Organic Semiconductor 4, 4-N, N-dicarbazolyl-biphenyl, J. Appl. Phys. **84**(6), 3236–3241 (1998).

[97] H. Peisert, M. Knupfer, T. Schwieger, J. M. Auerhammer, M. S. Golden, and J. Fink, Full Characterization of the Interface Between the Organic Semiconductor Copper Phthalocyanine and Gold, J. Appl. Phys. **91**(8), 4872–4878 (2002).

[98] W. Gao and A. Kahn, Controlled P Doping of the Hole-Transport Molecular Material N, N-diphenyl-N, N-bis (1-naphthyl)-1, 1-biphenyl-4, 4-diamine with Tetrafluorotetracyanoquinodimethane, J. Appl. Phys. **94**(1), 359–366 (2003).

[99] A. Wan, J. Hwang, F. Amy, and A. Kahn, Impact of Electrode Contamination on the α-NPD/Au Hole Injection Barrier, Org. Electron. **6**(1), 47–54 (2005).

[100] X. Crispin, V. Geskin, A. Crispin, J. Cornil, R. Lazzaroni, W. R. Salaneck, and J.-L. Brédas, Characterization of the Interface Dipole at Organic/Metal Interfaces, J. Am. Chem. Soc. **124**(27), 8131–8141 (2002).

[101] R. H. Williams, Surface Defect Effects on Schottky Barriers, J. Vac. Sci. Tech. **18**(3), 929–936 (1981).

[102] J. Tersoff and D. R. Hamann, Theory of the Scanning Tunneling Microscope, Phys. Rev. B **31**, 805–813 (1985).

[103] C. J. Chen. *Introduction to Scanning Tunneling Microscopy: Second Edition.* Oxford Science Publications (2008).

[104] T. Maroutian, S. Degen, C. Becker, K. Wandelt, and R. Berndt, Superstructures and Coincidences of a Thin Oxide Film on a Metallic Substrate: A STM Study, Phys. Rev. B **68**(15), 155414 (2003).

[105] G. Binnig, K. H. Frank, H. Fuchs, N. Garcia, B. Reihl, H. Rohrer, F. Salvan, and A. R. Williams, Tunneling Spectroscopy and Inverse Photoemission: Image and Field States, Phys. Rev. Lett. **55**, 991–994 (1985).

[106] X. Chen. *Ultrathin Oxide Films as Templates for Magnetic Nanostructures.* PhD thesis, University of Nebraska, Lincoln (2012).

[107] A. Pronschinske, D. J. Mardit, and D. B. Dougherty, Modeling the Constant-Current Distance-Voltage Mode of Scanning Tunneling Spectroscopy, Phys. Rev. B **84**(20), 205427 (2011).

[108] B. C. Stipe, M. A. Rezaei, and W. Ho, Single-Molecule Vibrational Spectroscopy and Microscopy, Science **280**(5370), 1732–1735 (1998).

[109] G. Binnig, H. Rohrer, C. Gerber, and E. Weibel, Tunneling through a Controllable Vacuum Gap, Appl. Phys. Lett. **40**(2), 178–180 (1982).

[110] G. Binnig, H. Rohrer, C. Gerber, and E. Weibel, Surface Studies by Scanning Tunneling Microscopy, Phys. Rev. Lett. **49**(1), 57 (1982).

[111] J. C. Slonczewski, Conductance and Exchange Coupling of Two Ferromagnets Separated by a Tunneling Barrier, Phys. Rev. B **39**(10), 6995 (1989).

[112] M. Kleiber, M. Bode, R. Ravlić, and R. Wiesendanger, Topology-Induced Spin Frustrations at the Cr (001) Surface Studied by Spin-Polarized Scanning Tunneling Spectroscopy, Phys. Rev. Lett. **85**(21), 4606 (2000).

[113] T. Arai, K. Ichimura, K. Nomura, S. Takasaki, J. Yamada, S. Nakatsuji, and H. Anzai, Tunneling Spectroscopy on the Organic Superconductor κ-(BEDT-TTF)$_2$ Cu(NCS)$_2$ using STM, Phys. Rev. B **63**(10), 104518 (2001).

[114] B. Giambattista, A. Johnson, R. V. Coleman, B. Drake, and P. K. Hansma, Charge-Density Waves Observed at 4.2 K by Scanning-Tunneling Microscopy, Phys. Rev. B **37**(5), 2741 (1988).

[115] Z. Z. Wang, J. C. Girard, C. Pasquier, D. Jérome, and K. Bechgaard, Scanning Tunneling Microscopy in TTF-TCNQ: Phase and Amplitude Modulated Charge Density Waves, Phys. Rev. B **67**(12), 121401 (2003).

[116] M. F. Crommie, C. P. Lutz, and D. M. Eigler, Confinement of Electrons to Quantum Corrals on a Metal Surface, Science **262**(5131), 218–220 (1993).

[117] S.-W. Hla, L. Bartels, G. Meyer, and K.-H. Rieder, Inducing all Steps of a Chemical Reaction with the Scanning Tunneling Microscope Tip: Towards Single Molecule Engineering, Phys. Rev. Lett. **85**(13), 2777 (2000).

[118] P. Braunstein, O. Siri, J.-P. Taquet, M.-M. Rohmer, M. Bénard, and R. Welter, A $6\pi + 6\pi$ Potentially Antiaromatic Zwitterion Preferred to a Quinoidal Structure: Its Reactivity Toward Organic and Inorganic Reagents, J. Am. Chem. Soc. **125**(40), 12246–12256 (2003).

[119] V. I. Minkin, M. N. Glukhovtsev, and B. Ya. Simkin. *Aromaticity and Antiaromaticity* (1994).

[120] R. Breslow, Small Antiaromatic Rings, Angew. Chem. Int. Ed. **7**(8), 565–570 (1968).

[121] L. Beer, R. T. Oakley, J. R. Mingie, K. E. Preuss, N. J. Taylor, and A. W. Cordes, Antiaromatic Bis (1, 2, 3-dithiazoles) with Zwitterionic Ground States, J. Am. Chem. Soc. **122**(31), 7602–7603 (2000).

[122] K. Hutchison, G. Srdanov, R. Hicks, H. Yu, F. Wudl, T. Strassner, M. Nendel, and K. N. Houk, Tetraphenylhexaazaanthracene: A Case for Dominance of Cyanine Ion Stabilization Overwhelming 16π Antiaromaticity, J. Am. Chem. Soc. **120**(12), 2989–2990 (1998).

[123] H. T. Le, P. C. Nam, V. L. Dao, T. Veszprémi, and M. T. Nguyen, Molecular and Electronic Structure of Zwitterionic Diamino-Meta-Quinonoid Molecules, Mol. Phys. **101**(15), 2347–2355 (2003).

[124] L. Routaboul, P. Braunstein, J. Xiao, Z. Zhang, P. A. Dowben, G. Dalmas, V. Da Costa, O. Felix, G. Decher, L. G. Rosa, and *et al.*, Altering the Static Dipole on Surfaces through Chemistry: Molecular Films of Zwitterionic Quinonoids, J. Am. Chem. Soc. **134**(20), 8494–8506 (2012).

[125] Q.-Z. Yang, O. Siri, and P. Braunstein, First Transamination Reactions for the One-Pot Synthesis of Substituted Zwitterionic Quinones, Chem. Commun. (21), 2660–2662 (2005).

[126] Q. Yang, O. Siri, and P. Braunstein, Tunable N-substitution in Zwitterionic Benzoquinonemonoimine Derivatives: Metal Coordination, Tandemlike Synthesis of Zwitterionic Metal Complexes, and Supramolecular Structures, Chem. Eur. J. **11**, 7237–7246 (2005).

[127] Q.-Z. Yang, A. Kermagoret, M. Agostinho, O. Siri, and P. Braunstein, Nickel Complexes with Functional Zwitterionic N, O-benzoquinonemonoimine-type Ligands: Syntheses, Structures, and Catalytic Oligomerization of Ethylene, Organometallics **25**(23), 5518–5527 (2006).

[128] J.-P. Taquet, O. Siri, P. Braunstein, and R. Welter, Stepwise Synthesis, Structures, and Reactivity of Mono-, Di-, and Trimetallic Metal Complexes with a $6\pi+ 6\pi$ Quinonoid Zwitterion, Inorg. Chem. **43**(22), 6944–6953 (2004).

[129] J. Xiao, Z. Zhang, D. Wu, L. Routaboul, P. Braunstein, B. Doudin, Y. B. Losovyj, O. Kizilkaya, L. G. Rosa, C. N. Borca, and *et al.*, The Interface Bonding and Orientation of a Quinonoid Zwitterion, Phys. Chem. Chem. Phys. **12**(35), 10329–10340 (2010).

[130] Z. Zhang, J. Alvira, X. Barbosa, L. G. Rosa, L. Routaboul, P. Braunstein, B. Doudin, and P. A. Dowben, Lock and Key Adsorption Chemistry: Preferential Absorption of an Isomer of Di-iodobenzene on Molecular Films of Quinonoid Zwitterions, J. Phys. Chem. C **115**(6), 2812–2818 (2011).

[131] L. Kong, G. J. Perez Medina, J. A. Colón Santana, F. Wong, M. Bonilla, D. A. Colón Amill, L. G. Rosa, L. Routaboul, P. Braunstein, B. Doudin, and *et al.*, Weak Screening of a Large Dipolar Molecule Adsorbed on Graphene, Carbon **50**(5), 1981–1986 (2012).

[132] J. V. Barth, H. Brune, G. Ertl, and R. J. Behm, Scanning Tunneling Microscopy Observations on the Reconstructed Au(111) Surface: Atomic Structure, Long-Range Superstructure, Rotational Domains, and Surface Defects, Phys. Rev. B **42**, 9307–9318 (1990).

[133] Ch. Wöll, S. Chiang, R. J. Wilson, and P. H. Lippel, Determination of Atom Positions at Stacking-Fault Dislocations on Au(111) by Scanning Tunneling Microscopy, Phys. Rev. B **39**, 7988–7991 (1989).

[134] S. Simpson, D. A. Kunkel, J. Hooper, J. Nitz, P. A. Dowben, L. Routaboul, P. Braunstein, B. Doudin, A. Enders, and E. Zurek, Coverage-Dependent Interactions at the Organics–Metal Interface: Quinonoid Zwitterions on Au (111), J. Phys. Chem. C **117**(32), 16406–16415 (2013).

[135] M. Pivetta, M.-C. Blüm, F. Patthey, and W.-D. Schneider, Coverage-Dependent Self-Assembly of Rubrene Molecules on Noble Metal Surfaces Observed by Scanning Tunneling Microscopy, Chem. Phys. Chem. **11**(7), 1558–1569 (2010).

[136] A. C. Papageorgiou, S. Fischer, J. Reichert, K. Diller, F. Blobner, F. Klappenberger, F. Allegretti, A. P. Seitsonen, and J. V. Barth, Chemical Transformations Drive Complex Self-Assembly of Uracil on Close-Packed Coinage Metal Surfaces, ACS Nano **6**(3), 2477–2486 (2012).

[137] J. Fraxedas, S. García-Gil, S. Monturet, N. Lorente, I. Fernández-Torrente, K. J. Franke, J. I. Pascual, A. Vollmer, R.-P. Blum, N. Koch, and *et al.*, Modulation of Surface Charge Transfer through Competing Long-Range Repulsive Versus Short-Range Attractive Interactions, J. Phys. Chem. C **115**(38), 18640–18648 (2011).

[138] N. Kovačević and A. Kokalj, DFT Study of Interaction of Azoles with Cu (111) and Al (111) Surfaces: Role of Azole Nitrogen Atoms and Dipole–Dipole Interactions, J. Phys. Chem. C **115**(49), 24189–24197 (2011).

[139] Th. Wagner, A. Bannani, C. Bobisch, H. Karacuban, and R. Möller, The Initial Growth of PTCDA on Cu (111) Studied by STM, J. Phys.: Cond. Matter **19**(5), 056009 (2007).

[140] F. Bocquet, L. Nony, S.C.B. Mannsfeld, V. Oison, R. Pawlak, L. Porte, and Ch. Loppacher, Inhomogeneous Relaxation of a Molecular Layer on an Insulator due to Compressive Stress, Phys. Rev. Lett. **108**(20), 206103 (2012).

[141] A. Hoshino, S. Isoda, H. Kurata, and T. Kobayashi, Scanning Tunneling Microscope Contrast of Perylene-3, 4, 9, 10-tetracarboxylic-dianhydride on Graphite and its Application to the Study of Epitaxy, J. Appl. Phys. **76**(7), 4113–4120 (1994).

[142] E. Goiri, J. M. García Lastra, M. Corso, Z.M. Adb El-Fattah, J.E. Ortega, and D.G. de Oteyza, Understanding Periodic Dislocations in 2D Supramolecular Crystals: The PFP/Ag (111) Interface, J. Phys. Chem. Lett. **3**(7), 848–852 (2012).

[143] K. Berland, T. L. Einstein, and P. Hyldgaard, Rings Sliding on a Honeycomb Network: Adsorption Contours, Interactions, and Assembly of Benzene on Cu (111), Phys. Rev. B **80**(15), 155431 (2009).

[144] W. Liu, J. Carrasco, B. Santra, A. Michaelides, M. Scheffler, and A. Tkatchenko, Benzene Adsorbed on Metals: Concerted Effect of Covalency and van der Waals Bonding, Phys. Rev. B **86**(24), 245405 (2012).

[145] D. Payer, A. Comisso, A. Dmitriev, T. Strunskus, N. Lin, C. Wöll, A. DeVita, J. V. Barth, and K. Kern, Ionic Hydrogen Bonds Controlling Two-Dimensional Supramolecular Systems at a Metal Surface, Chem. Eur. J. **13**(14), 3900–3906 (2007).

[146] S. Fischer, A. C. Papageorgiou, M. Marschall, J. Reichert, K. Diller, F. Klappenberger, F. Allegretti, A. Nefedov, C. Woll, and J. V. Barth, l-Cysteine on Ag (111): A Combined STM and X-ray Spectroscopy Study of Anchorage and Deprotonation, J. Phys. Chem. C **116**(38), 20356–20362 (2012).

[147] J. I. Pascual, J. V. Barth, G. Ceballos, G. Trimarchi, A. De Vita, K. Kern, and H.-P. Rust, Mesoscopic Chiral Reshaping of the Ag(110) Surface Induced by the Organic Molecule PVBA, J. Chem. Phys. **120**, 11367 (2004).

[148] B. Parker, B. Immaraporn, and A. J. Gellman, Carboxylic Acid Deprotonation on the Ag(110) and Ag(111) Surfaces, Langmuir **17**(21), 6638–6646 (2001).

[149] H. Walch, J. Dienstmaier, G. Eder, R. Gutzler, S. Schlögl, T. Sirtl, K. Das, M. Schmittel, and M. Lackinger, Extended Two-Dimensional Metal–Organic Frameworks Based on Thiolate–Copper Coordination Bonds, J. Am. Chem. Soc. **133**(20), 7909–7915 (2011).

[150] A. Schiffrin, J. Reichert, Y. Pennec, W. Auwärter, A. Weber-Bargioni, M. Marschall, M. Dell'Angela, D. Cvetko, G. Bavdek, A. Cossaro, A. Morgante, and J. V. Barth, Self-Assembly of l-Methionine on Cu(111): Steering Chiral Organization by Substrate Reactivity and Thermal Activation, J. Phys. Chem. C **113**(28), 12101–12108 (2009).

[151] T. Classen, G. Fratesi, G. Costantini, S. Fabris, F. L. Stadler, C. Kim, S. de Gironcoli, S. Baroni, and K. Kern, Templated Growth of Metal–Organic Coordination Chains at Surfaces, Angew. Chem. **117**(38), 6298–6301 (2005).

[152] S. Stepanow, N. Lin, F. Vidal, A. Landa, M. Ruben, J. V. Barth, and K. Kern, Programming Supramolecular Assembly and Chirality in Two-Dimensional Dicarboxylate Networks on a Cu (100) Surface, Nano Lett. **5**(5), 901–904 (2005).

[153] S. L. Tait, Y. Wang, G. Costantini, N. Lin, A. Baraldi, F. Esch, L. Petaccia, S. Lizzit, and K. Kern, Metal-Organic Coordination Interactions in Fe-Terephthalic Acid Networks on Cu(100), J. Am. Chem. Soc. **130**(6), 2108–2113 (2008).

[154] M. N. Faraggi, C. Rogero, A. Arnau, M. Trelka, D. Écija, C. Isvoranu, J. Schnadt, C. Marti-Gastaldo, E. Coronado, J. M. Gallego, R. Otero, and R. Miranda, Role of Deprotonation and Cu Adatom Migration in Determining the Reaction Pathways of Oxalic Acid Adsorption on Cu(111), J. Phys. Chem. C **115**(43), 21177–21182 (2011).

[155] Q. Chen, C. C. Perry, B. G. Frederick, P. W. Murray, S. Haq, and N. V. Richardson, Structural Aspects of the Low-Temperature Deprotonation of Benzoic Acid on Cu (110) Surfaces, Surf. Sci. **446**(1), 63–75 (2000).

[156] S. Clair, S. Pons, S. Fabris, S. Baroni, H. Brune, K. Kern, and J. V. Barth, Monitoring Two-Dimensional Coordination Reactions: Directed Assembly of Co-Terephthalate Nanosystems on Au(111), J. Phys. Chem. B **110**(11), 5627–5632 (2006).

[157] G. Ertl. *Reactions at Solid Surfaces*, volume 14. John Wiley & Sons (2010).

[158] Private communication with Scott Simpson.

[159] A. Enders, R. Skomski, and J. Honolka, Magnetic Surface Nanostructures, J. Phys.: Cond. Mat. **22**(43), 433001 (2010).

[160] P. Han and P. S. Weiss, Electronic Substrate-Mediated Interactions, Surf. Sci. Rep. **67**(2), 19–81 (2012).

[161] A. Stroppa, D. Di Sante, S. Horiuchi, Y. Tokura, D. Vanderbilt, and S. Picozzi, Polar Distortions in Hydrogen-Bonded Organic Ferroelectrics, Phys. Rev. B **84**(1), 014101 (2011).

[162] C. Rovira, J. J. Novoa, and P. Ballone, Hydrogen Bonding and Collective Proton Modes in Clusters and Periodic Layers of Squaric Acid: A Density Functional Study, J. Chem. Phys. **115**, 6406 (2001).

[163] K. Noda, K. Ishida, A. Kubono, T. Horiuchi, H. Yamada, and K. Matsushige, Remanent Polarization of Evaporated Films of Vinylidene Fluoride Oligomers, J. Appl. Phys. **93**(5), 2866–2870 (2003).

[164] S. Horiuchi and Y. Tokura, Organic Ferroelectrics, Nature Mater. **7**(5), 357–366 (2008).

[165] D. Braga, G. Cojazzi, L. Maini, and F. Grepioni, Reversible Solid-State Inter-conversion of Rhodizonic Acid $H_2C_6O_6$ into $H_6C_6O_8$ and the Solid-State Structure of the Rhodizonate Dianion $C_6O_6^{2-}$ (Aromatic or Non-Aromatic?), New J. Chem. **25**(10), 1221–1223 (2001).

[166] E. Patton and R. West, New Aromatic Anions. VIII. Acidity Constants of Rhodizonic Acid, J. Phys. Chem. **74**(12), 2512–2518 (1970).

[167] W. Städeli, R. Hollenstein, and W. Von Philipsborn, 13C-NMR. Spectra, Structure and Reactivity of Cyclic Oxocarbons, Helvetica Chimica Acta **60**(3), 948–958 (1977).

[168] M. Wu, J. D. Burton, E. Y. Tsymbal, X. C. Zeng, and P. Jena, Multiferroic Materials Based on Organic Transition-Metal Molecular Nanowires, J. Am. Chem. Soc. **134**(35), 14423–14429 (2012).

[169] C.-C. Wang, C.-T. Kuo, P.-T. Chou, and G.-H. Lee, Rhodizonate Metal Complexes with a 2D Chairlike M6 Metal–Organic Framework:[M $(C_6O_6)(bpym)(H_2O)]nH_2O$, Angew. Chem. Int. Ed. **43**(34), 4507–4510 (2004).

[170] S. Beniwal, S. Chen, X.-C. Zeng, S. Simpson, J. Hooper, E. Zurek, D. A. Kunkel, and A. Enders, Kagome Lattice of $\pi - \pi$ stacked 3-Hydroxyphenalenone on Cu(111), Chem. Commun. (2014).

[171] D. A. Kunkel, J. Hooper, S. Simpson, G. A. Rojas, S. Ducharme, T. Usher, E. Zurek, and A. Enders, Proton Transfer in Surface-Stabilized Chiral Motifs of Croconic Acid, Phys. Rev. B **87**(4), 041402 (2013).

[172] S. Grimme, J. Antony, S. Ehrlich, and H. Krieg, A Consistent and Accurate ab initio Parametrization of Density Functional Dispersion Correction (DFT-D) for the 94 Elements H-Pu, J. Chem. Phys. **132**, 154104 (2010).

[173] C. N. Ramachandran and E. Ruckenstein, Density Functional Theoretical Studies of the Isomers of Croconic Acid and their Dimers, Comp. Theor. Chem. **973**, 28–32 (2011).

[174] D.G. Nocera, B.M. Bartlett, D. Grohol, D. Papoustsakis, and M.P. Shores, Spin Frustration in 2D Kagomé Lattices: A Problem for Inorganic Synthetic Chemistry, Chem. Eur. J. **10**, 3850 (2004).

[175] L. Messio, B. Bernu, and C. Lhuililer, Kagome Antiferromagnet: A Chiral Topological Spin Liquid?, Phys. Rev. Lett. **108**, 207204 (2012).

[176] S. Yamanaka, D. Yamaki, H. Takeda, Y.and Nagao, and K. Yamaguchi, J-Model for Magnetism and Superconductivity of Triangular, Kagome, and Related Spin Lattice Systems, J. Quantum Chem. **100**, 1179 (2004).

[177] B. Moulton, J. Lu, R. Hajndl, S. Hariharan, and M. J. Zaworotko, Crystal Engineering of a Nanoscale Kagomé Lattice, Angew. Chem. Int. Ed. **114**, 2945 (2002).

[178] H. Zhou, J.-H. Dang, H.and Yi, A. Nanci, A. Rochefort, and J. D. Wuest, Frustrated 2D Molecular Crystallization, J. Am. Chem. Soc. **129**(45), 13774–13775 (2007).

[179] M. Blunt, X. Lin, M. d. C. Gimenez-Lopez, M. Schröllder, N.R. Champness, and P. H. Beton, Directing Two-Dimensional Molecular Crystallization using Guest Templates, Chem. Commun. page 2304 (2007).

[180] J. Adisoejoso, K. Tahara, S. Okuhata, S. Lei, Y. Tobe, and S. De Feyter, Two-Dimensional Crystal Engineering: A Four-Component Architecture at a Liquid-Solid Interface, Angew. Chem. Int. Ed. **48**, 7353–7357 (2009).

[181] M. Stöhr, M. Wahl, H. Spillman, L.H. Gade, and T.A. Jung, Lateral Manipulation for the Positioning of Molecular Guests within the Confinements of a Highly Stable Self-Assembled Organic Surface Network, Small **3**, 1336–1340 (2007).

[182] Z. Shi and N. Lin, Porphyrin-Based Two-Dimensional Coordination Kagome Lattice Self-Assembled on a Au(111) Surface, J. Am. Chem. Soc. **131**, 5377 (2009).

[183] U. Schlickum, R. Decker, F. Klappenberger, G. Zoppellarp, S. Klyatskaya, W. Auwärter, S. Neppl, K. Kern, H. Brune, M. Ruben, and J. V. Barth, Chiral Kagome Lattice from Simple Ditoptic Molecular Bricks, J. Am. Chem. Soc. **130**, 11778 (2008).

[184] S. Furukawa, H. Uji-I, K. Tahara, T. Ichikawa, M. Sonoda, F. C. De Schryver, Y. Tobe, and S. De Feyter, Molecular Geometry Directed Kagomé and Honeycomb Networks: Toward Two-Dimensional Crystal Engineering, J. Am. Chem. Soc. **128**, 3502 (2006).

[185] T. Chen, Q. Chen, X. Zhang, D. Wang, and L.-J. Wan, Chiral Kagome Network from Thiacalix[4]arene Tetrasulfonate at the Interafce of Aqueous Solution/Au(111) Surface: An in Situ Electrochemical Scanning Tunneling Microscopy Study, J. Am. Chem. Soc. **132**, 5598 (2010).

[186] J. Mao, H. Zhang, Y. Jiang, Y. Pan, M. Gao, Xiao W., and H.-J. Gao, Tunability of Supramolecular Kagome Lattices of Magnetic Phthalocyanines using Graphene-Based Moiré Patterns as Templates, J. Am. Chem. Soc. **131**, 14136 (2009).

[187] K. Tahara, S. Okuhata, J. Adisoejoso, S. Lei, T. Fujita, S. De Feyter, and Y. Tobe, 2D Networks of Rhombic-Shaped Fused Dehydrobenzo[12]annulenes: Structural Variations under Concentration Control, J. Am. Chem. Soc. **131**(48), 17583–17590 (2009).

[188] B. Glettner, F. Liu, X. Zeng, M. Prehm, M. Baumeister, U. Walker, M.A. Bates, P. Boesecke, G. Ungar, and C. Tschierske, Liquid-Crystalline Kagome, Angew. Chem. Int. Ed. **47**, 9063 (2008).

[189] J. Malo, J.C. Mitchell, C. Vénien-Bryan, J. R. Harris, H. Willie, D. J. Sherratt, and A.J. Tuberfield, Engineering a 2D Protein-DNA Crystal, Angew. Chem. Int. Ed. **44**, 3057 (2005).

[190] Q. Chen, S. C. Bae, and S. Granick, Directed Self-Assembly of a Colloidal Kagome Lattice, Nature **469**, 381–384 (2011).

[191] S. Stepanow, N. Lin, J. V. Barth, and K. Kern, Surface-Template Assembly of Two-Dimensional Metal-Organic Coordination Networks, J. Phys. Chem. B **110**(46), 23472–23477 (2006).

[192] M. Corso, W. Auwärter, M. Muntwiler, A. Tamai, T. Greber, and J. Osterwalder, Boron Nitride Nanomesh, Science **303**(5655), 217–220 (2004).

[193] S. Bose, A. M. García-García, M. M. Ugeda, J. D. Urbina, C. H. Michaelis, I. Brihuega, and K. Kern, Observation of Shell Effects in Superconducting Nanoparticles of Sn, Nature Mater. **9**(7), 550–554 (2010).

[194] I. Brihuega, C. H. Michaelis, J. Zhang, S. Bose, V. Sessi, J. Honolka, M. Alexander Schneider, A. Enders, and K. Kern, Electronic Decoupling and Templating of Co Nanocluster Arrays on the Boron Nitride Nanomesh, Surf. Sci. **602**(14), L95–L99 (2008).

[195] J. Repp, G. Meyer, S. M. Stojković, A. Gourdon, and C. Joachim, Molecules on Insulating Films: Scanning-Tunneling Microscopy Imaging of Individual Molecular Orbitals, Phys. Rev. Lett. **94**, 026803 (2005).

[196] V. Sessi, K. Kuhnke, J. Zhang, J. Honolka, K. Kern, A. Enders, P. Bencok, S. Bornemann, J. Minár, and H. Ebert, Cobalt Nanoclusters on Metal-Supported Xe Monolayers: Influence of the Substrate on Cluster Formation Kinetics and Magnetism, Phys. Rev. B **81**(19), 195403 (2010).

[197] J. H. Weaver and G. D. Waddill, Cluster Assembly of Interfaces: Nanoscale Engineering, Science **251**(5000), 1444–1451 (1991).

[198] V. C. Zoldan, R. Faccio, C. Gao, and A. A. Pasa, Coupling of Cobalt–Tetraphenylporphyrin Molecules to a Copper Nitride Layer, J. Phys. Chem. C **117**(31), 15984–15990 (2013).

[199] S. M. Driver and D. P. Woodruff, Nitrogen Adsorption Structures on Cu (100) and the Role of a Symmetry-Lowering Surface Reconstruction in the c (2×2)-N Phase, Surf. Sci. **492**(1), 11–26 (2001).

[200] B. Lu, T. Iimori, K. Sakamoto, K. Nakatsuji, F. Rosei, and F. Komori, Fullerene on Nitrogen-Adsorbed Cu (001) Nanopatterned Surfaces: From Preferential Nucleation to Layer-by-Layer Growth, J. Phys. Chem. C **112**(27), 10187–10192 (2008).

[201] Y. Matsumoto and K.-i. Tanaka, Growth of Nanosize Ni Thin Films on a Modified c ($2\times$ 2)-N Cu (100) Surface, Jpn. J. Appl. Phys. **37**, L154–L157 (1998).

[202] F. Komori, S.-y. Ohno, and K. Nakatsuji, Lattice Deformation and Strain-Dependent Atom Processes at Nitrogen-Modified Cu (001) Surfaces, Prog. Surf. Sci. **77**(1), 1–36 (2004).

[203] D. Braga, L. Maini, and F. Grepioni, Croconic Acid and Alkali Metal Croconate Salts: Some New Insights into an Old Story, Chem. Eur. J. **8**(8), 1804–1812 (2002).

[204] Private communication with James Hooper, March 2014.

[205] J. F. Dienstmaier, K. Mahata, H. Walch, W. M. Heckl, M. Schmittel, and M. Lackinger, On the Scalability of Supramolecular Networks- High Packing Density vs Optimized Hydrogen Bonds in Tricarboxylic Acid Monolayers, Langmuir **26**(13), 10708–10716 (2010).

[206] C. Meier, M. Roos, D. Künzel, A. Breitruck, H. E. Hoster, K. Landfester, A. Gross, R. J. Behm, and U. Ziener, Concentration and Coverage Dependent Adlayer Structures: From Two-Dimensional Networks to Rotation in a Bearing, J Phys. Chem. C **114**(2), 1268–1277 (2009).

[207] P. W. Preisler, L. Berger, and E. S. Hill, Oxidation–Reduction Potentials and Ionization Constants of the Reversible Series: Hexahydroxybenzene–Tetrahydroxyquinone–Rhodizonic Acid, J. Am. Chem. Soc. **69**(2), 326–329 (1947).

[208] S. L. Tait, A. Langner, N. Lin, S. Stepanow, C. Rajadurai, M. Ruben, and K. Kern, One-Dimensional Self-Assembled Molecular Chains on Cu (100): Interplay Between Surface-Assisted Coordination Chemistry and Substrate Commensurability, J. Phys. Chem. C **111**(29), 10982–10987 (2007).

[209] D. Kühne, F. Klappenberger, R. Decker, U. Schlickum, H. Brune, S. Klyatskaya, M. Ruben, and J. V. Barth, High-Quality 2D Metal- Organic Coordination Network Providing Giant Cavities within Mesoscale Domains, J. Am. Chem. Soc. **131**(11), 3881–3883 (2009).

[210] C. S. Kley, J. Čechal, T. Kumagai, F. Schramm, M. Ruben, S. Stepanow, and K. Kern, Highly Adaptable Two-Dimensional Metal–Organic Coordination Networks on Metal Surfaces, J. Am. Chem. Soc. **134**(14), 6072–6075 (2012).

[211] S. Stepanow, N. Lin, D. Payer, U. Schlickum, F. Klappenberger, G. Zoppellaro, M. Ruben, H. Brune, J. V. Barth, and K. Kern, Surface-Assisted Assembly of 2D Metal–Organic Networks that Exhibit Unusual Threefold Coordination Symmetry, Angew. Chem. **119**(5), 724–727 (2007).

[212] T. P. Martin, Shells of Atoms, Phys. Rep. **273**(4), 199–241 (1996).

[213] C. L. Cleveland and U. Landman, The Energetics and Structure of Nickel Clusters: Size Dependence, J. Chem. Phys. **94**(11), 7376–7396 (1991).

[214] W. A. de Heer, The Physics of Simple Metal Clusters: Experimental Aspects and Simple Models, Rev. Mod. Phys. **65**(3), 611 (1993).

[215] A. Dmitriev, H. Spillmann, N. Lin, J. V. Barth, and K. Kern, Modular Assembly of Two-Dimensional Metal–Organic Coordination Networks at a Metal Surface, Angew. Chem. **115**(23), 2774–2777 (2003).

[216] P. Messina, A. Dmitriev, N. Lin, H. Spillmann, M. Abel, J. V. Barth, and K. Kern, Direct Observation of Chiral Metal-Organic Complexes Assembled on a Cu (100) Surface, J. Am. Chem. Soc. **124**(47), 14000–14001 (2002).

[217] C. C. Perry, S. Haq, B. G. Frederick, and N. V. Richardson, Face Specificity and the Role of Metal Adatoms in Molecular Reorientation at Surfaces, Surf. Sci. **409**(3), 512–520 (1998).

[218] M. Matena, M. Stöhr, T. Riehm, J. Björk, S. Martens, M. S. Dyer, M. Persson, J. Lobo-Checa, K. Müller, M. Enache, and *et al.*, Aggregation and Contingent Metal/Surface Reactivity of 1, 3, 8, 10-Tetraazaperopyrene (TAPP) on Cu (111), Chem. Eur. J. **16**(7), 2079–2091 (2010).

[219] S. Stepanow, N. Lin, and J. V. Barth, Modular Assembly of Low-Dimensional Coordination Architectures on Metal Surfaces, J. Phys.: Cond. Matter **20**(18), 184002 (2008).

[220] G. Pawin, K. L. Wong, D. Kim, D. Sun, L. Bartels, S. Hong, T. S. Rahman, R. Carp, and M. Marsella, A Surface Coordination Network Based on Substrate-Derived Metal Adatoms with Local Charge Excess, Angew. Chem. **120**(44), 8570–8573 (2008).

[221] T. Mochida, Sh. Matsumiya, A. Izuoka, N. Sato, T. Sugawara, and Y. Sugawara, Structure of 3-Hydroxyphenalenone, Acta Cryst. C: Cryst. Struct. Commun. **48**(4), 680–683 (1992).

[222] J. Hooper, D. A. Kunkel, S. Simpson, S. Beniwal, A. Enders, and E. Zurek, Chiral Surface Networks of 3-HPLN – A MolecularAnalog of Rounded Triangle Assembly, Surf. Sci.. (2014).

[223] N. Jiang, Y. Wang, Q. Liu, Y. Zhang, Z. Deng, K.-H. Ernst, and H.-J. Gao, Polymorphism and Chiral Expression in Two-Dimensional Subphthalocyanine Crystals on Au (111), Phys. Chem. Chem. Phys. **12**(6), 1318–1322 (2010).

[224] W. Xiao, X. Feng, P. Ruffieux, O. Gröning, K. Müllen, and R. Fasel, Self-Assembly of Chiral Molecular Honeycomb Networks on Au(111), J. Am. Chem. Soc. **130**(28), 8910–8912 (2008).

[225] Y. Ye, W. Sun, Y. Wang, X. Shao, F. Xu, X.and Cheng, J. Li, and K. Wu, A Unified Model: Self-Assembly of Trimesic Acid on Gold, J. Phys. Chem. C **111**(28), 10138–10141 (2007).

[226] J. A. Theobald, N. S. Oxtoby, M. A. Phillips, N. R. Champness, and P. H. Beton, Controlling Molecular Deposition and Layer Structure with Supramolecular Surface Assemblies, Nature **424**(6952), 1029–1031 (2003).

[227] M. Ruben, D. Payer, A. Landa, A. Comisso, C. Gattinoni, N. Lin, J.-P. Collin, J.-P. Sauvage, A. De Vita, and K. Kern, 2D Supramolecular Assemblies of Benzene-1, 3, 5-Triyl-Tribenzoic Acid: Temperature-Induced Phase Transformations and Hierarchical Organization with Macrocyclic Molecules, J. Am. Chem. Soc. **128**(49), 15644–15651 (2006).

[228] Y. Wei, S. W. Robey, and J. E. Reutt-Robey, Flux-Selected Titanyl Phthalocyanine Monolayer Architecture on Ag (111), J. Phys. Chem. C **112**(47), 18537–18542 (2008).

[229] D. A. Bonnell, Ferroelectric Organic Materials Catch Up with Oxides, Science **339**(6118), 401–402 (2013).

[230] S. G. Fleischman, S. S. Kuduva, J. A. McMahon, B. Moulton, R. D. Bailey Walsh, N. Rodríguez-Hornedo, and M. J. Zaworotko, Crystal Engineering of the Composition of Pharmaceutical Phases: Multiple-Component Crystalline Solids Involving Carbamazepine, Cryst. Growth Des. **3**(6), 909–919 (2003).

[231] K. B. Landenberger, O. Bolton, and A. J. Matzger, Two Isostructural Explosive Cocrystals with Significantly Different Thermodynamic Stabilities, Angew. Chem. Int. Ed. **52**(25), 6468–6471 (2013).

[232] S. K. Park, S. Varghese, J. H. Kim, S.-J. Yoon, O. K. Kwon, B.-K. An, J. Gierschner, and S. Y. Park, Tailor-Made Highly Luminescent and Ambipolar Transporting Organic Mixed Stacked Charge-Transfer Crystals: An Isometric Donor–Acceptor Approach, J. Am. Chem. Soc. **135**(12), 4757–4764 (2013).

[233] L. Zhu, Y. Yi, Y. Li, E.-G. Kim, V. Coropceanu, and J.-L. Brédas, Prediction of Remarkable Ambipolar Charge-Transport Characteristics in Organic Mixed-Stack Charge-Transfer Crystals, J. Am. Chem. Soc. **134**(4), 2340–2347 (2012).

[234] S. Horiuchi, T. Hasegawa, and Y. Tokura, Molecular Donor-Acceptor Compounds as Prospective Organic Electronics Materials, J. Phys. Soc. Jpn. **75**(5) (2006).

[235] N. Schultheiss and A. Newman, Pharmaceutical Cocrystals and Their Physico-chemical Properties, Cryst. Growth and Des. **9**(6), 2950–2967 (2009).

[236] S. Childs and M. J. Zaworotko, The Reemergence of Cocrystals: The Crystal Clear Writing is on the Wall Introduction to Virtual Special Issue on Pharmaceutical Cocrystals, Cryst. Growth Des. **9**(10), 4208–4211 (2009).

[237] T. Friscic and W. Jones, Recent Advances in Understanding the Mechanism of Cocrystal Formation via Grinding, Cryst. Growth Des. **9**(3), 1621–1637 (2009).

[238] J. H. ter Horst, M. A. Deij, and P. W. Cains, Discovering New Co-Crystals, Cryst. Growth Des. **9**(3), 1531–1537 (2009).

[239] H.-Y. Ye, Y. Zhang, S.-I. Noro, K. Kubo, M. Yoshitake, Z.-Q. Liu, H.-L. Cai, D.-W. Fu, H. Yoshikawa, K. Awaga, and *et al.*, Molecule-Displacive Ferroelectricity in Organic Supramolecular Solids, Sci. Rep. **3**, 2249 (2013).

[240] S. Horiuchi, F. Ishii, R. Kumai, Y. Okimoto, H. Tachibana, N. Nagaosa, and Y. Tokura, Ferroelectricity Near Room Temperature in Co-Crystals of Nonpolar Organic Molecules, Nature Mater. **4**(2), 163–166 (2005).

[241] S. Horiuchi, R. Kumai, and Y. Tokura, Room-Temperature Ferroelectricity and Gigantic Dielectric Susceptibility on a Supramolecular Architecture of Phenazine and Deuterated Chloranilic Acid, J. Am. Chem. Soc. **127**(14), 5010–5011 (2005).

[242] A. S. Tayi, A. K. Shveyd, A. C.-H. Sue, J. M. Szarko, B. S. Rolczynski, D. Cao, T. J. Kennedy, A. A. Sarjeant, C. L. Stern, W. F. Paxton, and *et al.*, Room-Temperature Ferroelectricity in Supramolecular Networks of Charge-Transfer Complexes, Nature **488**(7412), 485–489 (2012).

[243] K. Kobayashi, S. Horiuchi, R. Kumai, F. Kagawa, Y. Murakami, and Y. Tokura, Electronic Ferroelectricity in a Molecular Crystal with Large Polarization Directing Antiparallel to Ionic Displacement, Phys. Rev. Lett. **108**(23), 237601 (2012).

[244] F. Kagawa, S. Horiuchi, H. Matsui, R. Kumai, Y. Onose, T. Hasegawa, and Y. Tokura, Electric-Field Control of Solitons in a Ferroelectric Organic Charge-Transfer Salt, Phys. Rev. Lett. **104**(22), 227602 (2010).

[245] S. Horiuchi, R. Kumai, and Y. Tokura, A Supramolecular Ferroelectric Realized by Collective Proton Transfer, Angew. Chem. Int. Ed. **46**(19), 3497–3501 (2007).

[246] S. Horiuchi, R. Kumai, Y. Tokunaga, and Y. Tokura, Proton Dynamics and Room-Temperature Ferroelectricity in Anilate Salts with a Proton Sponge, J. Am. Chem. Soc. **130**(40), 13382–13391 (2008).

[247] K. W. Hipps, L. Scudiero, D. E. Barlow, and M. P. Cooke, A Self-Organized 2-Dimensional Bifunctional Structure Formed by Supramolecular Design, J. Am. Chem. Soc. **124**(10), 2126–2127 (2002).

[248] N. Wintjes, J. Lobo-Checa, J. Hornung, T. Samuely, F. Diederich, and T. A. Jung, Two-Dimensional Phase Behavior of a Bimolecular Porphyrin System at the Solid- Vacuum Interface, J. Am. Chem. Soc. **132**(21), 7306–7311 (2010).

[249] C. Bobisch, Th. Wagner, A. Bannani, and R. Möller, Ordered Binary Monolayer Composed of Two Organic Molecules: Copper-phthalocyanine and 3, 4, 9, 10-perylene-tetra-carboxylic-dianhydride on Cu (111), J. Chem. Phys. **119**, 9804 (2003).

[250] M. Ruiz-Osés, N. Gonzalez-Lakunza, I. Silanes, A. Gourdon, A. Arnau, and J.E. Ortega, Self-Assembly of Heterogeneous Supramolecular Structures with Uniaxial Anisotropy, J. Phys. Chem. B **110**(51), 25573–25577 (2006).

[251] B. Xu, Ch. Tao, W. G. Cullen, J. E. Reutt-Robey, and E. D. Williams, Chiral Symmetry Breaking in Two-Dimensional $C_{60} - ACA$ Intermixed Systems, Nano Lett. **5**(11), 2207–2211 (2005).

[252] L. Scudiero, K. W. Hipps, and D. E. Barlow, A Self-Organized Two-Dimensional Bimolecular Structure, J. Phys. Chem. B **107**(13), 2903–2909 (2003).

[253] J. C. Swarbrick, B. L. Rogers, N. R. Champness, and P. H. Beton, Hydrogen-Bonded PTCDA-Melamine Networks and Mixed Phases, J. Phys. Chem. B **110**(12), 6110–6114 (2006).

[254] I. Fernández-Torrente, K. J. Franke, and J. I. Pascual, Vibrational Kondo Effect in Pure Organic Charge-Transfer Assemblies, Phys. Rev. Lett. **101**(21), 217203 (2008).

[255] M. de Wild, S. Berner, H. Suzuki, Y. Hisao, D. Schlettwein, S. Ivan, A. Baratoff, H.-J. Guentherodt, and T. A. Jung, A Novel Route To Molecular Self-Assembly: Self-Intermixed Monolayer Phases, Chem. Phys. Chem. **3**(10), 881–885 (2002).

[256] T. R. Umbach, I. Fernandez-Torrente, J. N. Ladenthin, J. I. Pascual, and K. J. Franke, Enhanced Charge Transfer in a Monolayer of the Organic Charge Transfer Complex TTF–TNAP on Au (111), J. Phys: Condens. Matter **24**(35), 354003 (2012).

[257] G. A. Rojas, P. Ganesh, S. J. Kelly, B. G. Sumpter, J. A. Schlueter, and P. Maksymovych, Ionic Disproportionation of Charge Transfer Salt Driven by Surface Epitaxy, J. Phys. Chem. C **117**(38), 19402–19408 (2013).

[258] L. M. A. Perdigao, E. W. Perkins, J. Ma, P. A. Staniec, B. L. Rogers, N. R. Champness, and P. H. Beton, Bimolecular Networks and Supramolecular Traps on Au (111), J. Phys. Chem. B **110**(25), 12539–12542 (2006).

[259] E. Barrena, D. G. de Oteyza, H. Dosch, and Y. Wakayama, 2D Supramolecular Self-Assembly of Binary Organic Monolayers, Chem. Phys. Chem. **8**(13), 1915–1918 (2007).

[260] M. E. Cañas-Ventura, W. Xiao, D. Wasserfallen, K. Müllen, H. Brune, J. V. Barth, and R. Fasel, Self-Assembly of Periodic Bicomponent Wires and Ribbons, Angew. Chem. Int. Ed. **46**(11), 1814–1818 (2007).

[261] S. Lei, M. Surin, K. Tahara, J. Adisoejoso, R. Lazzaroni, Y. Tobe, and S. D. Feyter, Programmable Hierarchical Three-Component 2D Assembly at a Liquid- Solid Interface: Recognition, Selection, and Transformation, Nano Lett. **8**(8), 2541–2546 (2008).

[262] S. Yoshimoto, N. Higa, and K. Itaya, Two-Dimensional Supramolecular Organization of Copper Octaethylporphyrin and Cobalt Phthalocyanine on Au (111): Molecular Assembly Control at an Electrochemical Interface, J. Am. Chem. Soc. **126**(27), 8540–8545 (2004).

[263] F. Tao and S. L. Bernasek, Two-Dimensional Self-Assembly of a Two-Component Molecular System: Formation of an Ordered and Homogeneous Molecular Mesh, J. Am. Chem. Soc. **127**(37), 12750–12751 (2005).

[264] K. Suto, S. Yoshimoto, and K. Itaya, Two-Dimensional Self-Organization of Phthalocyanine and Porphyrin: Dependence on the Crystallographic Orientation of Au, J. Am. Chem. Soc. **125**(49), 14976–14977 (2003).

[265] L. Piot, C.-A. Palma, A. Llanes-Pallas, M. Prato, Z. Szekrényes, K. Kamarás, D. Bonifazi, and P. Samori, Selective Formation of Bi-Component Arrays Through H-Bonding of Multivalent Molecular Modules, Adv. Funct. Mater. **19**(8), 1207–1214 (2009).

[266] S. Uemura, M. Aono, K. Sakata, T. Komatsu, and M. Kunitake, Thermodynamic Control of 2D Bicomponent Porous Networks of Melamine and Melem: Diverse Hydrogen-Bonded Networks, J. Phys. Chem. C **117**(47), 24815–24821 (2013).

[267] K. E. Plass, K. M. Engle, K. A. Cychosz, and A. J. Matzger, Large-Periodicity Two-Dimensional Crystals by Cocrystallization, Nano Lett. **6**(6), 1178–1183 (2006).

[268] N. Issa, P. G. Karamertzanis, G. W. A. Welch, and S. L. Price, Can the Formation of Pharmaceutical Cocrystals be Computationally Predicted? Comparison of Lattice Energies, Cryst. Growth Des. **9**(1), 442–453 (2008).

[269] O. Echt, K. Sattler, and E. Recknagel, Magic Numbers for Sphere Packings: Experimental Verification in Free Xenon Clusters, Phys. Rev. Lett. **47**(16), 1121 (1981).

[270] I. A. Harris, R. S. Kidwell, and J. A. Northby, Structure of Charged Argon Clusters Formed in a Free Jet Expansion, Phys. Rev. Lett. **53**, 2390–2393 (1984).

[271] A. Enders, N. Malinowski, D. Ievlev, E. Zurek, J. Autschbach, and K. Kern, Magic Alkali-Fullerene Compound Clusters of Extreme Thermal Stability, J. Chem. Phys. **125**, 191102 (2006).

[272] S. Kervyn, N. Kalashnyk, M. Riello, B. Moreton, J. Tasseroul, J. Wouters, T. S. Jones, A. De Vita, G. Costantini, and D. Bonifazi, Magic Surface Clustering of Borazines Driven by Repulsive Intermolecular Forces, Angew. Chem. Int. Ed. (2013).

[273] M. Böhringer, K. Morgenstern, W.-D. Schneider, R. Berndt, F. Mauri, A. De Vita, and R. Car, Two-Dimensional Self-Assembly of Supramolecular Clusters and Chains, Phys. Rev. Lett. **83**, 324–327 (1999).

[274] Q. Li, C. Han, S. R. Horton, M. Fuentes-Cabrera, B. G. Sumpter, W. Lu, J. Bernholc, P. Maksymovych, and M. Pan, Supramolecular Self-Assembly of π-Conjugated Hydrocarbons via 2D Cooperative CH/π Interaction, ACS nano **6**(1), 566–572 (2011).

[275] D. Heim, K. Seufert, W. Auwärter, C. Aurisicchio, C. Fabbro, D. Bonifazi, and J. V. Barth, Surface-Assisted Assembly of Discrete Porphyrin-Based Cyclic Supramolecules, Nano Lett. **10**(1), 122–128 (2010).

[276] T. Yokoyama, S. Yokoyama, T. Kamikado, Y. Okuno, and S. Mashiko, Selective Assembly on a Surface of Supramolecular Aggregates with Controlled Size and Shape, Nature **413**(6856), 619–621 (2001).

[277] T. Yokoyama, T. Kamikado, S. Yokoyama, and S. Mashiko, Conformation Selective Assembly of Carboxyphenyl Substituted Porphyrins on Au (111), J. Chem. Phys. **121**, 11993 (2004).

[278] C. Iacovita, P. Fesser, S. Vijayaraghavan, M. Enache, M. Stöhr, F. Diederich, and T. A. Jung, Controlling the Dimensionality and Structure of Supramolecular Porphyrin Assemblies by their Functional Substituents: Dimers, Chains, and Close-Packed 2D Assemblies, Chem. Eur. J. **18**(46), 14610–14613 (2012).

[279] T. J. Lawton, J. Carrasco, A. E. Baber, A. Michaelides, and E. C. H. Sykes, Visualization of Hydrogen Bonding and Associated Chirality in Methanol Hexamers, Phys. Rev. Lett. **107**(25), 256101 (2011).

[280] M.-C. Blüm, E. Ćavar, M. Pivetta, F. Patthey, and W.-D. Schneider, Conservation of Chirality in a Hierarchical Supramolecular Self-Assembled Structure with Pentagonal Symmetry, Angew. Chem. **117**(33), 5468–5471 (2005).

[281] A. Kühnle, T. R. Linderoth, and F. Besenbacher, Self-Assembly of Monodispersed, Chiral Nanoclusters of Cysteine on the Au (110)-(1× 2) Surface, J. Am. Chem. Soc. **125**(48), 14680–14681 (2003).